Università degli Studi di Roma
"Tor Vergata"
Facoltà di Scienze Matematiche, Fisiche e Naturali
Dipartimento di Fisica

Dottorato di Ricerca in Fisica XXI ciclo

PhD Thesis

# The cosmic rays flux from the Pierre Auger Observatory data

Candidato : Claudio Di Giulio

A.A. 2008/2009

Relatore : Prof. Giorgio Matthiae

Coordinatore : Prof. Piergiorgio Picozza

# Acknowledgments

I would like to thank Prof. Giorgio Matthiae and Valerio Verzi for believing in me and for all the support they gave me. I would also like to thank Paolo Privitera, Paolo Petrinca and Pedro Facal for all I learned from them. A special thank at María Monasor, Matías Tueros and Gonzalo Rodriguez for discussion, fruitful and not, *muchas gracias*.

I would like to acknowledge all the Pierre Auger Collaboration members for all I learned during the meetings in those 3 years. I would like to mention Ioana Mariş, Francesco Salamida, Nicolás Busca, Markus Roth, and Michael Unger for fruitful discussion.

Thanks to my family that help me during the PhD period, in particular this last year that was very difficult for all us. Thanks to my friends for giving me the opportunity to share the doubts and questions.

I specially thank Fabiana, for everyday life.

This work was partially funded by the Dipartimento di Fisica dell'Università degli Studi di Roma Tor Vergata, the Istituto Nazionale di Fisica Nucleare di Roma Tor Vergata and by América Latina Formación Académica - European Community / High Energy physics Latin-american European Network (ALFA-EC / HELEN).

# Contents

# Introduction

The Pierre Auger Observatory is exploring the mysteries of the highest-energy cosmic rays. This experiment was conceived more than ten years ago to explore the properties of the most energetic cosmic rays such as the flux, arrival direction distribution and mass composition, with high statistical significance and covering the whole sky.

A few years after Penzias and Wilson established the existence of the cosmic microwave background with a mean temperature of 2.7 $K$, Greisen, Zatsepin and Kuzmin predicted that a cutoff of the cosmic ray flux at the highest energies is expected due to the interaction of the ultra high energy cosmic rays with the cosmic microwave background photons.

Before the Pierre Auger Observatory the AGASA and Hires experiments have obtained differents results about this cutoff. Those experiments use different detection techniques. The Auger experiment is an "hybrid" detector in the sense that uses for the first time both techniques.

It consists of two complementary detectors designed to observe, in coincidence, the shower of particles which can be spread along several kilometers when they reach the earth surface. A Surface Detector (SD) composed of 1600 Cherenkov stations samples the front of the shower at ground. A Fluorescence Detector (FD) equipped with 24 telescopes collects the fluorescence light emitted by atmospheric nitrogen molecules excited as the shower is crossing the atmosphere. The FD measure the longitudinal profile of the shower.

The Southern Observatory in Argentina near the Malargüe village was completed in May 2008 and inaugurated in November 2008. It is taking data in stable manner since January 2004. During this time the experiment has accumulated an unprecedented statistics and the first results are pubblished. The Northern Observatory will be built in Colorado, USA. Both observatories allow a full sky coverage.

The main objective of this thesis is the measurement of the cosmic ray energy spectrum above 3 EeV based on the data recorded at the Pierre Auger Observatory.

The energy spectrum, i.e the flux of cosmic rays as a function of energy, is obtained exploiting the features of both Fluorescence and Surface Detectors. On the one hand the Surface Detector is used to provide the large statistical sample needed to study the ultra-high energy tail of the cosmic ray spectrum and also allows to calculate the total exposure, independently of the energy above a certain threshold in a simple geometrical way. On the other hand, the Fluorescence Detector provides a calorimetric measurement of the primary energy which is nearly independent of mass composition or interaction model. Both techniques are combined in order to obtain an energy spectrum which does not rely on detailed shower simulations or assumptions about the hadronic interactions involved.

In Chapter 1 a brief review on the current knowledge of Ultra-High Energy Cosmic Rays (UHECR) is given. A short description of the phenomenology of air showers induced by UHECR is also given. In Chapter 2 the Pierre Auger detectors are briefly described, and the data acquisition system is presented.

During the preparation of my Ph.D. thesis, I was involved in the construction and commissioning of six fluorescence telescopes. I also participated in three periods of fluorescence detector data taking.

In Chapter 3 the reconstruction methods to obtain the cosmic ray observables using both detectors are presented. In Chapter 4 an new method that I have developed, to reconstruct the longitudinal shower profile using the fluorescence detector is described together with the differences with respect to the present official Auger reconstruction.

In Chapter 5 the method to obtain the energy calibration using the direct energy measurements of the fluorescence detector is described. The origin of systematics for this energy calibration are also discussed. In the last Chapter the Auger energy spectrum is presented and astrophysical implications are discussed.

# Chapter 1

# Ultra-High Energy Cosmic Rays

Cosmic rays were discovered by Victor Hess in 1912 using detectors placed in balloons [1]. Later, Pierre Auger and collaborators [2], used time correlations between separated particle counters to prove the existence of air showers induced by primary particles of energies exceeding $10^{15}$ eV. Remarkably, during the years before particle accelerators, cosmic rays were the basis of particle physics. Positrons [3] and muons [4], among others, were discovered in cosmic rays.

Ultra High Energy Cosmic Rays (UHECR) are those particles arriving at earth with an energy above $10^{19}$ eV, well above the energies achievable on this and next generation particle accelerators. They are detected through the extensive air shower that they produce in the atmosphere and their flux is extremely low (below 1 per km$^2$ per century).

In this chapter we briefly review the most important theoretical aspects of cosmic ray physics, putting emphasis on crucial aspects which still need to be fully understood and the first results obtained by high level experimental developments.

## 1.1 Cosmic ray spectrum

The spectrum of cosmic rays spans through 15 energy decades, where the flux shows a nearly constant $E^{-3}$ dependence. In the tail of the cosmic ray spectrum, the region of the ultra high energy cosmic rays of energy exceeding $10^{19}$ eV, our knowledge is limited due to the low statistics and the experimental uncertainties.

The importance of UHECR has to be understood in the light of some

theoretical considerations. On one hand, UHECR are expected to interact with cosmic microwave background and loose energy, limiting its maximum travel distance to the Mpc range, while, on the other hand, the dimensions and magnetic field strengths of astrophysical objects strongly limit the possible sites where these particles could be accelerated to these extreme energies. The spectrum of cosmic rays, the differential flux as a function of the primary cosmic ray energy, is well known (Figure 1.1). The flux shows an approximate $E^{-3}$ dependence along over 15 energy decades. A detailed discussion of the spectrum is out of the scope of this brief introduction, but is worth noting the two most prominent features: the knee (around $10^{16}$ eV) and the ankle (around $5{\times}10^{18}$ eV). Both points are characterized by slight changes in the spectral index. The ankle is usually tentatively explained as a change in the origin of the dominant fraction of the cosmic ray flux, from galactic to extra-galactic. Figure 1.2 shows a closer look of the high energy tail of the cosmic ray spectrum, with recent results from two experiments, HiRes [5] and AGASA [6]. Besides the disagreement in the normalization of the flux, the two detectors report different results on the spectrum structure at the higher energy values: while HiRes claims a spectrum suppression over $10^{20}$ eV, AGASA data suggests no evidence of this suppression. The importance of this discrepancy is at the heart of the puzzle and involves the GZK mechanism explained below. Both measurements are limited by poor statistics and high systematic errors. The Pierre Auger detector has give a statistical evidence of the flux suppression [7] shown by HiRes [5]. In Figure 1.3 the differential flux J as a function of energy, with statistical and the fractional differences between Auger and HiRes I data compared with a spectrum with an index of 2.69 is shown.

To summarize, the Pierre Auger Collaboration (PAO) results reject the hypothesis that the cosmic-ray spectrum continues with a constant slope above $4{\times}10^{19}$ eV, with a significance of 6 standard deviations. In a previous paper [8, 9], the Pierre Auger Collaboration reported that sources of cosmic rays above 5.7 $\times 10^{19}$eV are extragalactic and lie within 75 Mpc.

Both results suggest that the GZK prediction may have been verified.

## 1.2 Acceleration, origin, propagation and composition

The origin of UHECR continues to be an unsolved problem even after seventy years since their discovery. This section is devoted to argue general principles of origin, acceleration and propagation of these extremely high energy

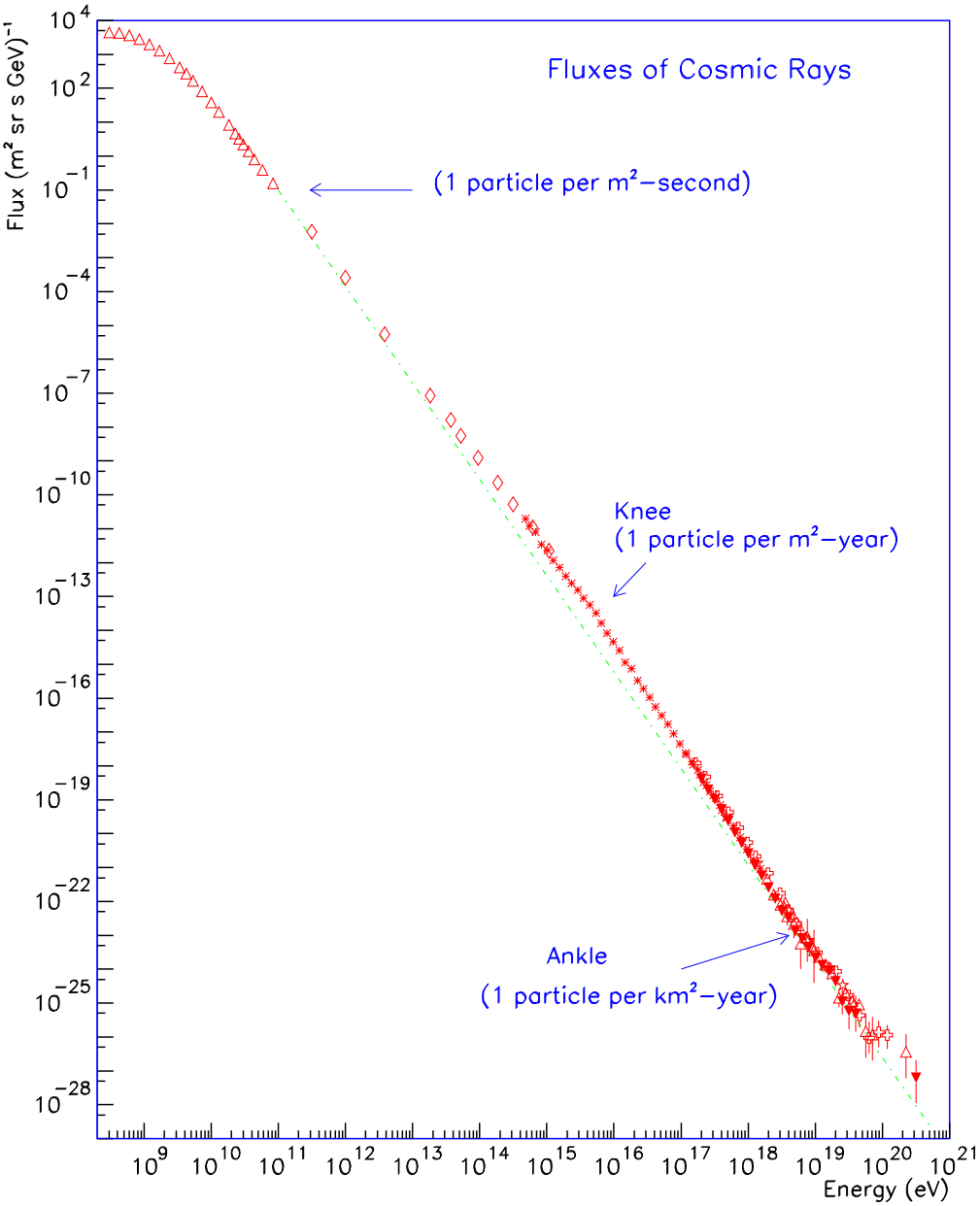


Figure 1.1: Cosmic ray spectrum.

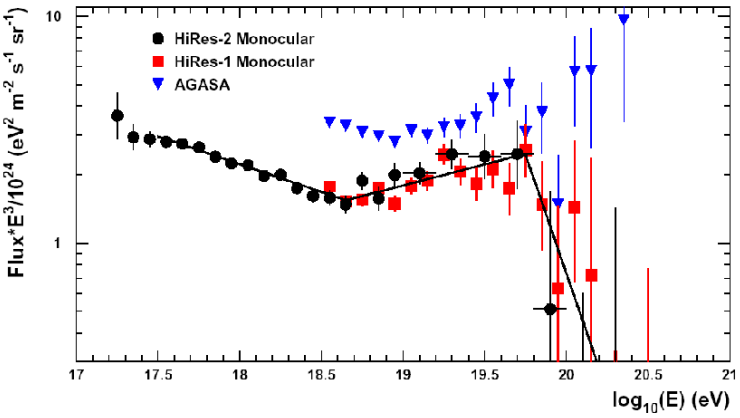


Figure 1.2: The high energy end of the cosmic ray spectrum, multiplied by $E^3$ to evidence the spectral features. The circles are monocular data from HiRes-II and the squares monocular data from HiRes-I. The triangles are data from AGASA. The line segments are the result of the flux to a triple-power law [5].

particles.

The theories developed to explain the acceleration of cosmic rays are based on the mechanism, firstly introduced by Fermi, to accelerate particles through a statistical process by collisions with moving magnetic clouds or in shock-waves presented in a number of astrophysical objects. Nowadays it is very difficult to obtain a satisfactory theory mainly due to the lack of data. As a result, some recent theoretical works that demand new physics have been developed as an alternative to explain the origin of the highest energy cosmic rays. The kind of measurements required to confirm these new models will be also briefly discussed.

### 1.2.1 Acceleration mechanisms and cosmic ray sources

**The Accelerating mechanisms**: One of the earliest theories on the acceleration of cosmic rays was proposed by Enrico Fermi in 1949 [10]. It became known as the Second Order Fermi Mechanism. In this model, particles collide stochastically with magnetic clouds in the interstellar medium. Those particles involved in head-on collisions will gain energy and those involved in tail-end collisions will lose energy. On average, however, head-on collisions are more probable. In this way, particles gain energy over many collisions. This mechanism naturally predict a power law energy spectrum, but the power index depends on the details of the model and would not give rise to a uni-

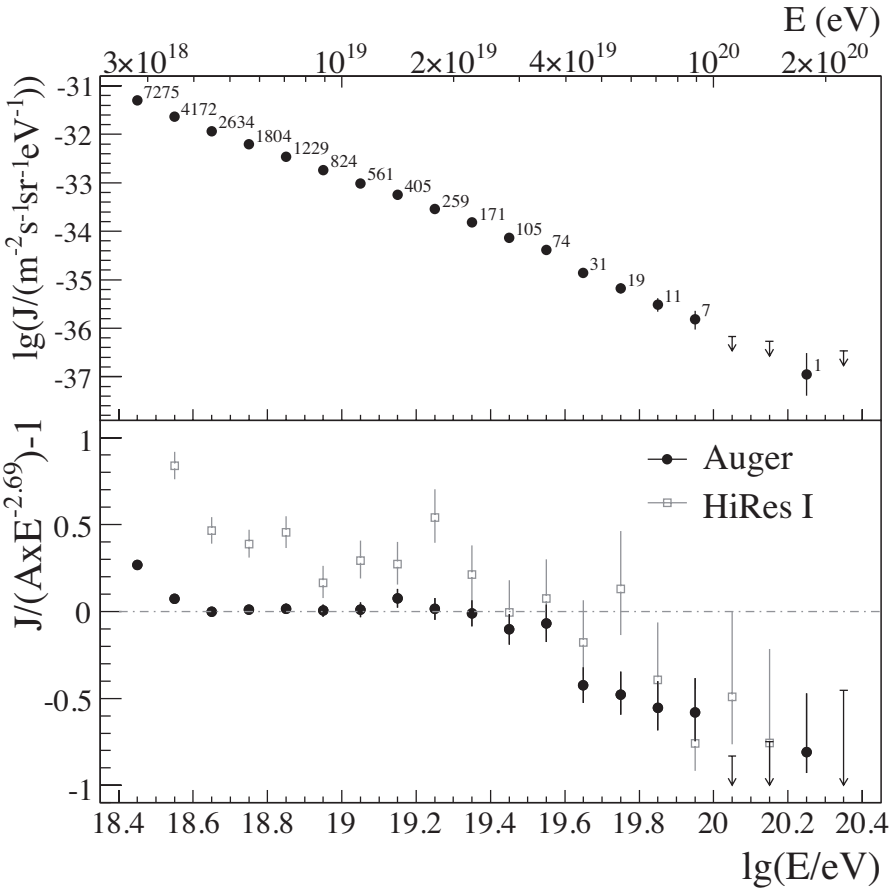


Figure 1.3: Upper panel: The differential flux J as a function of energy, with statistical uncertainties. Lower Panel:The fractional differences between Auger and HiRes I data compared with a spectrum with an index of 2.69.

versal power law for cosmic rays arriving from all directions. This mechanism is also too slow and too inefficient to account for the observed UHE cosmic rays (Fig. 1.4).

A more efficient version of Fermi Acceleration was proposed in the late 1970's. In this model, particles are accelerated by strong shock waves propagating through interstellar space.

A schematic of the process is described below [11].

Consider the case of a strong shock propagating at a supersonic, but non-relativistic speed U through a stationary interstellar gas. Figure 1.5 (a) at left shows the situation in the rest frame of the gas: the density, pressure, and temperature of the gas upstream and downstream of the shock front are $\rho_2$, $p_2$, $T_2$ and $\rho_1$, $p_1$, $T_1$, respectively.

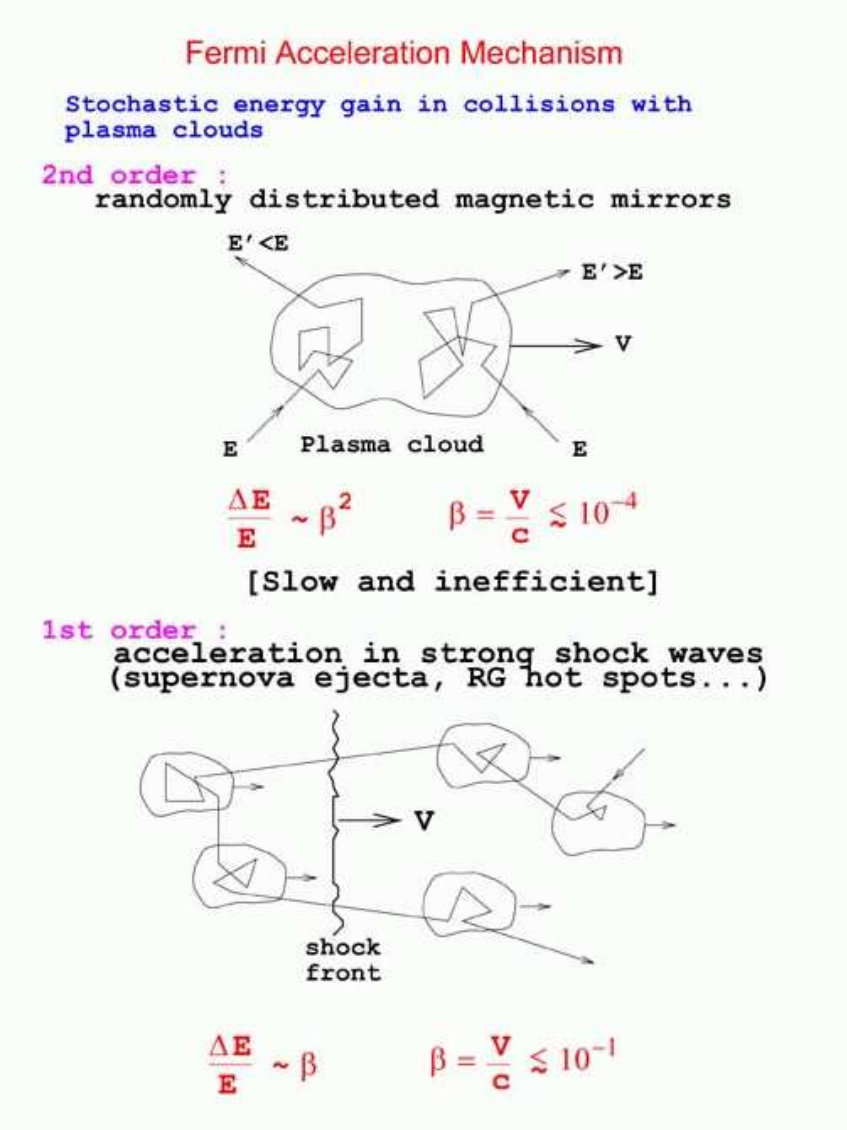


Figure 1.4: The Fermi mechanisms.

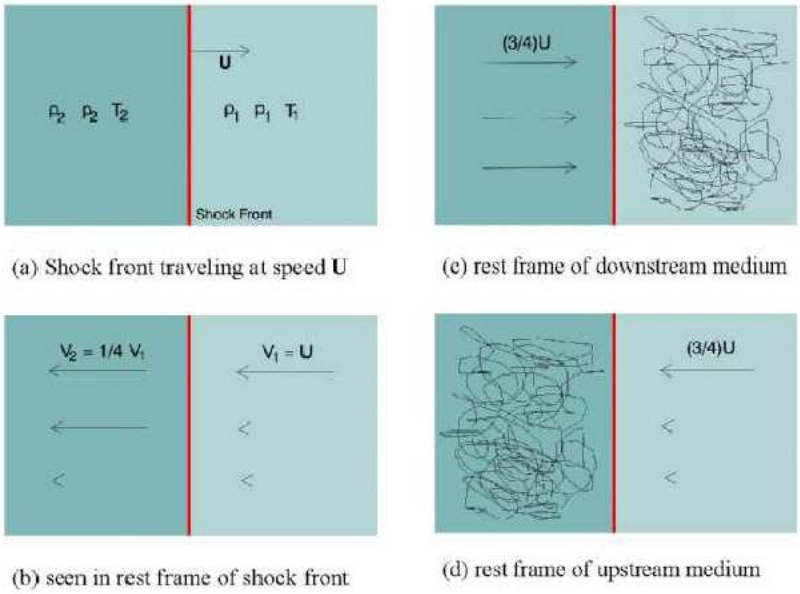


(a) Shock front traveling at speed **U**

(c) rest frame of downstream medium

(b) seen in rest frame of shock front

(d) rest frame of upstream medium

Figure 1.5: Schematic of the First Order Fermi Mechanism.

When viewed in the rest frame of the shock front as in Figure 1.5 (b) below, particles are arriving from downstream with speed $v_1 = U$ and exiting upstream at speed $v_2$. Conservation of the number of particles implies the relation: $\rho_1 \, v_1 = \rho_2 \, v_2$. In the case of strong shock we expect $\rho_2/\rho_1 = (g+1)/(g-1)$, where $g$ is the usual ratio of heat capacities. For a fully ionized plasma, one expects $g = 5/3$, leading to a velocity ratio of $v_1/v_2 = 4$.

Transforming into the rest frame of the downstream medium, the particles upstream appear to flow into the shock front with a speed of $(3/4)\ U$. Similarly, the downstream particles appear to stream into the shock front with a speed of $(3/4)\ U$ as seen in the rest frame of the downstream medium. These are illustrated in Figures 1.5 (c) and 1.5 (d) above.

A particle crossing from either side of the shock front is more likely to suffer a head-on collision, which then tends to send it back in the opposite direction with an increase in energy. A particle that repeatedly crosses the shock front can gain energy rapidly. Consequently, this model is referred to as the "First Order Fermi Mechanism".

First order Fermi acceleration naturally predicts a power law spectrum of $DNA(E)/dE \ E^{-2}$. While the power index of 2 does not agree with the measured index of about 3, this model predicts, for the first time, a power law spectrum with a unique spectral index that is independent of the details of the local environment. The mechanism requires only the presence of strong

shocks, which are quite plausibly present in the expected sources of cosmic rays.

**Possible Sources of UHE Cosmic Rays**: The leading candidates for the sources of UHE cosmic rays are large, energetic structures where strong shocks are expected to be found. The most well known of these are supernova remnants, which have long been suspected to generate cosmic rays.

In 1995, Japan's ASCA X-ray Satellite, reported positive observation of non-thermal X-ray emissions from the Supernova Remnant SN1006. The observed emission spectrum is consistent with synchrotron emission by accelerated charged particles. This report is widely seen as confirmation of supernova remnants as a known source of cosmic rays.

The observed emission from SN1006, with some fine tuning of the emission models, can explain the existence of cosmic rays up to $10^{15}$ eV. However, it is difficult to explain the existence of cosmic rays above $10^{18}$ eV, because supernovae are simply not large enough to maintain acceleration to the UHE regime. Furthermore, no positive correlation has been observed between the arrival directions of UHE cosmic rays and supernova remnants.

There are many larger objects in the sky where strong shocks are expected. For example, strong shocks are possible around colliding galaxies such as NGC 4038/9. However, there is no evidence that these objects are sources of UHE cosmic rays.

Another class of objects which are candidate sources of UHE cosmic rays are active galactic nuclei (AGN). AGN is the generic name given to a class of galaxies which are suspected to have at their center a super massive black-holes. AGN's are typically accompanied by jets which can extend 50-100 thousand light-years.

The maximum energy attainable in diffusive shock acceleration depends ultimately on the size and the magnetic field strength of the object where acceleration takes place. Large sizes and strong fields are required to accelerate particles up to $10^{20}$ eV, otherwise their Larmor radius exceeds the size of the object and the particles are able to escape the acceleration region.

This condition is summarized in the following expression:

$$E_{max} \simeq \beta Z B L \tag{1.1}$$

for the maximum energy, $E_{max}$, in $10^{18}$ eV units attainable by a particle of charge $Z$ being accelerated by a shockwave traveling at a velocity $\beta$ (in units of $c$) in a region of magnetic field $B$ (in $\mu G$) and of characteristic size $L$ (in kpc). The Hillas plot [12] (Figure 1.6) presents the magnetic field $B$ vs. $R$ for the main astrophysical candidates for accelerating ultra high energy cosmic rays. It shows that only few of these candidates are barely suitable.

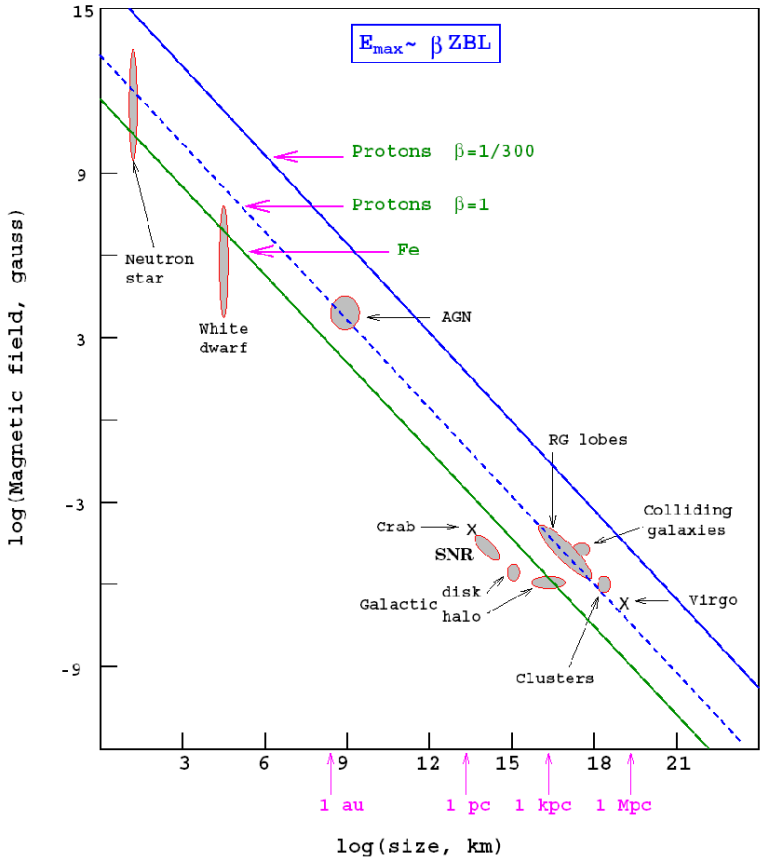


Figure 1.6: The Hillas plot shows the size and magnetic field strength of astrophysical objects that are candidates for suitable accelerating regions. The three lines are the values required to accelerate Fe nucleus and protons (for $\beta = 1$ and for the more realistic $\beta = 1/300$) up to $10^{20}$ eV. All the objects below the lines are excluded as possible acceleration sources of ultra high energy cosmic rays.

The maximum energy is further limited by losses in the accelerating region, that compete with the acceleration mechanism.

**Exotic Mechanisms**: Other ideas for explaining the existence of UHE cosmic rays include:

- Top-Down Models: Decay or annihilation of some super-heavy particles or cosmological relics (e.g. topological defects, relic magnetic monopoles.);
- Acceleration in Catastrophic events GRB's;
- New Physics.

### 1.2.2 Propagation and GZK cut-off

Above $10^{20}$ eV protons interact with cosmic microwave background photons, undergoing a photoproduction reaction:

$$p + \gamma \rightarrow p + \pi$$

that, for a typical energy of the cosmic microwave background photons of $6.4 \times 10^{-4}$ eV, is kinematically possible when the energy of the incident proton is above $4 \times 10^{19}$ eV [13]. The mean free path for a proton of this energy in the cosmic microwave background is about 10 Mpc.

This has an immediate consequence on the energy of an ultra high energy proton arriving to earth form a distant source: its energy will fall below the photoproduction threshold ($4 \times 10^{19}$ eV) in less that 100 Mpc (Figure 1.7). Or, in other words, ultra high energy cosmic ray sources must be relatively near earth.

If cosmic ray of UHECR are not produced in the earth neighborhood, the signature of this interaction would be a suppression of cosmic ray flux around $10^{20}$ eV. This effect is known as the GZK cutoff, named after Greisen, Zatsepin and Kuzmin [16]. The actual form of the spectrum cutoff would depend on the characteristics of the sources and on their spatial distribution (Figure 1.8).

Similar mechanisms apply to the inter-galactic propagation of nuclei (photodisintegration reactions) and gamma rays (pair creation, both on CMB and on diffuse background radio photons) leading to an expected flux suppression similar to that of protons [17].

Furthermore, energetic protons ($E > 10^{18}$ eV) may also lose energy through pair creation:

$$p + \gamma \rightarrow p + e^+ + e^-$$

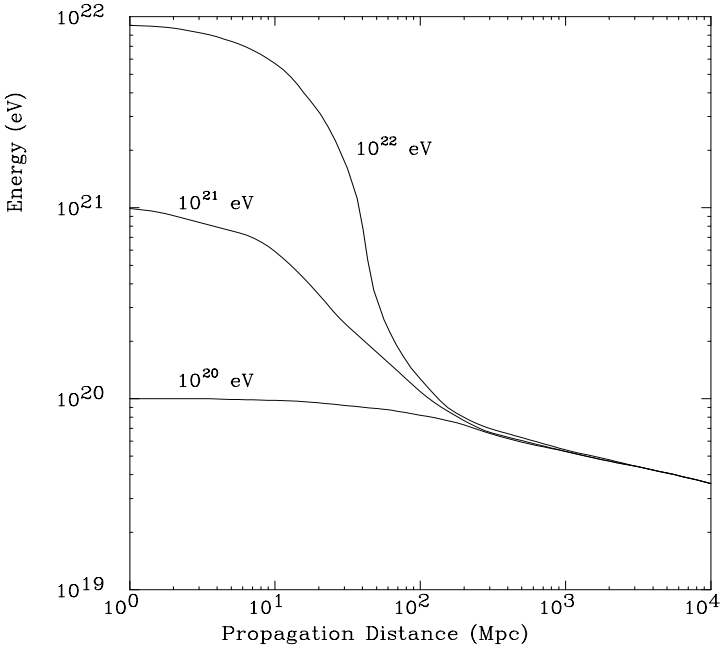


Figure 1.7: Energy of a proton traveling through the CMBR. The three curves correspond to three different starting energies (as noted), each one averaged from the simulation of 1000 protons [14].

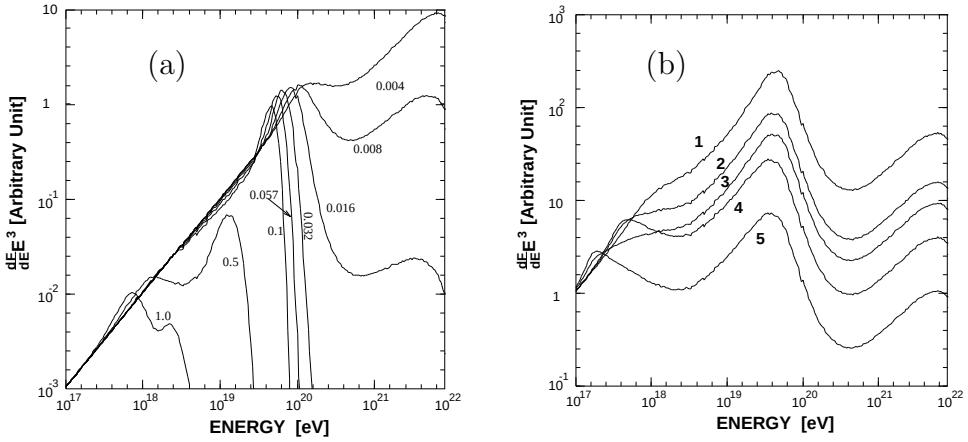


Figure 1.8: Two different theoretical calculations for the cutoff. (a) One single source, with $E^{-2}$ spectrum, at different redshift distances (roughly 20 Mpc to 5 Gpc). (b) Several cosmological models, with different parameters for galactic evolution and cosmic ray emission spectrum [15].

Although the energy loss per interaction for pair production is much smaller than the corresponding for pion production, the creation of electron-positron pairs is important since it can contribute to the shape of the observed energy spectrum in the region between 1 EeV and the ankle where pair production seems to be the dominant process [18].

The GZK mechanism and the Hillas plot impose tights constraints on the possible sources of extremely high energy cosmic rays. Moreover, given the strength of inter-galactic magnetic fields, if these events are produced nearby, as suggested by the GZK mechanism, they should point back to their sources. These events have been reported by several experiments and no conclusive evidence of correlation with possible nearby accelerating regions has been found before Auger.

### 1.2.3 Arrival directions

The first evidence that the cosmic rays possess a charge was given by East-West asymmetries caused by their deflection in the magnetic field of Earth. Up to energies of a few 10 EeV they are completely isotropic. In the highest energies they are affected by the galactic and extragalactic magnetic fields. Only above 1 EeV, particles cannot be anymore confined by the 3 $\mu G$ magnetic field of our galaxy. Their origin can be identified depending on the intergalactic magnetic field and the distance to the source, but the deflection angle at a few times 10 EeV is less than 5 degrees for the nearby astrophysical objects.

Finding the sources of the UHECRs has a long history. Even before they were identified it was assumed that very good accelerating sites are nearby radio galaxies [19], which are containing active galactic nuclei, super-massive black holes with a mass 6 orders of magnitude larger than the solar mass. In active galactic nuclei (AGN) a big amount of matter is accreting, part of it being released in the form of jets.

The maximum energy that can be reached in these astrophysical objects is $10^{21}$ eV [20] (this theory being supported by the cutoff in the non-thermal emission spectrum produced by electrons, observed in many radio galaxies). The acceleration sites for the UHECRs can be the beam dumped AGN, Galaxies where the jet hits an intergalactic cloud of matter [21], or the region very close to the black hole [22] and even in the remains of the fossil jets of old AGNs [23].

After lots of trials to find significant anisotropies at the highest energy the recent results of the Pierre Auger Observatory have proved a correlation of the arrival direction of cosmic rays at energies above 57 EeV with close by AGNs [8, 9]. The data illustrated in Fig. 1.9 show the arrival direction

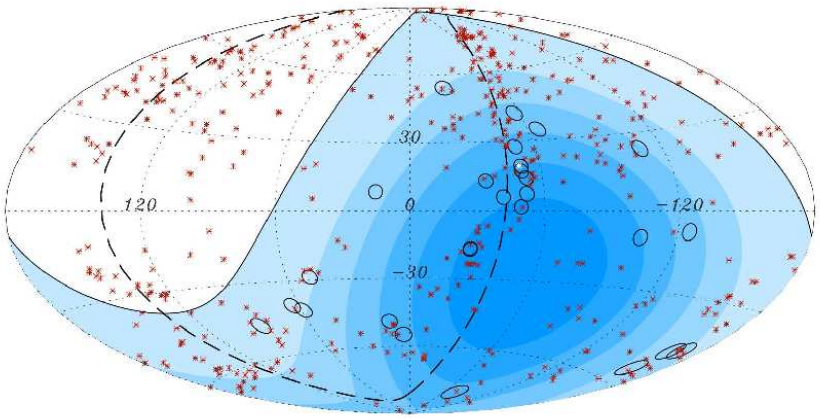


Figure 1.9: Arrival direction of the cosmic rays(circles) with energies greater than 57 EeV measured by the Pierre Auger Observatory and the position of the close by AGN objects (stars) in the Aitoff projection of the galactic coordinates. In blue the integrated exposure of the detector is shown [8].

together with AGN locations. 22 events out of 27 are within a 3.1 degrees separation angle from AGNs, and the majority of the ones that do not correlate are near the galactic plane, where the expected cosmic ray deflections are largest and the used catalog is incomplete. The data does not identify AGNs as the sources of cosmic rays, other astrophysical object distributed similar to nearby AGNs could also be possible candidates.

### 1.2.4 New scenarios as UHECR sources

The controversy caused by the lack of data needed to confirm possible acceleration scenarios and the detection of cosmic rays particles with energies in excess of $10^{20}$ eV has led to propose alternative theories that demand new physics to explain the origin of UHECR.

A distinctive feature of all top-down models and the Z-burst model is the prediction of a large photon flux at high energies. Therefore, the photon fraction of the total UHECR flux is a crucial test for these non-acceleration models [24, 25, 26].

The Pierre Auger Collaboration has set an upper limit on the photon fraction above 10 EeV which is twice as strong as those given previously [27]. This photon limit is obtained from the direct observation of the discriminating observable, the depth of shower maximum Xmax, using the fluorescence technique. Although the method supposes a great advantage since it not rely

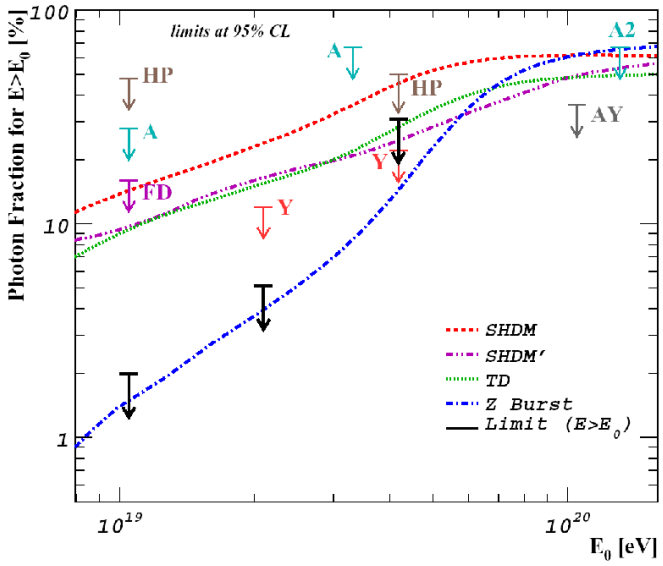


Figure 1.10: Upper limits at a confidence level of 95% to the cosmic ray photon fraction derived in (Auger) and those previously obtained from AGASA (A1, A2) and Haverah Park (HP) data, compared to expectations for non-acceleration models (TD: topological defects, SHDM: superheavy relic particles, ZB: Z-burst model) [28].

on the simulation of nuclear primaries (subject to large uncertainties from modelling hadronic interactions), the derived upper limit to the photon fraction of 16% is limited by a low statistics and it is not able to test the photon flux predicted by top-down models. A more recent and stringent limit on the photon flux, obtained using the large statistics accumulated with the array of surface detectors at the Pierre Auger Observatory, is presented in [28] together with an improvement of previous measurement, using the fluorescence detector. Now the maximum flux of photons has been constrained above different energy limits to 2.0%, 5.1% and 31% at 10, 20 and 40 EeV respectively (see Figure 1.10).

These results are discussed in [29] showing that the models based on the decay of superheavy dark matter in the halo of our Galaxy are essentially excluded from being the sources of UHECR unless their contribution becomes significant only above around 100 EeV. For models based on topological defects the results are not so conclusive since some of them are compatible with the current limits and may be best constrained by the high-energy neutrino flux limit [30].

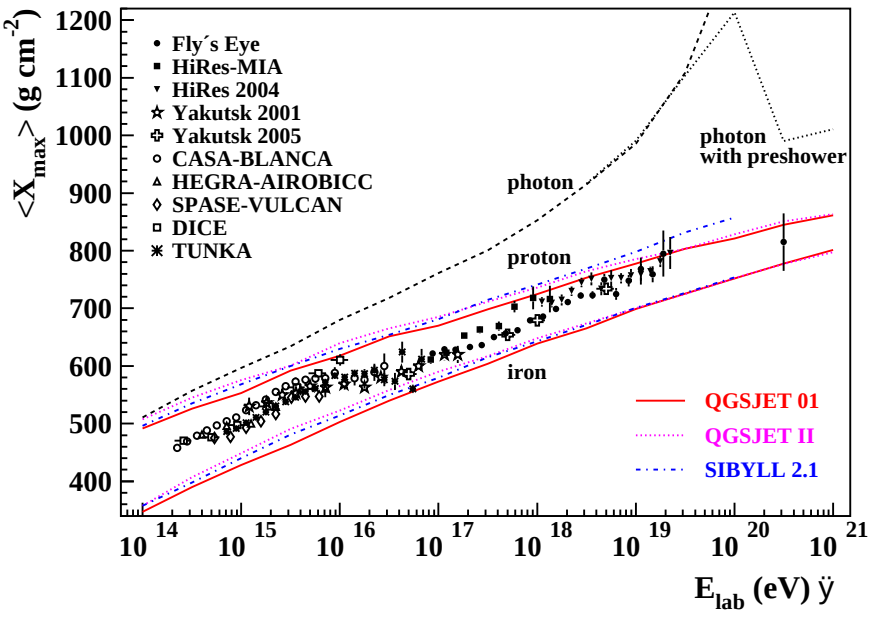


Figure 1.11: Xmax as a function of energy measured by different experiments compared with predictions of different hadronic models for proton and iron showers.

### 1.2.5 Composition

For cosmic rays of low energies (up to about $10^{15}$ eV) the particle flux is high enough to allow a direct detection which also provides valuable information about their composition. For this energy range the composition of cosmic rays have been found to be rather similar to those in the interstellar medium with some small differences that have been explained using the spallation of heavy nuclei to lighter ones.

Above these energies direct identification of the primary particle is not possible and cosmic rays are studied through the air showers that they develop in the atmosphere. One of the methods used to estimate the primary mass is based on the measurement of Xmax , defined as the atmospheric depth where the longitudinal development rises the maximum number of particles. The elongation rate theorem proposed by Linsley in 1977 [31] shows that the average value of Xmax at a certain energy is related to the mass of the primary particle. Figure 1.11 shows the maximum depth Xmax as a function of energy by from different experiments. As it can be observed, for energies up few times $10^{16}$ eV the composition is mainly dominated by iron nuclei. This fact is probably related with the limit of the efficiency of SNRs to accelerate cosmic rays since their radius becomes comparable to the Larmor radius of the particles. As the maximum energy attainable in

SNRs is proportional to the particle charge, iron nuclei will be accelerated to higher energies than lighter primaries. Above more or less $6 \times 10^{16}$ eV the experiments with data in this region, HiRes-MIA [32], HiRes [33], Fly's Eye [34] and Yakutsk [35], suggest a change in the composition from a heavy blend to a flux mainly dominated by proton primaries close to $10^{19}$ eV. The Pierre Auger Collaboration has estimated the variation of Xmax for the region of UHECR [36] and the results are shown in Figure 1.12. Data are well described by a double linear fit (dashed gray line in the left panel of Figure 1.12) allowing for a break in $2.2 \times 10^{18}$ eV. The slope of the fit is the so-called elongation rate. Though measurements favour a mixed composition for all energies, detailed interpretations are ambiguous since they are subject to the uncertainties in the hadronic interactions at the highest energies. Whereas some models suggest a moderate lightening of the primary mass at low energies and a constant composition at high energies, other ones suggest a transition from light to heavy elements at high energies.

## 1.3 Extensive air showers and cosmic ray detection

It is not possible to use satellite or balloon based detectors to study ultra high energy cosmic rays, due to their small flux: they have to be detected through the extensive air showers they produce in the atmosphere. When a cosmic ray primary undergoes an inelastic collision with an atmospheric nucleus its energy is shared between the products of the collision. Then, the created particles suffer successive collisions, giving rise to successive generations of shower particles.

Extensive air showers can be electromagnetic or hadronic, depending on the nature of the primary particle. In an hadronic shower induced by a baryon more than 90% of the energy is channeled into electromagnetic subshowers, via the decay of the $\pi^0$ produced in the hadronic interactions.

Electromagnetic showers, induced by photons or electrons, are governed by two processes: photons undergo pair production while electrons/positrons radiate bremsstrahlung photons. The size of the shower grows until the mean energy of the electrons falls below the critical energy and ionization losses overcome bremsstrahlung. The hadronic showers are characterized by the interactions of the primary hadron in the atmosphere, that will generally a number of charged and neutral pions. Neutral pions decay into two photons so the energy they carry is channeled into two electromagnetic subshowers.

What happens to charged pions depends mainly on its Lorentz factor:

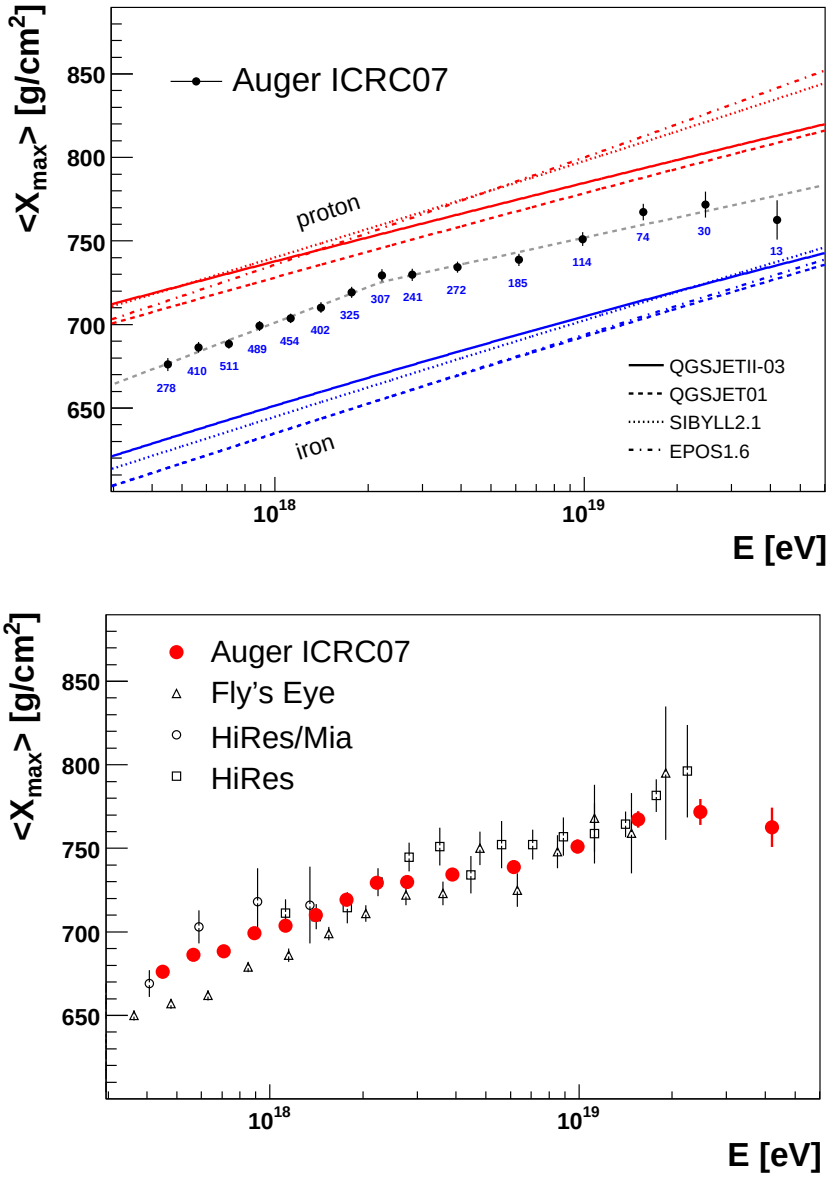


Figure 1.12: Xmax as a function of energy measured by the Pierre Auger Observatory. Data are compared to predictions from different hadronic interaction models for proton and iron primaries (up), and to data from previous experiments (down). [36].

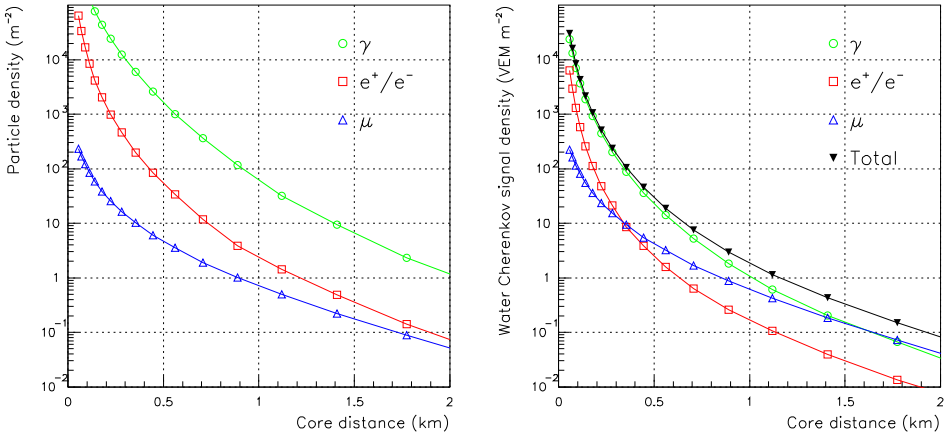


Figure 1.13: Left plot: lateral distribution at ground level of a simulated $10^{19}$ proton shower. Right plot: expected signal in a water Čerenkov detector [40].

having high factor, they will suffer a new interaction, without decaying. This will result in a new generation of charged and neutral pions and with them another fraction of the primary energy transferred into electromagnetic subshowers. Eventually some of the created charged pions will decay to a muon neutrino pair: this constitutes the fraction of the primary energy that, different to the electromagnetic component, will not be ultimately deposited in the atmosphere. Its value depends slightly on primary energy and composition but is around 10% of the firsts.

The study of air shower processes is necessary to extract the relevant information, most notable primary energy and mass, from shower measurements. A detailed description of cosmic ray shower phenomenology is out of the scope of this thesis. We will limit to a very brief introduction of the main experimental techniques, complemented with the relevant aspects of extensive air showers. Excellent reviews of air shower phenomenology and ultra high energy cosmic ray experimental techniques are found in the literature [13][37][38][39][40].

### Surface detectors

Surface detectors sample the extensive air shower at ground by means of an array of particle detectors. The shower is essentially a disc of particles moving at speed of light. When it strikes the ground, the particles are spread away from the shower axis (defined by the direction of the primary) due to the combined effect of multiple Coulomb scattering and traverse momentum in

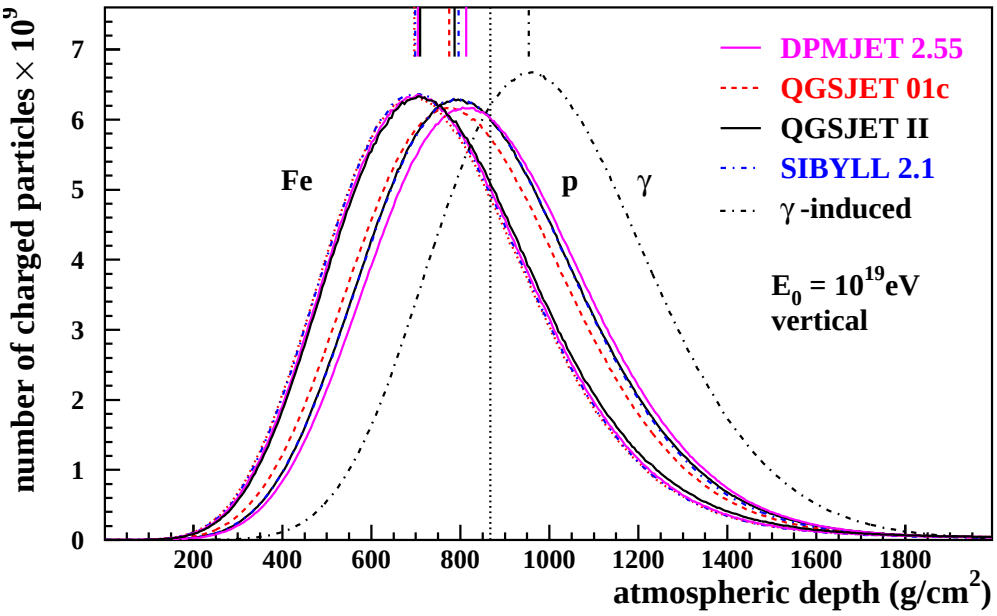


Figure 1.14: Simulated longitudinal profiles for proton, iron and photon primaries with an initial energy of $10^{19}$ eV and arriving at a zenith angle = 0° .

shower interactions. The particle distribution is symmetric around the axis and its density falls with the distance to the core (Figure 1.13). Although the density distribution is characterized by the Molière radius [41], about 100 meters at ground level [40], in the higher energy events it is possible to detect particles some kilometers away from the core. Surface detectors measure essentially the lateral distribution of the density of particles in the shower.

The energy of the primary is determined in surface detectors (in an indirect manner) from the measured lateral distribution. Essentially, a Monte Carlo program is used to simulate high energy showers in the atmosphere, predicting the relation between energy and particle density. At the ground, one of the main indicators of the primary mass is the shower muon content. Thus, surface arrays use muon separation capabilities, both direct (placing underground muon counters) or indirect (separating the detector signal due to muons) to achieve mass composition sensivity. Its also possible to study the primary mass using the timing of the shower front: since muons suffer less scattering they tend to arrive earlier than the electromagnetic component [42].

Surface detectors use generally scintillators or water Čerenkov tanks as their detector stations. Water Čerenkov tanks have broader angular coverage,

compared to thin scintillators which are usually more difficult to build and deploy. Both methods are robust and reliable, well known, detectors adequate to instrument the required large areas.

### Fluorescence detectors

Fluorescence detectors record the near UV light emitted by deexcitation of $N_2$ molecules previously excited by the shower particles. They provide a direct measurement of the longitudinal shower development (Figure 1.14). This is crucial, because the integral of the profile is a direct measurement of the energy deposited in the atmosphere. Moreover, the depth of the shower maximum is also a good indicator of the primary mass. Three factors limit the ability to study cosmic ray primary composition: intrinsic fluctuations on shower development, finite detector resolution and systematics and limited knowledge of high energy hadronic interactions.

# Chapter 2

# The Pierre Auger Observatory

The Pierre Auger Observatory [43], operated by an international collaboration, is conceived with the aim of measuring the spectrum, arrival direction and composition of UHECR with unprecedented statistics and with low systematic uncertainties.

The Southern Observatory, completed in May 2008, is located near the town of Malargüe in Argentina. at the latitude of 35° South. The northern site is in its planning stage, in southeastern Colorado near the city of Lamar, at an altitude of 1100 m above sea level (a.s.l.) and at the latitude of 38° North. Both Observatory provides a full sky coverage when combined.

The need of full sky coverage is motivated by anisotropy studies, point source determination and correlations with astrophysical objects, as well as for determining the cosmic ray flux in different regions of the sky, since a different energy spectrum could give insides into different mechanisms of particle acceleration at the source.

The design incorporates two measurement techniques used with success in the past: detecting the Nitrogen fluorescence in the atmosphere caused by particles of the extensive air shower and measuring the lateral distributions of particles that reach the ground. It consists of an array of water Čerenkov detectors covering 3000 $km^2$ with about 1600 detectors spaced 1.5 km apart in a triangular grid. The mean ground slope of less than 1% and the altitude of 1400 m ensures a measurement of the air shower at the same shower age, close to the maximum of the shower development of cosmic rays in the EeV range. On the edges of the Surface Detector array there are 4 fluorescence detector sites, each with 6 telescopes. The layout of the Southern Observatory is shown in Fig. 2.1.

The large surface detection area allows the collection of a large amount of statistics for analysis in a reasonable amount of time. With both detector sites completed and operational, the cosmic ray flux will be measured within

50 days with more statistics than the total of all experiments in the last 30 years. The stereo observation mode, by two or more fluorescence detectors, allows the understanding and the evaluation of the systematic effects arising from varying atmospheric conditions.

Most importantly the golden hybrid events, air showers recorded and reconstructed with both techniques, are useful for inter-calibration and data consistency checks.

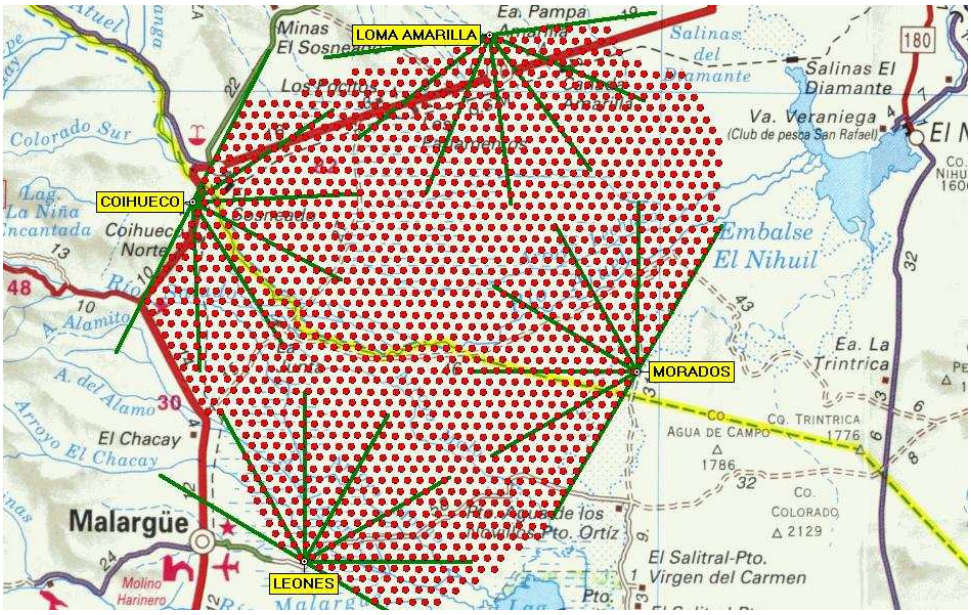


Figure 2.1: The Pierre Auger Observatory, the red point are the Čerenkov counters, the 4 sites for the fluorescence telescope are indicated by names.

## 2.1 Surface Detector

The Surface Detector measures the front of the shower as it reaches ground. The tanks activated by the event record the particle density and the time of arrival. A wireless local area network (LAN) is used to communicate the tanks with four antennas at each fluorescence site. From there, the data is routed through a high capacity microwave link to the central data acquisition system (CDAS). Synchronization is provided by the standard GPS system.

### 2.1.1 Surface Detector unit

The cell unit of the Surface Detector (SD) of the Pierre Auger Observatory is a water Cherenkov counter. Each counter is a polyethylene tank of cylindrical shape with size 10 $m^2$ x 1.2 m filled with purified water. Cherenkov light produced by charged particles of the showers is detected by three 9" photomultipliers. Each unit is autonomous with a battery and a solar panel (Fig. 2.2). Tanks are calibrated using the signals of atmospheric muons, a

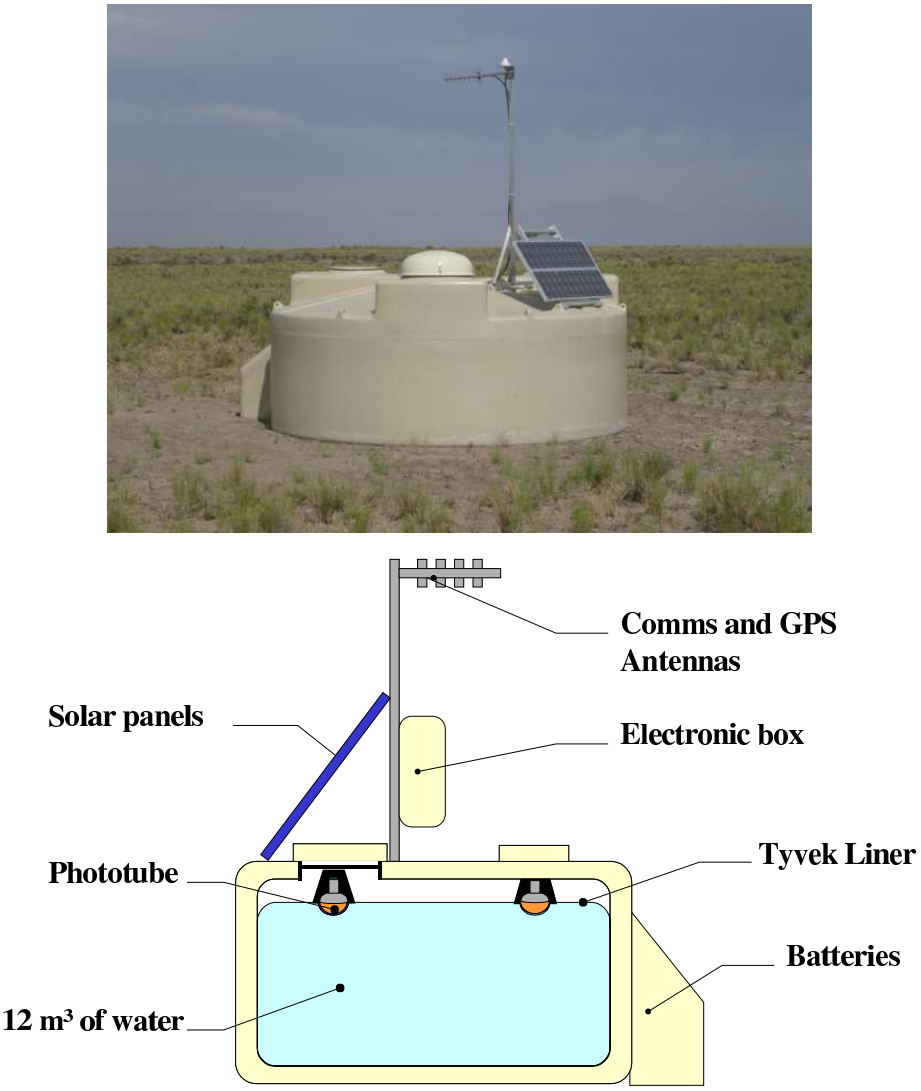


Figure 2.2: A picture (up) and a schematic view (down) of a Surface Detector unit.

well known uniform background across the array. The signal of a muon is

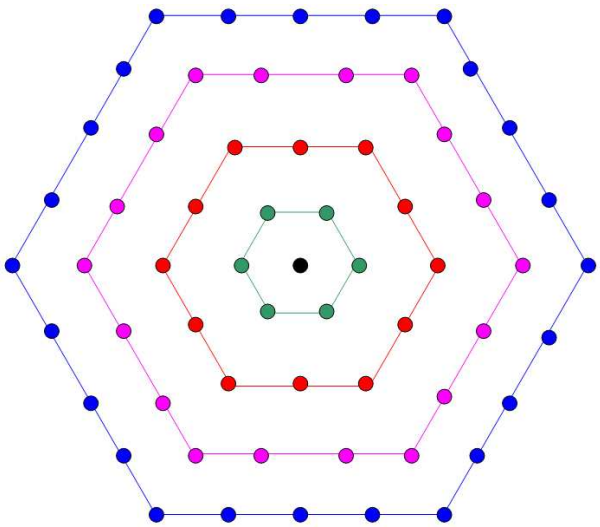

Figure 2.3: Topology of the concentric rings or hexagons used for T3 trigger decision [44].

proportional to the geometric path length. A test tank was used to establish the relation between the signal of down-going vertical and central muons (VEM) and the peak of the histogram obtained from omni directional muons crossing the tank. Each station is calibrated matching the photomultipliers gain to obtain the expected trigger rate over a given VEM threshold. This procedure allows to calibrate the stations with respect to the absolute value of the VEM with an overall precision of 5%.

### 2.1.2 Data acquisition and triggers

Each station is equipped with three photomultipliers [45]. Two signals are extracted from each tank PMT Photonis XP1802: the signal from the last dynode and that from the anode. The last dynode signal is amplified to match the dynamic range. The anode is used for high signals such as seen when the station is near the core of the shower. The six signals from each tank are digitized by 10 bit fast analog to digital converters (FADCs) running at 40 MHz.

There are two types of local station triggers (T1): *single threshold*, a 3-fold coincidence of signals above 1.75 VEM and *time over threshold*, a 2-fold coincidence of 12 bins above 0.2 VEM within a 120 bins (a 3 $\mu$s window). T1 trigger rate is around 110 Hz. Upon a trigger, 256 pre-trigger and 512 post-trigger bins are stored in local buffer waiting for further trigger decisions to be taken.

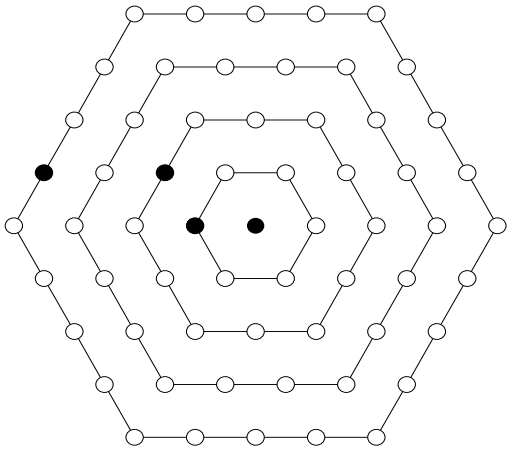

Figure 2.4: Illustration of a minimum "2C1&3C2&4C4" condition. Triggered tanks are represented as full points. The first ring has one trigger (2C1 condition). The triggered tank in the second ring fulfills the 3C2 condition. The last tank can be as far as in the fourth ring because of the 4C4 condition.

The second level trigger (T2) is a software station trigger. All time over threshold triggers, and all threshold triggers above 3.2 VEM, are designated as T2. The local station controller, a CPU board running under the OS9 operating system, provides the T2 trigger decision as well as the handling of the GPS timing board, of the slow control board and of the forwarding of T2 triggers to CDAS. The rate of T2 triggers is around 20 Hz.

Whenever a station fulfills one of the T2 trigger condition, the trigger timestamp and the type of trigger are forwarded to CDAS. Within CDAS the central trigger receives the T2 and is used to identify groups of stations that are clustered in time and space to form a T3 trigger. Placing a 25 $\mu$s window at a given T2, the stations that have a trigger within this window are examined for spatial correlation. At least three T2 triggered stations are required (4-fold condition). At least one of the three has to be in one of the six adjacent stations that are closer to the triggered tank used as the time window center (the *first ring*, figure 2.3). Two of the three have to be within the second ring. The third has be within the fourth ring. This is known as the "2C1&3C2&4C4," mCn meaning m triggered stations within the nth ring (see figure 2.4). In case of time over threshold (ToT) triggers, 3-fold coincidences fulfilling a "2C1&3C2" condition are also considered for a trigger. Once the spatial coincidence is verified, a final timing criteria is

imposed: each T2 must be within $(6 + 5n)$ $\mu$s of the central one, where $n$ represents the hexagon number. If this latter condition is fulfilled, the event is considered a T3 and CDAS requests the FADC data from the triggered stations.

The total trigger rate depends on the array size and CDAS can adequately handle rates at the level of 0.01 Hz. As the array is growing, the T3 trigger conditions are being strengthened to keep acceptable trigger rates.

The lowest CDAS trigger (T3) identifies time coincidences between the signals in different tanks that could be associated with a real air shower. It does not guarantee that the data are physics events while a large number of chance coincidences in accidental tanks is expected due to low energy showers and to single cosmic muons. It considers any of the following requests:

- a 3-fold condition, which requires a coincidence within a time interval depending on the distance of three tanks passing the ToT condition.

- a 4-fold coincidence which requires the coincidence within a time window depending on the tank distance among 4 tanks having passed any T2 condition, with 2 tanks inside 2 hexagonal crowns from a triggered tank and a further one within 4 crowns. A crown is formed by the stations at equal distance from the center one and are numbered depending on this separation.

- a 3-fold condition which requires the coincidence of three aligned tanks passing any T2 condition.

- an external condition generated by the fluorescence detector (FD).

Every time a station has a T2 trigger it sends a signal to the CDAS containing the trigger time. The station trigger times are sorted. One by one all stations within a sliding time window of 50 $\mu$s are searched for the above patterns. If a pattern is found, the search stops and a first event trigger is formed.

For every event, a readout of the entire array is done. Some other information, e.g. the station position, id, calibration histograms and an error code, are also stored in the data file.

The T3 trigger does not ensure that the events that are taken are physical events, but the philosophy is that a large set of events is recorded among which all the physical events are contained and the sorting is left for a subsequent analysis.

The first physics trigger (T4) was designed to distinguish air showers from random coincidences of single atmospheric muons and is also the first step to select reconstructible vertical events. It consists of:

- 3ToT trigger requires at least 3 stations with a ToT trigger in a non-aligned configuration. This simple compact trigger is not effective for events with large zenith angles due to the dominance in this case of the muonic component which gives origin to fast less spread signals. This requirement selects 99% of the events with zenith angle less than 60 (Fig. 2.5).

- 4C1 trigger is passed only by events that have 4 tanks with a T2 trigger each, and a configuration of one station with 3 close neighbors (Fig. 2.6).

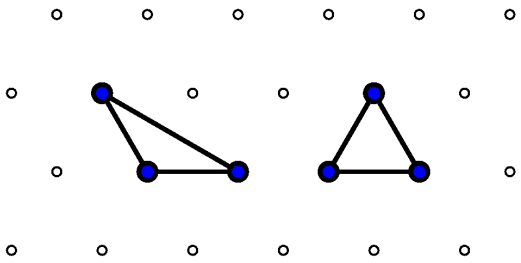

Figure 2.5: Two possible 3TOT compact configurations.

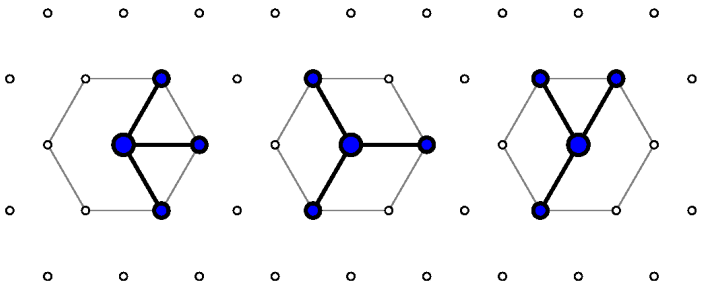

Figure 2.6: The three (minimal) 4C1 configurations.

In all cases of the T4 trigger, compatibility in time between stations part of the trigger is required. The difference in their start time has to be lower than the distance between them divided by the speed of light, allowing for a marginal limit of 200 ns.

The quality trigger (T5) is meant to exclude events that fall too close to the edge of the SD array. For this class of events, due to a possible missing

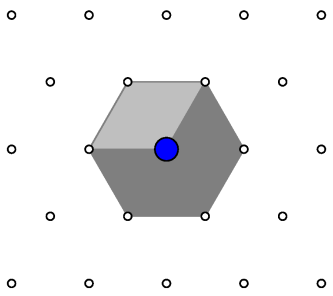

Figure 2.7: The T5 configuration. The central station (blue) with the largest signal is surrounded by 6 functioning stations.

signal, the reconstruction of the air shower variables may not be reliable. Another reason is that it is very hard to compute the acceptance which would take into account events that are highly energetic but far away from the array. In such cases the trigger probability for 4 tanks on the edge of the array depends on fluctuations which are very hard to simulate.

This quality trigger is based on a criterion related to the core position: for the station with the largest signal it is required to have six nearest neighbors that were present and functioning (but not necessarily triggered) at the time of the shower impact (Fig. 2.7). This assures a good and unbiased reconstruction of the event.

## 2.2 Fluorescence Detector

The fluorescence detector (FD) consists of 24 telescopes located at four site, which are built on small elevations on the perimeter of the array (Fig. 2.1). The telescopes measure the shower development in the atmosphere by collecting the fluorescence light emitted by the atmospheric nitrogen molecules excited by the charged particles of the shower.

Each telescope is composed by an aperture system, a spherical mirror, and a 440 photomultiplier camera in the focal plane. A schematic view of the arrangement can be seen in figure 2.8. From left to right: shutters, aperture system with holding mounts for filter and corrector ring; camera with its support, mirror with support structure and, on the floor, the electronics crate.

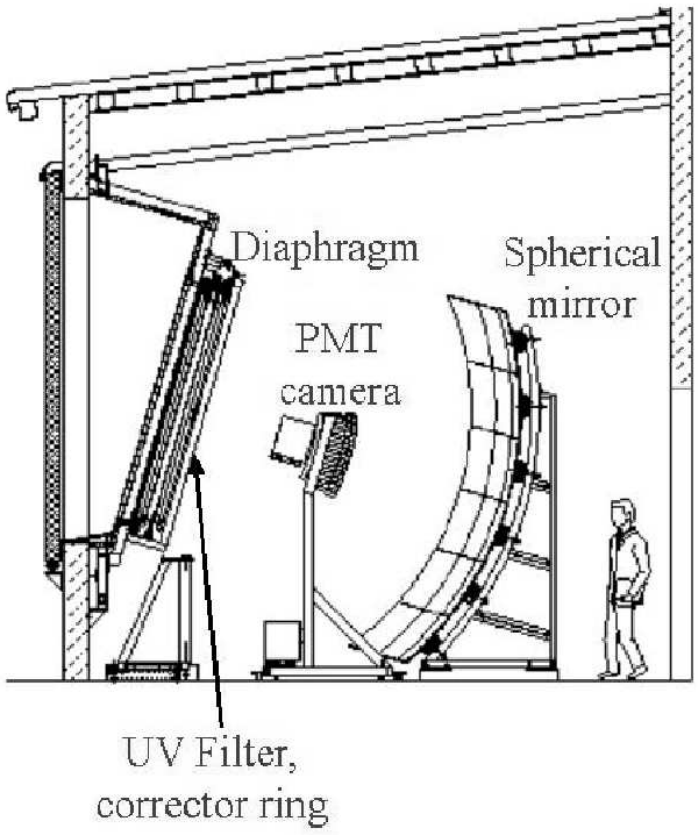


Figure 2.8: A schematic view of the fluorescence telescope.

### 2.2.1 Optics

Each fluorescence telescope cover 28.6° in elevation (from 2° to 30.6°) and 30° in azimuth. To achieve this large field of view with good optical quality the general layout of a Schmidt telescope has been adapted [46]: a diaphragm is used to limit the dimension of the aperture. The choice of Schmidt optics gives the advantage of eliminating coma aberration: the circle of least confusion, *spot*, caused by spherical aberration, is practically independent of the incident direction. The main disadvantage is that the focal surface of such a system is spherical, slightly complicating the camera design.

The diameter of the diaphragm is 1.7 m, giving an effective area for light collection of 1.5 $m^2$, after taking account of the shadow of the camera. The radius of curvature of the mirror is 3.4 m, and the angular size of the spot from spherical aberration is 0.5°, i.e. $\frac{1}{3}$ of the pixel size.

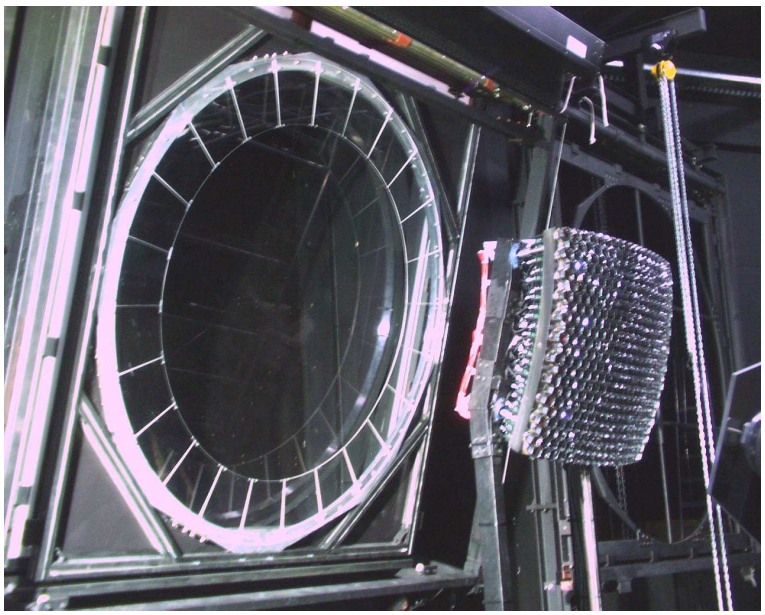

Figure 2.9: Picture of a corrector ring, placed on its position in the aperture system.

As an extension of the Schmidt optics, a corrector ring is used to increase the light collection at the diaphragm maintaining the spot size [47]. Currently all the telescopes are equipped with corrector rings.

### Aperture

The aperture system holds the diaphragm for the Schmidt optics design, the corrector ring, and an UV transmitting filter. The idea of an optical filter is to transmit most of the fluorescence signal in the near-UV while blocking other night sky background to which the PMTs are sensitive. The filter acts also as the window of the bay, protecting the telescope from the external environment [48]. Sheets of M-UG6 glass, 3.25 mm thick, are used. The filter efficiently transmits the nitrogen fluorescence spectrum in the near-UV, while blocking almost all visible light, which would increase the background noise. A simple, but robust, support structure holds the glass sheets of $80 \times 40$ cm$^2$ in place. The transmission curve peaks at about 85% for the wavelength of 350 nm and drops down to nearly 20% at 300 nm and 400 nm.

The background reduction due to the filter is a factor of 8. Since the fluctuations of the noise vary with the square root of the background, the expected signal to noise ratio improvement is factor of 2 [49].

The aperture can hold a 1.7 m diameter diaphragm mask or alternatively

the annular corrector ring [50], that increases the aperture to 2.2 m diameter. The corrector ring, of annular shape, has radial extension of 25 cm (inner radius of 0.85 m, as the original aperture, and outer radius of 1.10 m, figure 2.9). It is constructed from 24 sectors made of UV transmitting glass, machined with an appropriate spherical profile to compensate for the spherical aberration. The corrector ring nearly doubles the reference aperture area while maintaining essentially the same spot size.

#### Mirrors

The mirrors are of square form, 3.8 m×3.8 m in size, and are built up from smaller pieces held by a single common structure. The mirror pieces are attached to the supporting structure by means of an adjustable mount that allows the optimization of the orientation of the mirror segment to obtain a good overall alignment of the whole mirror.

There are two types of mirror segments: square aluminum mirrors and hexagonal glass mirrors [49]. They all share common performance requirements, in particular 90% reflectivity between 300 and 400 nm and have a radius of curvature of 3.4 m.

Single mirrors are built upon 36 mirror segments (figure 2.10) aligned with respect to a removable reference point, placed on a strong and precise mechanical support, corresponding to the center of curvature of the mirror.

### 2.2.2 The camera

Because of the symmetry of the optical system, the actual focal surface is spherical in shape. It is concentric with the mirror and has a radius of 1.743 m, slightly larger than the standard focal length. The camera segments the 30° azimuth × 28.6° elevation field of view into an array of 440 hexagonal pixels, with a 1.5° field of view each [51] (Fig. 2.11).

Each pixel is defined by the light collectors, that improve the camera uniformity and match the variable-size pixels to standard hexagonal photomultiplier tubes, the active light collecting devices. The pixel angular coverage is designed to optimize the signal-to-noise ratio and the sampling resolution of the shower profile.

Each pixel vertex is placed with equal angular separation over the focal surface. Equal steps in angle produce different linear dimensions depending on the pixel position on the spherical surface. Thus, pixels are not regular hexagons and their shape and size vary over the focal surface (figure 2.12). However, differences of the side length are smaller than 1 mm and are taken into account in the design of the light collectors [51].

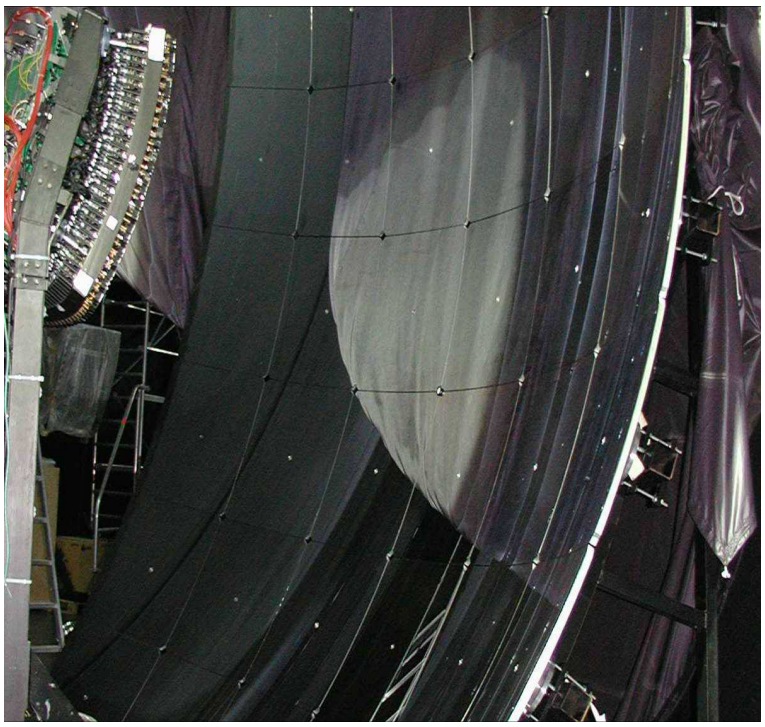

Figure 2.10: Picture of an aluminum mirror, where each one of the single segments can be seen.

### The camera body

Form the mechanical point of view, the main difficulty in camera design is to adapt its shape to the spherical focal surface.

The camera body is made of a single aluminum block. It consists of an accurately machined plate, 6 cm thick, approximately square (94 cm horizontal $\times$ 86 cm vertical) with inner and outer surface of spherical shape. The photomultiplier tubes are positioned inside cylindrical holes which are drilled through the plate. Smaller drills serve as insertion points for the Winston cone holders.

The camera is held by a simple two-leg steel support, that results in an obscuration area less than 0.1 $m^2$ (about one tenth of the camera itself). Power and signal cables run inside the two legs of the support without producing additional obscuration.

Once in place, the camera is aligned with respect to the same reference point as the mirrors, by means of several mechanical adjustments provided in the base of the support and in the camera body fixing system. A $\pm 2$ mm alignment precision is achieved.

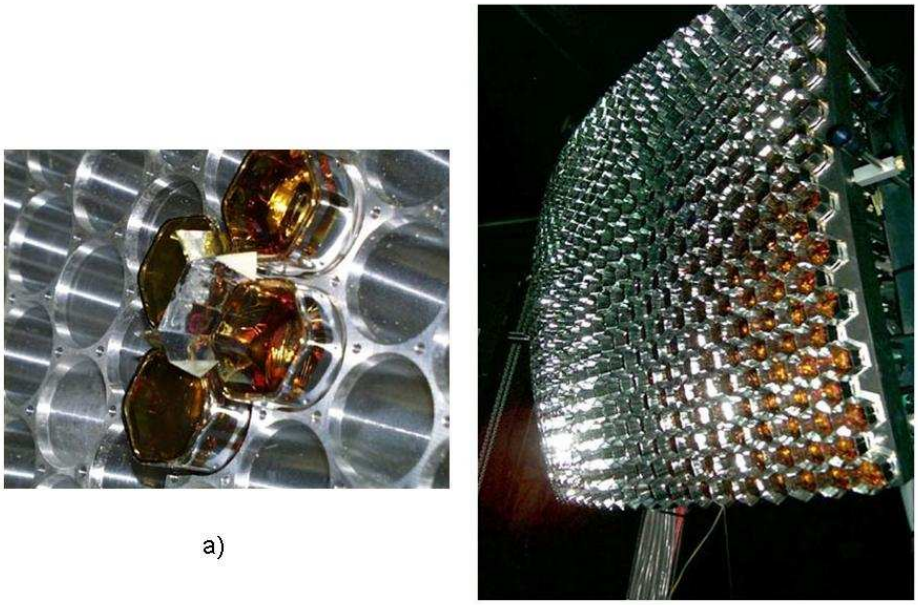

a) b)

Figure 2.11: a) Detail of the camera body with four PMTs mounted together with two *mercedes* stars. The large holes to insert the PMTs and the small ones to mount the *mercedes* are clearly visible. b) Picture of a camera completely assembled with all PMTs and light collectors in place.

### The photomultipliers and the Winston cones

Each pixel is instrumented with an eight-stage photomultiplier (PMT) tube, Photonis XP3062 (Fig. 2.14) , of 40 mm side-to-side hexagonal photocathode, complemented with light collectors. The photomultiplier array is made of 22 rows and 20 columns (figure 2.13). The hexagonal shape of the PMT cathode ensures optimal coverage of the focal surface.

The main characteristics of the PMT tubes are [52]:

**Uniformity of response over the photocathode** The response is uniform, with a maximum $\pm 15\%$ of non-uniformity.

**Spectral response** The PMTs have a 0.25 average quantum efficiency in the range 330-400 nm.

**Gain** The nominal gain for standard operation is around $5 \times 10^4$.

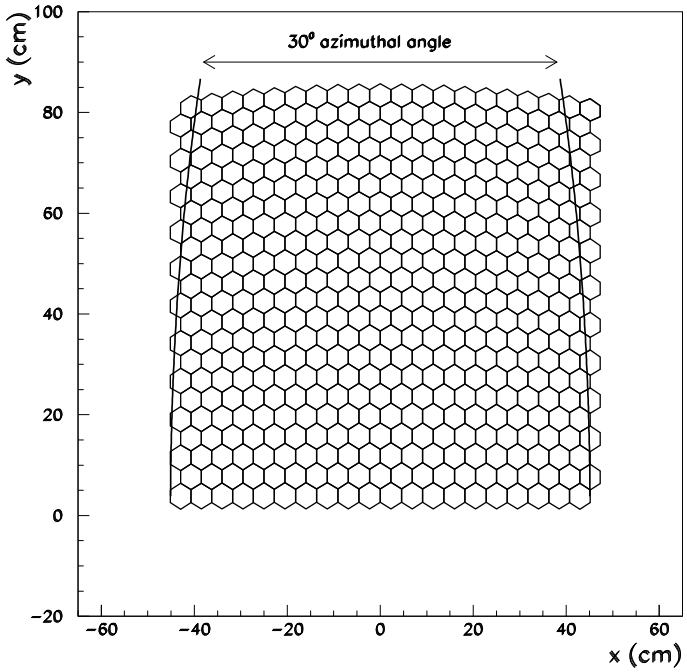


Figure 2.12: The linear dimensions of the pixels vary across the camera, because of the spherical geometry. Due to the details of camera construction there is also a small overlap region in the upper field of view of two neighbor telescopes, given by the pixels placed outside the 30° lines in the sketch.

**Linear dynamic range** The PMT response is linear to better than 3%, over a dynamic range of at least $10^4$ for 1 $\mu s$ signals. The maximum signal for linear response is expected to be 1 mA, corresponding to $6 \times 10^4$ photoelectrons for a gain of $10^5$.

**Integrated anode charge** The total anode charge is not less than 350 C, to ensure the lifetime of the tubes, that will be operated under important levels of background light.

The PMTs are equipped with an active divider chain [53] and a preamplifier. The normal dark sky background induces an anode current at the level of 0.8 $\mu$A. The active divider ensures that the gain shift due to the divider chain is less than 1% for anode currents up to about 10 $\mu$A. Each PMT+base system is tested on a dedicated system, in addition to the test performed in the factory [54].

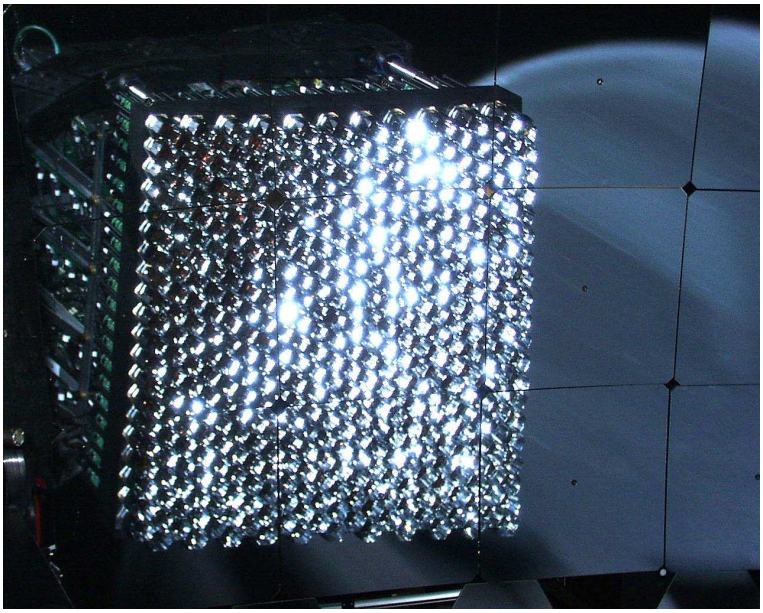

Figure 2.13: The photomultiplier camera and the Winston cones.

The base of the PMTs is soldered an includes two printed boards with the divider chain and the preamplifier [55]. A single cable carries the high voltage, the low voltage and the signal. The other end of the cable is attached to a *distribution board* at the back of the camera [56]. The distribution board serves 44 photomultipliers. Signals are driven through twisted-pair cable to the front-end board. A single power supply serves all the distribution boards of the whole FD site [57].

In order to maximize light collection and guarantee a sharp transition between adjacent pixels, each photomultiplier is surrounded by a simplified version of the classical *Winston cones* [58]. The designed light collectors [59] provide (1) a good matching of the hexagonal pixel geometry, (2) a sharp transition between adjacent pixels and (3) an almost complete recovery of the light falling on the insensitive area due to the space needed for safe mechanical packaging on the focal surface and the effective cathode area, that is smaller than the area delimited by the PMT glass envelope.

The *cone* is realized by a hexagonal set of flat reflecting surfaces. The basic element of the light collector is a *mercedes* star fixed at the vertex of three adjacent pixels (figure 2.15). The arm length is approximately half of the pixel side length while the arm section is an isosceles triangle. The base length of 9.2 mm is designed to match the photocathode inefficiency, 2 mm for each adjacent PMT, plus the maximum space between PMTs glass sides,

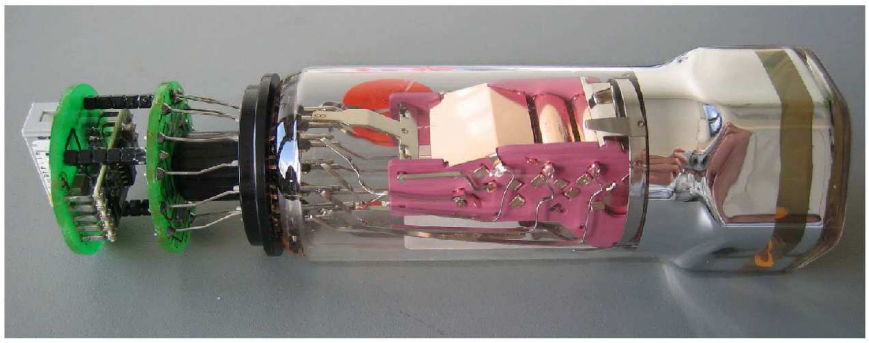

Figure 2.14: Picture of a PMT unit.

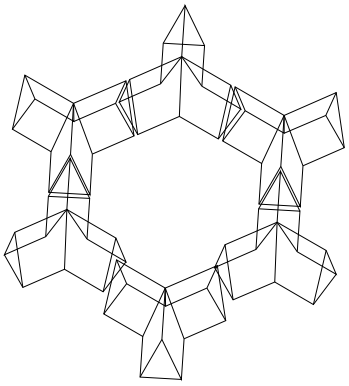

Figure 2.15: Each light collector unit has the form of a three point star. Six collector units correspond to an hexagonal pixel.

of the order of 5 mm. The triangle height is 18 mm, optimized taking into account the optical characteristics of the FD telescope, particularly the fact that the light ray angles of incidence are between 10° and 30°, approximately. The reflective surface is obtained by gluing aluminized Mylar on the mercedes surface.

The properties of the light collectors were tested [59] using a light source filtered in the 300-400 nm region which produced an image that simulated the spot created by the mirror, by means of a light diffusing cylinder. A small version of the full size camera body held seven Photonis hexagonal phototubes XP3062, arranged in a sunflower configuration. The light source was moved over the sunflower surface in steps of a few millimeters.

The recuperation of the light using the light collectors is demonstrated in figure 2.16, where the results of scanning a row of three adjacent pixels is

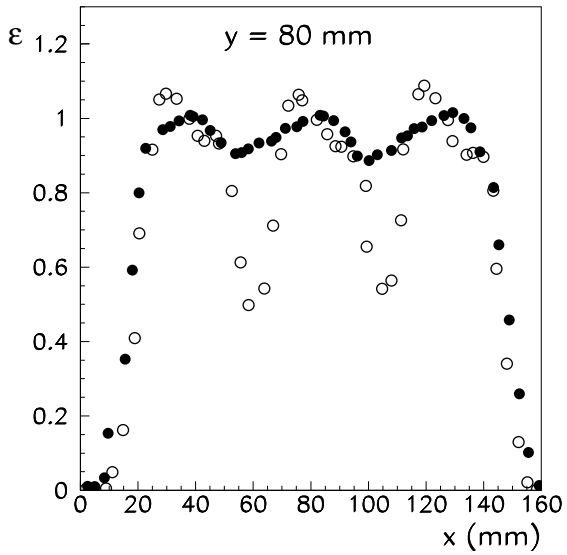


Figure 2.16: Measurement of the light collection efficiency, $\epsilon$, with a light spot moved along a line passing over three pixels. The full dots represent the measurements performed with the mercedes, while the open dots represent the measurements without the mercedes. In limited regions of the photocathode the light collection efficiency can be greater than one since is normalized to the average light collection efficiency integrated over the photocathode surface.

shown. At the photomultiplier edges the efficiency rises from about 50% to more than 90%. The light collectors are efficiently recovering the light loss. The uniformity within a given pixel is also improved, since light rays which were hitting the photocathode edges are now reflected on the mercedes and directed into the central region of the photocathode.

From these measurements, the light collection efficiency, $\epsilon$, averaged over the FD focal surface was found to be 93% [59].

### 2.2.3 Electronics, trigger and DAQ

The fluorescence detector (FD) trigger is a 4 level trigger:

- The pixel trigger is built by four Field-Programmable Gate Arrays (FPGAs), each controlling 6 channels. The FADC values are integrated over 10 bins improving the signal to noise ratio by a factor of $\sqrt{10}$. The threshold is adjusted continuously to achieve a pixel trigger rate of 100 Hz.

- The second level trigger is also decided by the FPGA trigger board. It consists of a purely geometric pattern recognition. It searches for 4 or 5 adjacent pixels overlapping in a time window of 1 to 32 $\mu$s. The rate is 0.1 Hz per mirror.

- The last trigger is implemented in software. It checks for the time structure of an event. The average trigger rate is 0.02 Hz per mirror.

- After the last mirror-level trigger the data are collected by the eye PC, where the events have to pass the eye trigger level T3 which performs rudimentary event reconstruction of the direction and of the time of impact on the ground that is used in CDAS for reading the corresponding part of the array.

The main tasks of the telescope electronics are to shape the PMT signals from FD cameras, to digitize, to store them, to generate a trigger based on the camera image and to initiate the readout of the stored data. A computer network compresses the data, refines the trigger decision, gathers data of the same event from different telescopes and transfers them to the central computing facility, CDAS [60].

The design of the system is aimed to obtain high reliability and robustness for 20 years of operation, good absolute time synchronization with the surface array stations, and flexibility in the trigger scheme.

The organization of the front-end electronics (FE) follows the structure of the telescopes in the FD buildings. Each of the 24 telescopes is readout by one FE sub-rack through its associated Mirror PC. Each sub-rack covers 22×20 pixels of the camera and contains 20 Analog Boards (AB), 20 First Level Trigger (FLT) boards and a single Second Level Trigger (SLT) board [61].

**Analog electronics** The analog signal processing starts at the Head Electronics (HE) which consists of 2 circular printed circuit boards (PCB) mounted directly behind the XP3062 hexagonal PMTs. The inner board holds an active voltage divider which allows the biasing of the PMT dynodes with low power dissipation and high linearity compared to a conventional design [62]. The outer PCB contains a differential-input and a balanced output driver to transfer the PMT signals with low noise and high dynamic range via twisted pair lines to the Analog Boards (AB) at the front-end sub-rack. The driver is located on a small hybrid circuit, which has a symmetrical layout and laser trimmed resistor pairs matched to 0.25% to reduce the common mode noise.

The signals from the camera are processed by 20 AB, i.e. each board serves the 22 channels of a single camera column. The AB holds a differential line receiver, a programmable gain amplifier (to balance the gain spread of the

pixels) and a fourth order anti-aliasing filter in front of the ADC. A 15-bit dynamic range is achieved by introducing an additional low gain channel, which processes the rare large pulses. An on-board test-pulser allows injection of signals with programmable width and amplitude in each channel in order to check the full system even when the camera is not connected [55].

The measured noise for a PMT gain of $5 \times 10^4$ was smaller than 0.5 photoelectrons in a 100 ns, 20% of the expected background due to the diffuse sky light. The cross-talk was smaller than $6 \times 10^{-4}$ and the linearity better than 2% (4% with a large continuous background) [63].

**Digital electronics, DAQ and trigger** The PMT signals are digitized using 10 MHz 12 bit Flash ADCs. The digital part of the front-end board is used to implement all functions of the First Level Trigger (FLT) with reprogrammable logic chips. The trigger logic also implements the calculation of the pixel ADC variance, which is proportional to the DC background light. The knowledge of the background level allows to protect the PMTs against excess of natural or artificial light as well as providing an useful method to study the detector pointing through the record of start tracks [64].

The SLT logic is implemented on a separate board, which is used to read the pixel triggers generated for each channel in the 20 FLT boards. The SLT algorithm is used to search for patterns of five pixels consistent with a track segment, and to generate an internal trigger for data readout. Synchronization with the front-end board is provided by a GPS clock.

The Mirror PC, a robust, disk-less, industry PC associated with each telescope, is used to perform the data readout and the associated software triggers.

The timing synchronization precision is guaranteed using the GPS standard and is monitored through the Central Laser Facility: the same laser signal can be detected by each Fluorescence Detector and fed to a single SD tank (*Celeste*). Such generated events are monitored in search of any timing shifts between detectors [65].

**Slow Control** The task of the FD Slow Control System (SCS) [66] is to control and supervise the operation of each FD telescope. It relies on a series of sensors to monitor the environmental conditions (such as ambient light or wind velocity) and the status of different devices (such as PMTs HV system or shutters).

One of the slow control key aspects is the ability to implement security policies in the data taking context: automatic HV shutdown or shutter closing when ambient safety conditions (i.e. ambient light or wind force) are not

fulfilled.

### 2.2.4 Detector Calibration

Calibration is essential to convert measured ADCs into light fluxes, that can be then translated to energy deposition. The absolute calibration of the fluorescence detectors uses a calibrated 2.5 m diameter light source, the *drum*, at the telescope aperture, providing uniform illumination to each pixel. Uniformity of light emission from the drum surface is important, since the pixels in an Auger fluorescence detector camera view the aperture at varying angles.

The detector is calibrated end-to-end, including optical transmission of the aperture and the mirrors, camera shadow, pixel area, light collection and photomultiplier quantum efficiency. The *drum* illuminator [67] is a pulsed

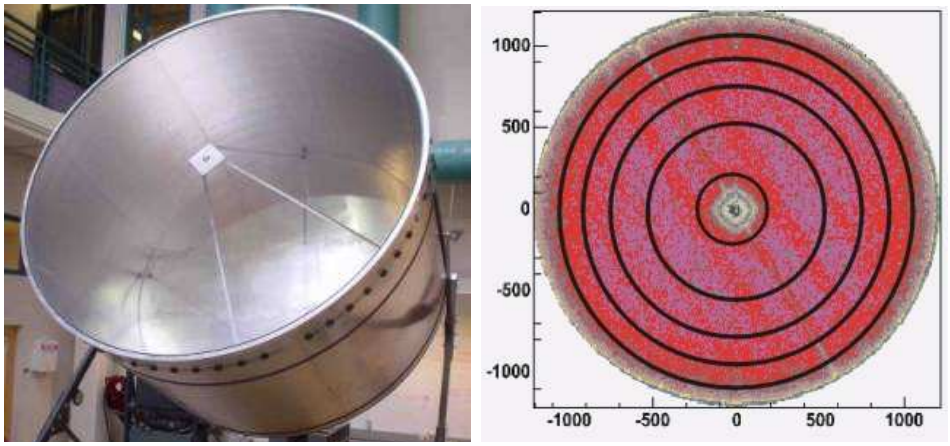


Figure 2.17: Left: photograph of the drum structure. The light source is placed on the mount inside, directed to the rear walls. All the inside walls are covered with Tyvek while a sheet of Teflon is placed on the front. Right: CCD picture of the drum light output. Different colors mean different light intensities. Except for the borders and the central light source shadow the output light intensity is rather uniform. The black concentric circles are drawn to guide the eye.

UV LED, emitting in a narrow band around 375 nm, embedded in a small cylinder of Teflon, illuminating the interior of a 2.5 m diameter cylindrical drum, 1.4 m deep. The sides and back surfaces of the drum are lined with Tyvek, while the front face is made of a thin sheet of Teflon, which transmits light diffusely (figure 2.17).

To calibrate each telescope, the drum is mounted on the the aperture. The provided illumination is uniform within 3%. The drum itself is calibrated using a NIST-calibrated photodiode, that measures the absolute light flux

to a precision of about 7%. The absolute calibration is derived from the telescope response under drum illumination [68].

A cross-check calibration can be obtained firing a nitrogen laser in the telescope field of view [69]. If the laser power is known, the amount of light reaching the telescope comes mainly from the well known Rayleigh scattering, provided that the laser is fired not far from the telescope. Since it depends on atmospheric conditions and requires placing the laser in each one of the telescopes field of view, this method is only used as a cross-check. This absolute calibration of the detector has currently an uncertainty of 12%.

**Relative calibration** An optical system for relative calibration is used to monitor possible time variations in the calibration of the telescopes [70], that are subjected to absolute calibration only from time to time. Three Xenon flash lamp light sources per building, coupled to optical fibers, are used to distribute light signals into three locations at each telescope: the center of the mirror (with the light directed to the camera), the sides of the camera (with the light directed to the mirror through a Teflon diffuser) and the sides of the entrance aperture (with the light directed to a reflective Tyvek target mounted on the telescope doors, from which it is reflected back into the telescope). The optical system is completed with neutral density and interference filters (to monitor the stability at different wavelengths in the range of 330-410 nm).

### 2.2.5 Atmospheric Monitoring

A precise determination of the fluorescence light emitted by the cosmic ray shower must take into account the attenuation of the light in its passage from the emission point to the detector. A detailed knowledge of the scattering properties of the atmosphere and its time dependence is mandatory. A full program, composed of different, complementary approaches is being developed on site [71].

The principal component is the LIDAR, a steerable Laser system capable of measuring the atmospheric aerosol content by the backscattered light signal [72]. The LIDAR is complemented by Horizontal Attenuation Monitors (HAM) that are able to measure the total extinction length between two fixed points and are a cross-check to the LIDAR. Cloud monitors use near infrared photography to check the cloud coverage over the telescopes [73]. The atmospheric monitoring program is completed with the periodic launch of balloon based radiosondes to study the molecular atmospheric profiles [74]. The data is taken every 20 m in altitude until reaching 25 km (a.s.l.). The

profiles are recorded and then compared to the parameterization used previously. If the parameterized values are used instead of the measured profiles, the shower depth at maximum values change on average 15 g/cm$^2$ while the energy changes less than 1%.

**LIDAR** The LIDAR uses a fully steerable alt-altazimuthal frame, one at each FD location, equipped with a UV laser source and three parabolic glass mirrors (Fig. 2.19). The laser is a frequency tripled Nd:Yag laser emitting pulses of 6 mJ energy and 7 ns duration at a wavelength of 355 nm. Each parabolic mirror focus the back-scattered laser light onto a PMT tube. The acquired signal, with a remote controlled DAQ, allows the atmospheric profile to be measured in any direction.

LIDAR operation has two main modes: (1) a continuous sky scan on a $\sim 50^\circ$ cone around the zenith direction, outside the FD field of view; and (2) FD triggered (*shoot the shower* mode) in the region of a recorded event spotted by the online trigger.

The analysis of the LIDAR backscattered light allows the optical depth profiles to be assessed in the horizontal direction up to 25 km, and at elevations up to 20 km, with and expected total error in the attenuation coefficients below 10% [43].

**Central Laser Facility** Located near the geometrical center of the array, the Central Laser Facility (CLF) [75] consists in a calibrated Laser source aimed to provide a *test beam* like light source for the Fluorescence Detector. The CLF is positioned 26 km away from Los Leones eye and 34 km away from Cohihueco eye, adjacent to an SD tank (Fig. 2.18). The light source is a a frequency tripled YAG laser that produces a linearly polarized pulsed beam at 355 nm, of 5 ns duration. It includes an steering system to produce inclined shots.

The CLF is routinely operated by firing 20 vertical shots at 0.5 Hz every 15 minutes. Each 20 shot set is completed with an additional shot that is also fired to the neighbor SD station for timing studies. Inclined shots are fired in an hourly time manner.

Aimed to detector performance and atmospheric monitoring studies, the analysis of the CLF was shown to be useful (but is not limited) to: measure the aerosol vertical optical depth versus height (with different systematics from the LIDAR), monitor FD trigger efficiency, monitor FD timing and FD-SD timing and to study stereo FD energy reconstruction systematics.

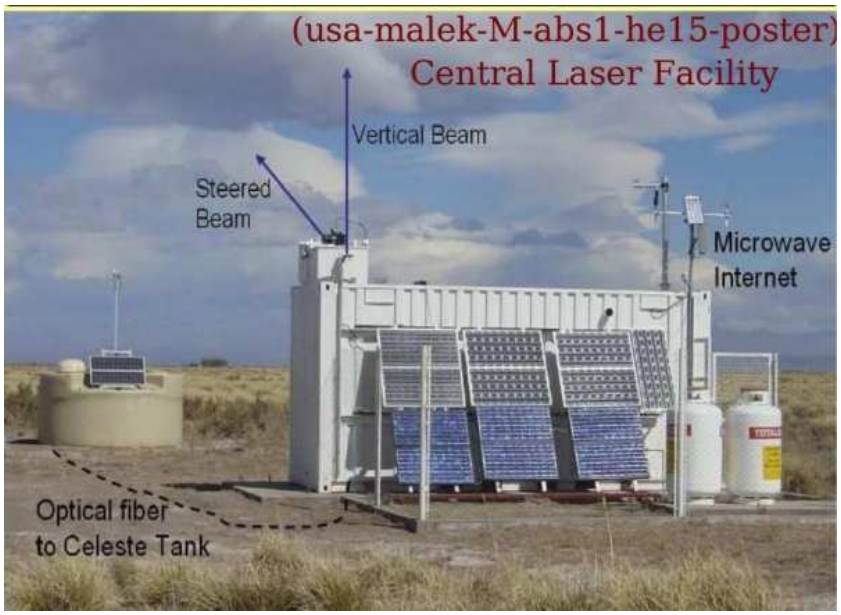


Figure 2.18: The Central Laser Facility with the tank *Celeste*.

Figure 2.19: The LIDAR system.

# Chapter 3

# Event Reconstruction

The air showers recorded by the Pierre Auger Observatory are characterized by triggered stations on the ground array, i.e. discrete samples of the arriving particles in a plane, or by triggered pixels in the fluorescence detectors, samples of the energy deposit in the atmosphere.

From this informations the lateral distribution of the particles on the ground and the lateral development of the shower are reconstructed. The variables important for this work are the S(1000 m), obtained from the SD reconstruction, and the energy of the primary particle, obtained from the FD reconstruction.

This direct energy measurement, independent on shower simulations or hadronic interaction models, will be of extremely importance for establishing the energy scale of the observatory.

In this chapter the way of obtaining these two variables is shown.

The reconstruction is done within the $\overline{\text{Off}}\underline{\text{line}}$ framework [76]. In the next chapter an alternative FD reconstruction methods is proposed.

## 3.1 SD event reconstruction

The reconstruction of events recorded by the SD is performed in two main steps. Firstly, the timing information of the stations is used to reconstruct the shower arrival direction. Once the shower axis has been fixed, a second fit of the station signals is performed to estimate the impact point at ground (from now on the shower core) and the shower size. This last measurement, defined as the signal at a fixed optimal distance $r_{opt}$ from the shower core, will be closely related to the energy of the primary particle.

The criteria used to select $r_{opt}$ is based not only on shower physics but mainly on the spacing of the SD array. For the array spacing used in the

Pierre Auger Observatory (1500 m) the optimum distance has been fixed at 1000 m as demonstrated in [77]. Therefore, the signal size at 1000 m, the so-called S(1000) parameter, will be the observable used as a primary energy estimator.

### 3.1.1 SD Station selection

In order to obtain only signals that belong to the actual air shower is necessary a selection at the level of PMTs and station [78]. The reasons to remove a station from the reconstruction are bad calibrations and/or accidental timing information.

The accidental triggered stations given by the atmospheric muons are removed based on the distance to the first neighbors, requiring at least one other triggered station within 1800 m or more than one within 5000 m, and on timing information, applying the bottom up selection algorithm. This algorithm requires compatibility between the timing in the stations with a planar front propagating with speed of light.

An initial guess of the plane front is done using a seed, the three stations that maximize the sum of signals. If these stations are compatible with the analytical solution the event is considered good enough for a proper reconstruction.

The stations placed outside of the regular grid in order to locally increase the density of the array, infill stations, are rejected.

### 3.1.2 Geometry reconstruction

The shower can be considered as a front of particles propagating with the speed of light along a straight line, the axis, defined by the arrival direction of the primary.

The simplest model of the shower front can be approximated by a plane, perpendicular to the shower axis direction .

An algorithm based on timing information is used to obtain the axis direction given by the unit vector $\overrightarrow{a}$. According to Figure 3.1 the expected time $\widehat{t_i}$ when the shower plane is passing through some chosen SD station located at the point $x_i$ can be estimated as:

$$\widehat{t_i} = \frac{1}{c}\left(ct_0 - (\overrightarrow{x_i} - \overrightarrow{x_b}) \cdot \overrightarrow{a}\right) \tag{3.1}$$

where $\overrightarrow{x_b}$ is the barycenter, a first estimation of the shower impact point $\overrightarrow{x_0}$, calculated as the weighted average of triggered stations, and $t_0$ is the arrival time of the shower front. This expected arrival time $\widehat{t_i}$ can be compared with

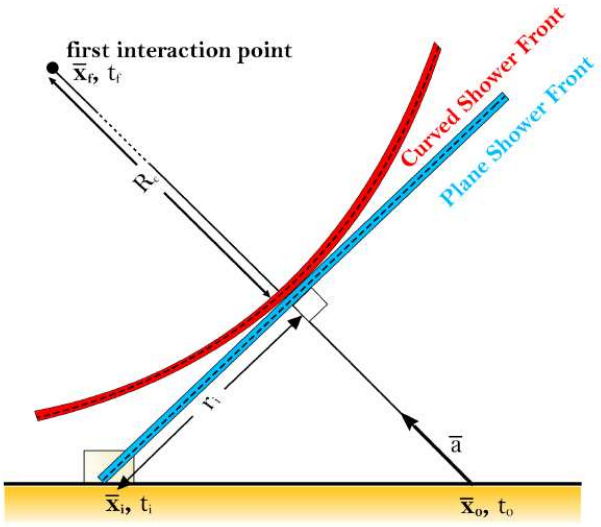


Figure 3.1: Shower geometry including the parameters involved in the SD reconstruction.

the start time measured by the considered station $t_i$ using a standard $\chi^2$ function:

$$\sum_i \left[ \frac{t_i - \widehat{t_i}}{\sigma_{t_i}} \right]^2 \tag{3.2}$$

where the time-variance $\sigma_{t_i}$ in the start time in $n$s units, is defined in [79]. The sum in equation 3.2 runs over all triggered stations. This function will have 3 free parameters: two components of $\overrightarrow{a}$ (the third one is given by the normalization condition) and $t_0$ .

The more realistic shower front model is based on a curved front fit, as illustrated in Fig. 3.1, done by extending the plane fit method with a parabolic term that describes the curvature of the shower front near the impact point. Using the shower-plane distance from the tank to the shower axis $r_i$:

$$r_i = |\overrightarrow{a} \times (\overrightarrow{x_i} - \overrightarrow{x_b})| \tag{3.3}$$

and the radius of curvature $R_C$ of the shower front, the expected arrival time $\widehat{t_i}$ will be:

$$\widehat{t_i} = \frac{1}{c} \left( ct_0 - (\overrightarrow{x_i} - \overrightarrow{x_b}) \cdot \overrightarrow{a} + \frac{r_i^2}{2R_C} \right). \tag{3.4}$$

This corrected time includes a new parameter in the $\chi^2$ fit: $R_C$. For this reason, the shower-front curvature feature is only included for events with at least four triggered stations. In the case of a curved shower front, the

expected arrival time $\widehat{t_i}$ can be also obtained without any assumption about the ground impact point as:

$$\widehat{t_i} = \frac{|\overrightarrow{x_i} - \overrightarrow{x_f}|}{c} + t_f \tag{3.5}$$

where $\overrightarrow{x_f}$ and $t_f$ are the position and time of the first interaction in the upper layers of the atmosphere. This fit does not supply the axis that could be obtained as $\overrightarrow{x_f} - \overrightarrow{x_b}$.

The angular reconstruction accuracy achieved for SD events has been calculated in [80, 81] as a function of the station multiplicity. The angular resolution was found to be better than 1.2° for 4-folds and 5-folds events and better than 0.9° for higher multiplicities.

### 3.1.3 Shower size reconstruction

The station signals are used to infer the shower size and the core position. A Lateral Distribution Function (LDF) models the signals measured in the SD stations as a function of the core distance. The selected LDF used to described the expected signal $S(r)$ measured in VEM units for a station at a core distance $r$ is a modified NKG (Nishimura, Kamata and Greisen) function [82, 83]:

$$S(r) = S(1000) \left(\frac{r}{1000}\right)^{\beta} \left(\frac{r_s + r}{r_s + 1000}\right)^{\beta} \tag{3.6}$$

where $\beta$ is the slope of the LDF, $S(1000)$ the signal in VEM 1 km far from the core and $r_s = 700$.

The slope of the LDF depends on the zenith angle of the shower, $\theta$, as:

$$\beta(\theta) = \begin{cases} a + b(\sec\theta - 1) & , \sec\theta < 1.55 (\theta < 55°) \\ a + b(\sec\theta - 1) + f(\sec\theta - 1.55) & , \sec\theta \geq 1.55 \end{cases} \tag{3.7}$$

where a, b and f can be found in [84]. The $\beta$ parameter dependence on angle can be approximated with: $\beta = (1.17 \sec\theta - 3.69)$ and assume negative value. The set of parameters that best fits the measured signal $S_i$ to the expected one $S(r_i)$ given by equation 3.6 is found minimizing the $chi^2$ function:

$$\chi^2 = \sum_i \left[\frac{S_i - S(r_i)}{\sigma_{S_i}}\right]^2 + \sum_{i,zero\ signal} S(r_i) \tag{3.8}$$

where $\sigma_{S_i}$ is the signal accuracy that have been studied in [85] as a function of the axis zenith angle. The first term runs over all stations with signal. A

second term is added to take into account stations with zero signal but with a non-negligible probability to measure a signal lower than the threshold.

Some stations included in the fit can have a saturated trace, specially those close to the core. Some procedures [86, 87] have been developed to avoid these traces could be lost.

The equation 3.8 has three free parameters to fit: the shower size $S(1000)$, and two components from the shower core (the z component is considered to be the same of the barycenter). The $\chi^2$ dependence on the core position is implicit in the distance since it is a function of the core location, the station position and the axis, where the two last ones are known parameters. The

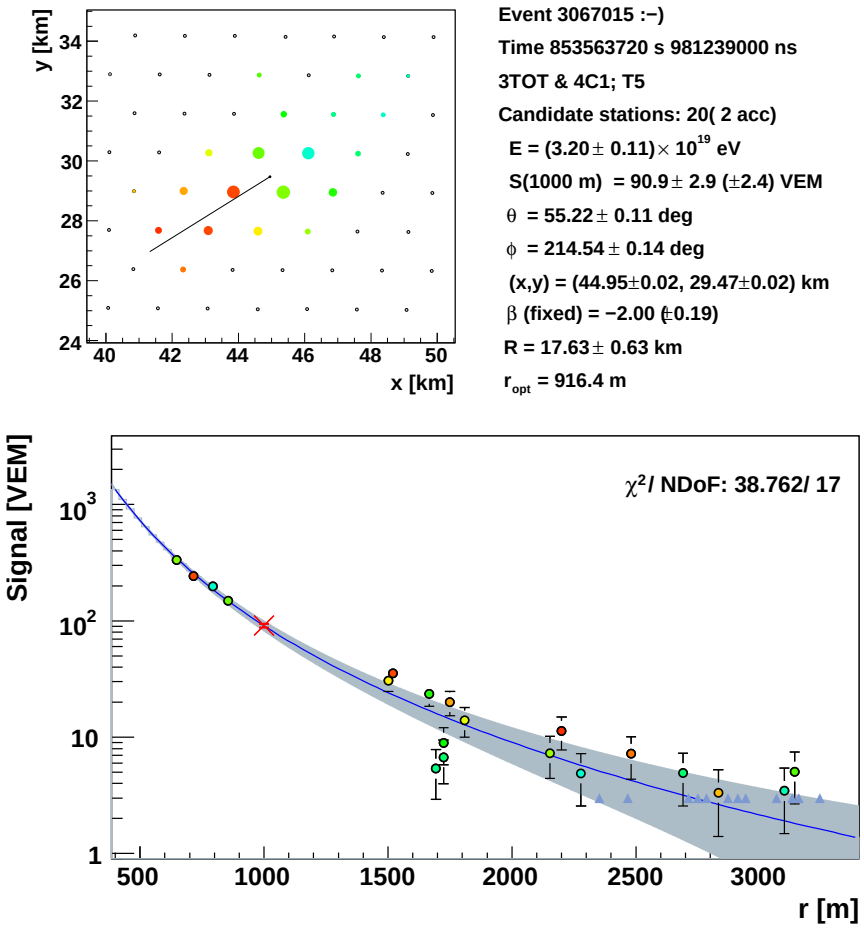


Figure 3.2: Upper left panel:SD stations involved in the event. Upper right panel:Event parameters reconstructed. Down Panel: LDF fit, each color correspond at the tank in the upper left panel.

choice of the signal at $r_{opt} = 1000$ m as the observable to estimate the shower size will be justified. To avoid the large fluctuations in the signal integrated over all distances caused by fluctuations in the shower development, Hillas [88, 89] proposed to use the signal at a given distance, dependent mainly on the spacing of the array, to classify the size of the shower.

In [77] it is shown that at this optimal core distance the fluctuations in the expected signal $S(r_{opt})$ due to a lack of knowledge of the LDF are minimized.

As a final remark it should be mentioned that the validity of the LDF is limited to zenith angles lower than 60° (the so-called *vertical* events).

Primary particles arriving at larger zenith angles develops *horizontal* showers in the atmosphere very similar to vertical ones but the very long path crossed by shower particles prevents the EM component from reaching the earth surface. Only muons survive at ground level but they have been affected by the geomagnetic field deforming the expected symmetrical shape [90].

In Figure 3.2 an example of LDF fit on SD event is shown.

## 3.2 FD event reconstruction

The aims of the FD reconstruction is to estimate the energy needed for the energy calibration of the surface detector. In the first reconstruction step, the signal pulses from individual PMTs are determined, then the geometry of the shower is deduced using the timing from a SD station for the so called *Hybrid event*. Finally the energy is obtained from the total energy deposit in the atmosphere [91].

### 3.2.1 Pixel selection

The data taking software of the fluorescence detectors writes out the ADC-counts for a period of 100 $\mu$s. The stored traces for individual pixels are long enough in time to ensure a properly calculation of the pedestal $n_p$ due to the light background and its fluctuations $\sigma_p$ using the first $N$ time bins. A typical pixel signal is shown in figure 3.3. Each time bin $i$ contains $n^i_{adc}$ ADC counts corresponding to an integration period of 100 $ns$. The $n_p$ and $\sigma_p$ parameters are calculated as:

$$n_p = \frac{1}{N}\sum_{i=1}^{N} n^i_{adc} \tag{3.9}$$

$$\sigma_p^2 = \frac{1}{N-1}\sum_{i=1}^{N}\left(n^i_{adc} - n_p\right) \tag{3.10}$$

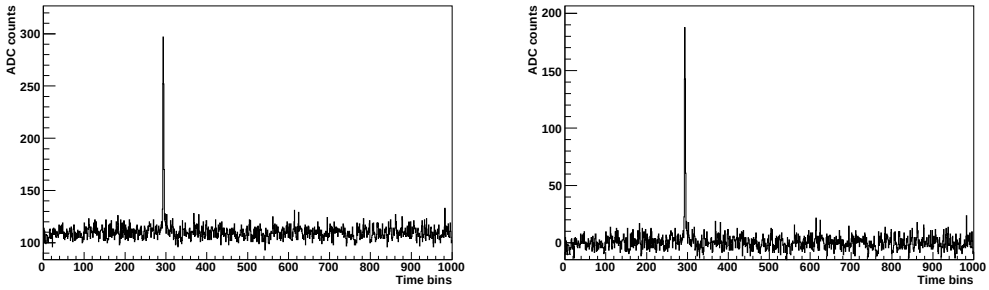


Figure 3.3: Left Panel: Pixel signal. Right Panel: Pixel signal with pedestal subtracted.

The pedestal subtraction allows to convert ADC traces from a given PMT into the equivalent photon traces, i.e. the number of photons that generated the track, as:

$$n_\gamma^i = \left(n_{adc}^i - n_p\right) C_{370} \tag{3.11}$$

where $C_{370}$ is the absolute calibration constant for the considered PMT (Fig. 3.4). To compare this measured flux with the expected at different wavelengths it must be corrected with the detector spectral response relative to 370 nm, the calibration wavelength.

The time interval of the real pulse generated by the shower, is defined by the start $N_{start}$ and stop $N_{stop}$, and it's found maximizing the signal to noise ratio within a time window of 100 bins around the one with the highest signal.

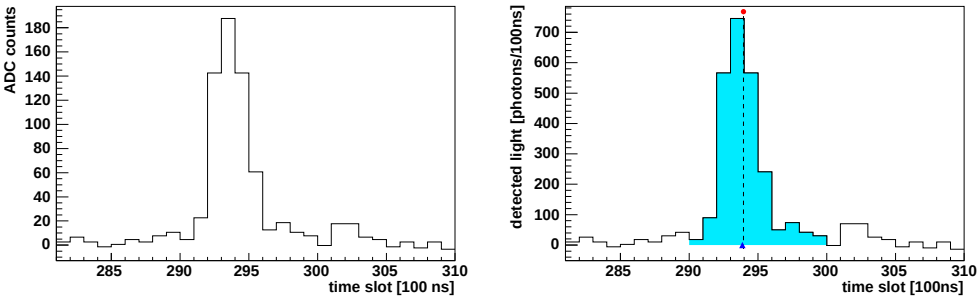


Figure 3.4: Left Panel: Pixel ADC trace. Right Panel: Pixel Photon trace, the pulsed centroid is indicated with dashed line.

### 3.2.2 Geometry Reconstruction

The geometry reconstruction is a two-step process: finding the shower-detector plane (SDP, figure 3.5), the plane defined by the shower axis and the detector center, and finding the shower axis, using the *time fit*. The timing information of the signals is used in the time fit to determine the shower direction within the SDP.

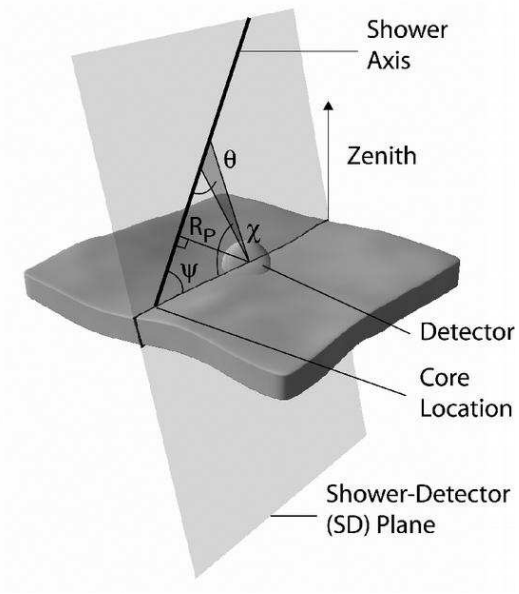


Figure 3.5: Sketch of the shower-detector plane, that contains the shower axis and the detector center.

The best estimate for the normal of the shower detector plane $\vec{n}$ is found minimizing the following $\chi^2$:

$$\chi^2 = \sum_i w_i \left(\vec{r_i} \cdot \vec{n}\right)^2 \tag{3.12}$$

where $\vec{r_i}$ is the pixel pointing direction and $w_i$ a weight proportional to the pixel signal. The sum runs over all the triggered pixels in the event.

The next step is to determine the position of the shower within the SDP using the timing information from the signals recorded by the detector.

For a given shower geometry and timing, the expected arrival time $\widehat{t_i}$ at a pixel $i$ is given by the expression [92]:

$$\widehat{t_i} = T_0 + \frac{R_p}{c} \tan\left(\frac{\chi_0 - \chi_i}{2}\right) \tag{3.13}$$

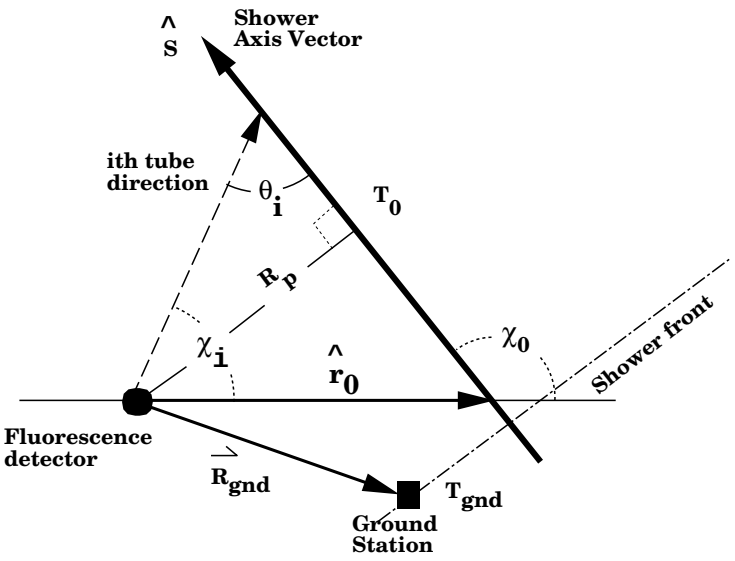


Figure 3.6: Geometry within SDP. The sketch includes a surface detector station outside the shower-detector plane.

where $\chi_i$ is the pixel direction on the SDP, $\chi_0$ is the angle between the shower axis and the vector pointing from the detector to the shower ground arrival point, $R_p$ is the shower distance of closest approach to the detector and $T_0$ the time at which the shower front reaches the position of closest approach (figure 3.6).

The set of parameters ($T_0$,$R_p$,$\chi_0$) that best describes the data is found minimizing the $\chi^2$:

$$\chi^2 = \sum_i w_i \left(t_i - \widehat{t_i}\right)^2 \tag{3.14}$$

where $t_i$ is the measured arrival time for the pixel $i$ and $w_i$ a weight proportional to the pixel signal. The sum runs over all the pixels in the event.

Figure 3.7 shows a time fit example. As can be deduced from the plot, the curvature of the fitted function is crucial, otherwise there are many three parameters solutions to a nearly-straight fit.

One of the methods to overcome the curvature problem in the time fit is the *stereo* detection: by viewing the same shower with two different eyes, the shower axis is determined unambiguously as the intersection between two shower-detector planes. But with the hybrid data there is the possibility of constraining the overall timing using data from the Surface Detector.

It is possible to use the hybrid data to improve the time fit performance. The expected arrival time $\widehat{t_j}$ of the shower from at tank $j$ is, for a given

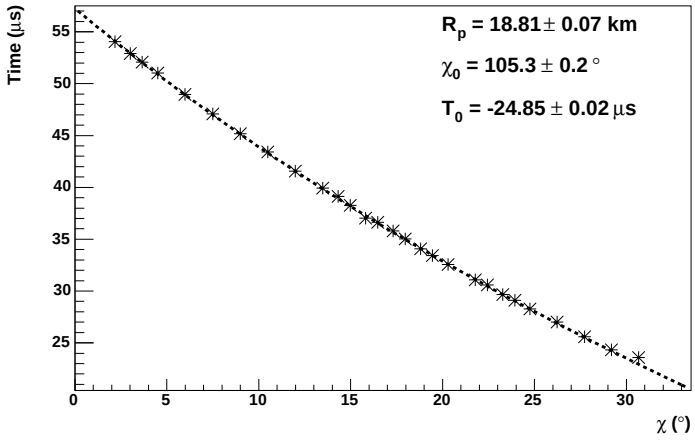


Figure 3.7: Time fit example: experimental points superimposed to the fit result (dashed line). The values of the fitted parameters are shown, with their statistical errors.

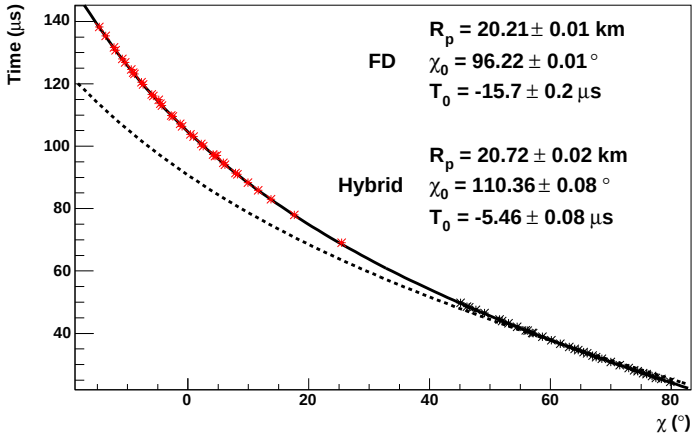


Figure 3.8: Hybrid time fit: Fluorescence Detector data (black points) and Surface Detector data (red points) superimposed to the results of the hybrid (full line) and mono (dashed line) fits. Both fits describe well the fluorescence data, while the $\chi_0$ values are significative different. Errors are only statistical.

geometry and timing:

$$\widehat{t_j} = T_0 + \frac{\vec{R}_{\mathrm{gnd},j} \cdot \vec{S}}{c} \tag{3.15}$$

where $\vec{R}_{\mathrm{gnd},j}$ is the vector from the eye to the Surface Detector tank $j$ and $\vec{S}$ an unitary vector in the direction of the shower axis.

It is possible to define $\chi^2$ term corresponding to the Surface Detector data:

$$\chi^2 = \sum_j \left(t_j - \widehat{t_j}\right)^2 \tag{3.16}$$

where the sum runs for all the triggered Surface Detector tanks.

Now the fit is done minimizing a two-term $\chi^2$:

$$\chi^2 = \chi^2_{\mathrm{FD}} + \chi^2_{\mathrm{SD}} \tag{3.17}$$

each one using one of the detectors data.

Figure 3.8 is an example of hybrid time fit. The improvement with respect to the mono fit is evident.

### 3.2.3 Longitudinal profile reconstruction

The next step is to determine the longitudinal development of the shower in order to obtain the physically relevant quantities. The longitudinal development is parameterized with the *Gaisser–Hillas* function [93]. It is a 4-parameter function of the atmospheric slant depth $X$:

$$N_e(X) = N_{max} \left(\frac{X - X_0}{X_{max} - X_0}\right)^{\frac{X_{max}-X0}{\lambda}} \mathrm{e}^{\frac{X_{max}-X}{\lambda}} \tag{3.18}$$

where $N_{max}$ is the shower size at the maximum and $X_{max}$ the atmospheric depth at which the shower maximum takes place (*the depth of the maximum*). $X_0$ and $\lambda$ are related to the depth of the first interaction and the primary interaction length in air, respectively.

Using the fitted geometry and a set of Gaisser–Hillas parameters, the light fluxes can be estimated and compared with recorded data.

The first step of shower reconstruction is to determine the light flux profile, that is, the photons arriving at the detector diaphragm during each 100 ns time bin. Using the reconstructed geometry, the atmospheric slant depth, $X$, can be calculated for each of the time bins. The light profiles can be *represented* as a function of $X$.

Due to the finite size of the optical image, the signal, at a given time, can be spread over more than one pixel. The total signal is recovered summing

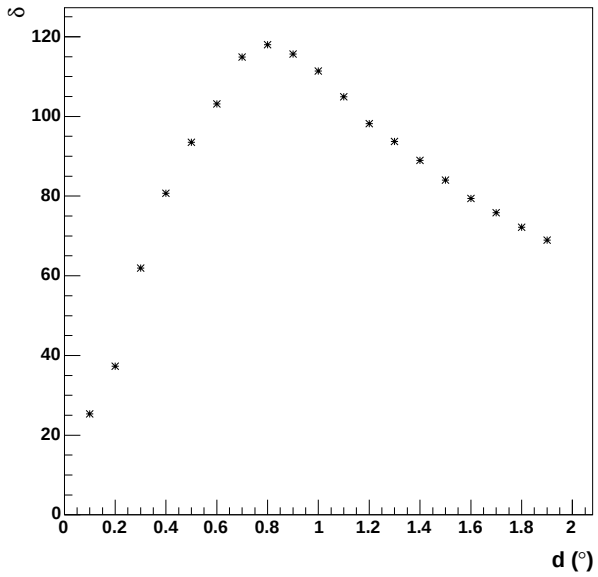


Figure 3.9: Signal over noise ($\delta$) as a function of the maximum accepted angle between pixel direction and image position direction, $d$, for an example event. The angle that maximizes signal to noise is $d(\delta_{max}) = 0.8^\circ$ so the reference angle used to reconstruct the profile would be in this case $d_{cut} = 1^\circ$.

over the channels that, being close to the fitted geometry, are expected to have signal.

A pixel signal is selected provided the angle between its alignment direction $\vec{R_p}$ and the direction of the image position $\vec{R_t}$

$$d_{pix} = \arccos\left(\vec{R_p} \cdot \vec{R_t}\right) \tag{3.19}$$

is less than a given value $d$. The *signal to noise* ratio, $\delta$, can be calculated considering all pixels within $d$ and summing over the entire trace

$$\delta = \frac{\sum_t \sum_{d_{pix}<d} [n_{adc}(t_i) - n_{ped}]}{\sqrt{\sum_t \sum_{d_{pix}<d} \sigma^2_{ped}}} \tag{3.20}$$

where $n_{adc}(t_i)$ is the FADC trace value at time $t_i$ and $n_{ped}$ and $\sigma_{ped}$ are the mean and the sigma of the pixel's baseline, calculated from the very first 100 pre-trigger FADC bins. The angle $d_{cut} = d(\delta_{max}) + 0.2^\circ$ (where $d(\delta_{max})$ maximizes signal to noise ratio, figure 3.9) is the reference angle used to reconstruct the light profile.

Once $d_{cut}$ has been fixed, the light flux, expressed as 370 nm equivalent photons in 100 ns time bins $t_i$, is calculated as:

$$n_\gamma^{370}(t_i) = \sum_{PMT} C_{PMT}^{370} \cdot (n_{adc}(t_i) - n_{ped}) = \sum_{PMT} C_{PMT}^{370} \cdot n_{ADC}(t_i) \qquad (3.21)$$

where the sum runs for PMTs with $d(t_i) < d_{cut}$. For simplicity the pedestal-subtracted ADC value is noted as $n_{ADC}(t_i)$ The absolute calibration constants of the photomultipliers, $C_{PMT}^{370}$ (in 370 nm photons at diaphragm/FADC count units) are obtained with the *drum*.

The error assigned to light profile points is based on two main sources of fluctuations in the photomultiplier signal: cathode photoelectrons and secondary electron emission in dynode chain.

The digitized photomultiplier signal, $n_{ADC}$ is proportional to the number of photoelectrons extracted from the cathode, $n_{p.e.}$:

$$n_{ADC} = \alpha \, n_{p.e.} \qquad (3.22)$$

where the proportionality constant $\alpha$ depends on photomultiplier and electronic gains ($\alpha \simeq 1.8(ADC/p.e/100ns)$ [94] for the FD photomultipliers at the working gain).

When considering fluctuations on photoelectron and secondary electron emission, the usual Poisson expression* becomes [95]:

$$\sigma_{ADC}^2 = \alpha(1 + v_g) n_{ADC} \qquad (3.23)$$

where the $v_g$ term accounts for the mentioned fluctuations the dynode chain. The $v_g$ value depends on the dynode chain characteristics. For FD photomultipliers $v_g \simeq 0.4$.

Finally, adding baseline fluctuations in quadrature:

$$\sigma_{ADC}^2 = \alpha(1 + v_g) n_{ADC} + \sigma_{ped}^2 \qquad (3.24)$$

and transforming to 370 nm photons at diaphragm, leads to the expression for the $n_\gamma^{370}$ errors:

$$\sigma_\gamma^{370}(t_i) = \sqrt{\sum_{PMT} (C_{PMT}^{370})^2 \left[\alpha(1 + v_g) n_{ADC}(t_i) + \sigma_{ped}^2\right]} \qquad (3.25)$$

where $n_{ADC}(t_i)$ is the pedestal subtracted ADC value.

Figure 3.10 presents two examples of raw ADC (pedestal subtracted) profiles and their corresponding light profiles. The upper plots are the ADC

*$\sigma_{p.e.} = \sqrt{n_{p.e.}} \Rightarrow \sigma_{ADC}^2 = \alpha^2 n_{p.e.} = \alpha \cdot n_{ADC}$

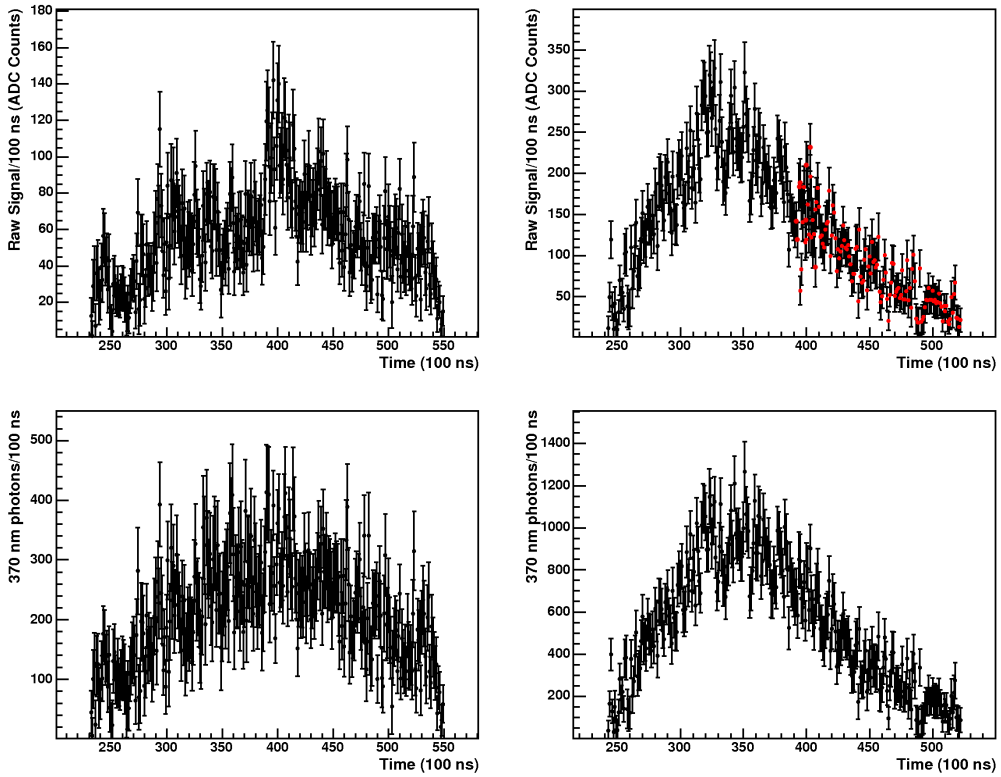


Figure 3.10: Two examples of ADC and photons at diaphragm profiles. The upper plots are the ADC profiles (pedestal subtracted) in original 100 ns bins. The upper right plot is a two mirror event, with the second mirror points in red. The bottom plots are the same events in terms of photons at diaphragm. In the mirror overlapping region the bin with higher data has been chosen.

profiles (pedestal subtracted) in original 100 ns bins. The upper right plot is a two mirror event, with the second mirror points in red. The bottom plots are the same events in terms of photons at diaphragm.

Up to now the number of photons have been defined as a function of the collection time. From now on it is more useful to define the signal as a function of the atmospheric depth in order to obtain the longitudinal profile. The light arriving at a given time $t_i$ was generated at some point on the shower track corresponding to a height $z_i$ that can be calculated from the shower geometry. The corresponding atmospheric depth $X_i$ will be given by:

$$X_i = \int_{z_i}^{\infty} \rho\left(z\right) \frac{dz}{\cos\theta} \tag{3.26}$$

where $\theta$ is the zenith angle of the shower axis.

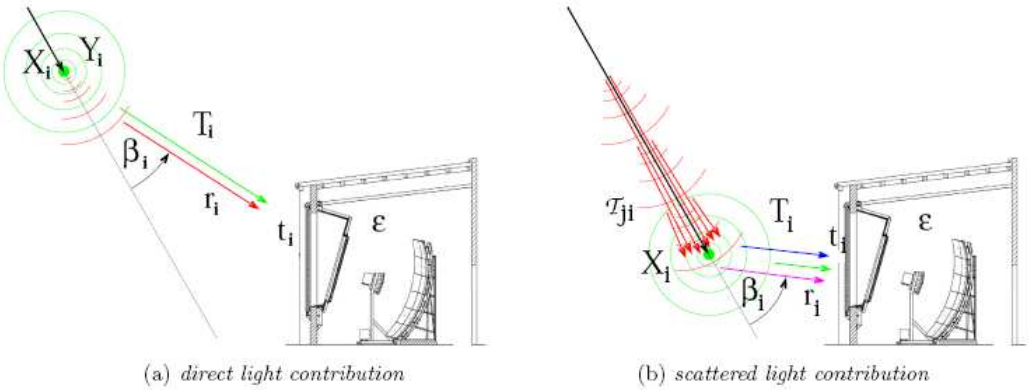


(a) *direct light contribution* (b) *scattered light contribution*

Figure 3.11: Illustration of the light flux received at the FD. Green: isotropic fluorescence light, red: forward direct Cherenkov light, blue: Rayleigh-scattered Cherenkov light, and magenta: Mie-scattered Cherenkov light.

The two major contributions to the light at the FD aperture are the fluorescence light from nitrogen molecules and Cherenkov radiation photons [96, 97, 98]. Both contributions are affected by scattering and absorption in the atmosphere. The important scattering processes are Rayleigh scattering, when photons are scattered by particles much smaller than their wavelength, and Mie scattering, from particles larger than about tenfold of the light wavelength. The amount of fluorescence light is directly proportional to the energy deposited by the air shower along its path in the atmosphere.

Given the fluorescence yield $Y_i^f$ [99, 100, 101] at a point in the atmosphere, the number of photons produced by the shower is

$$N_\gamma^f(X_i) = Y_i^f \frac{dE}{dX_i} \tag{3.27}$$

where $dE/dX_i$ denotes the energy deposited at slant depth $X_i$ .

Due to Rayleigh and Mie attenuation only a fraction of the photons, $T_i$ , can be detected at the aperture, as sketched in Fig. 3.11. The direct fluorescence light emitted at this slant depth is measured at the detector at time $t_i$ . Given the light detection efficiency of $\epsilon$ and aperture A, the fluorescence light flux $y_i^f$ measured at the FD is:

$$y_i^f = \frac{A\epsilon T_i}{4\pi r_i^2} Y_i^f \frac{dE}{dX_i}. \tag{3.28}$$

The number of photons emitted through Cherenkov radiation is proportional to the number of charged particles above a certain energy cutoff, which is in

a good approximation just the number of electrons and positrons:

$$N_\gamma^C\left(X_i\right) = Y_i^C N_e\left(X_i\right). \tag{3.29}$$

The threshold energy with the height is included in the Cherenkov yield $Y_i^C$ [102, 103]. Given the fraction $f_C\left(\beta_i\right)$ of photons emitted at an angle $\beta_i$ with respect to the shower axis, the light flux at the FD aperture originated from direct Cherenkov light is:

$$y_i^{Cd} = \frac{A\epsilon T_i}{4\pi r_i^2} f_C\left(\beta_i\right) Y_i^C N_e\left(X_i\right). \tag{3.30}$$

Although the Cherenkov photons are emitted in a narrow cone along the particle direction, they cover a considerable angular range with respect to the shower axis, because the charged particles are deviated from the primary particle direction due to multiple scattering. Due to the forward peaked nature of the Cherenkov light production, an intense Cherenkov light beam can build up along the shower as it traverses the atmosphere (Fig. 3.11 (b)). If a fraction $f_s\left(\beta_i\right)$ of the beam is scattered towards the detector it can contribute significantly to the total light received. In a simple one-dimensional model the number of photons in the beam at depth $X_i$ is just the sum of Cherenkov light produced at all previous depths $X_j$ attenuated on the way from $X_j$ to $X_i$ by $T_{ji}$:

$$N_\gamma^{beam}\left(X_i\right) = \sum_{j=0}^{i} T_{ji} Y_j^C N_e\left(X_j\right). \tag{3.31}$$

The total light received at the detector at the time $t_i$ is obtained by adding the scattered and direct light contributions:

$$y_i = y_i^{C_s} + y_i^{C_d} + y_i^f. \tag{3.32}$$

To obtain the shower energy from the light at the aperture the energy deposited in the atmosphere has to be determined. The total energy deposit is just the sum of the energy loss of electrons in the atmosphere, $dE/dX_i$ , which is related to the number of electrons $N_e\left(X_i\right)$ by:

$$\frac{dE}{dX_i} = N_e\left(X_i\right) \int_0^\infty f_e\left(E, X_i\right) \frac{dE}{dX_e\left(E, X_i\right)} dE, \tag{3.33}$$

where $f_e\left(E, X_i\right)$ denotes the normalized electron energy distribution and $\frac{dE}{dX_e(E,X_i)}$ is the energy loss of a single electron with energy $E$. The electron energy spectrum $f_e\left(E, X_i\right)$ is universal in shower age [102, 103], i.e. it does

not depend on the primary mass or energy and since the electron energy loss depends only weakly on the local density, Eq. 3.33 is simplified to:

$$\frac{dE}{dX_i} = N_e\left(X_i\right)\alpha_i, \tag{3.34}$$

where $\alpha_i$ is the average energy deposit per electron at shower age $s_i = 3/\left(1 + 2X_{max}/X_i\right)$, where $X_{max}$ denotes the shower maximum. It is parameterized from simulations as given in [103].

In general the FD will not be able to observe the full profile because of its limited field of view. Since for the calculation of the Cherenkov beam and the shower energy the full profile is required, the extrapolation to depths outside the field of view is done with a Gaisser-Hillas function which gives a good description of existing fluorescence data [93]:

$$f_{GH}\left(X\right) = \frac{dE}{X_{max}}\left(\frac{X - X_0}{X_{max} - X_0}\right)^{\frac{X-X_0}{\lambda}} e^{\frac{X_{max}-X}{\lambda}}, \tag{3.35}$$

where $X_{max}$ is the depth where the shower reaches its maximum energy deposit $dE/dX_{max}$.

The electromagnetic energy is given by the integral over the energy deposit profile:

$$E_{em} = \int_0^\infty f_{GH}\left(X\right) dX. \tag{3.36}$$

Not all of the energy of a primary cosmic ray particle ends up in the electromagnetic part of an air shower. Neutrinos escape undetected and muons need long path lengths to release their energy. This is usually accounted for by multiplying the electromagnetic energy (3.36) by a correction factor $f_{inv}$ determined from shower simulations to obtain the total primary energy:

$$E_{tot} = f_{inv} E_{em}, \tag{3.37}$$

Due to the energy dependence of the meson decay probabilities in the atmosphere, and thus the neutrino and muon production probabilities, the correction depends on the energy [104] how is shown in figure 3.12 for different hadronic interaction model, and is also subject to shower-to-shower fluctuations [105].

The statistical uncertainties of the total energy is obtained by the uncertainties of $dE/dX_{max}$ , $X_{max}$ , $X_0$ and obtained after the fit of the profile with Eq. (3.35), reflect only the statistical uncertainty of the light flux, $\sigma_{flux}\left(E_{em}\right)$. Additional uncertainties arise from the uncertainties on the core location and shower direction ($\sigma_{geo}$ ) and the correction of invisible energy ($\sigma_{inv}$).

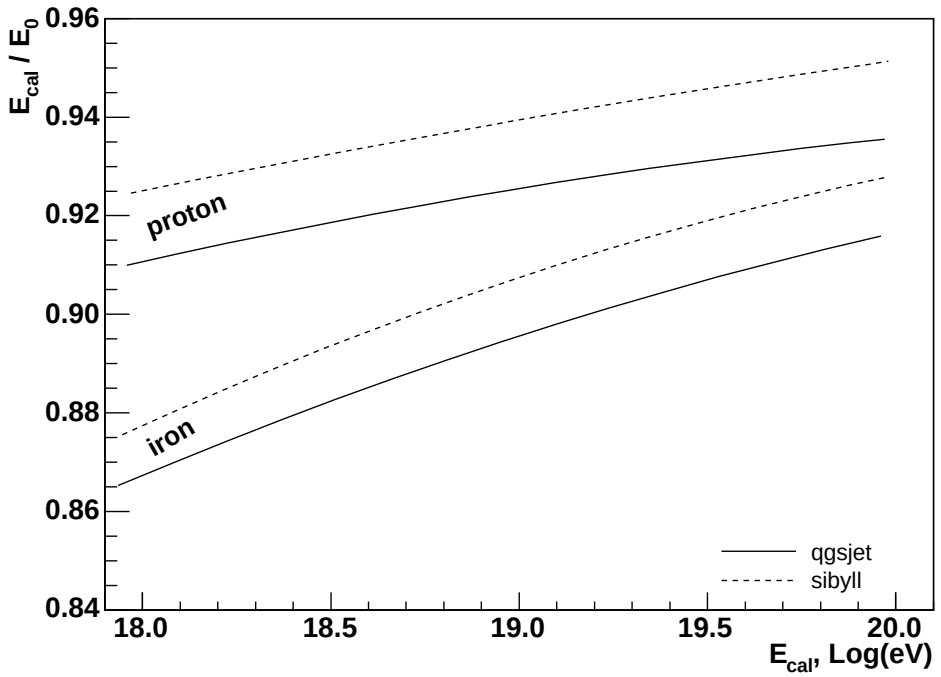


Figure 3.12: Missing energy correction plotted as the fraction $E_{cal}/E_0$ as a function of $E_{cal}$. The calorimetric energy measured $E_{cal}$ and the primary energy $E_0$ corresponde in the text to $E_{em}$ and $E_{tot}$ respectively. The variation with the high energy hadronic interaction model is shown. Simulations for proton and iron primaries, at $45^o$ [104].

The statistical variance of the total energy is:

$$\sigma_{stat}\left(E_{tot}\right)^2 = E_{tot}^2\sigma\left(f_{inv}\right)^2 + \left(\frac{df_{inv}}{E_{em}}E_{em} + f_{inv}\right)^2 \left(\sigma_{geom}\left(E_{em}\right)^2 + \sigma_{flux}\left(E_{em}\right)^2\right). \tag{3.38}$$

In [91] was shown that the energy resolution from simulated data is of about 8%.

In Figure 3.13 an example of event fitted using Eq. 3.35 is shown with fit results.

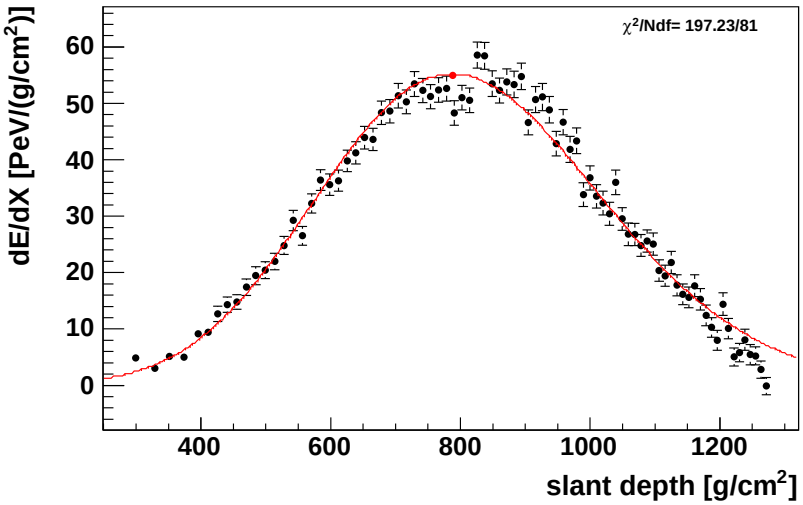


**Run 1574 Event 7**
**time stamp: 843697001 s 262517945 ns**
**Trigger: 'Physics − Int or L/R trigger', 'Shower Candidate'**
**hottest hybrid station: 302 (TOT), $\Delta$SP = 223 m**
**Mie attenuation: average**
**in Los Leones mirror 2 ( in DAQ: 2 4 6 )**

**E = (3.26 $\pm$ 0.07) $\times$ $10^{19}$ eV**
**Xmax = 788 $\pm$ 7 g/cm$^2$**
**dEdXmax = 54.99 $\pm$ 0.79 PeV/(g/cm$^2$)**
**($\lambda$,X0) = (30$\pm$3,−803$\pm$173) g/cm$^2$**
**Cherenkov−fraction = 25%**

**($\theta$,$\phi$)=(49.5$\pm$0.3, 47.8$\pm$0.4) deg**
**(x,y)=(30.00$\pm$0.07, 13.35$\pm$0.03) km**
**dca to Eye=8.73 $\pm$ 0.02 km**

Figure 3.13: Left Panel: Energy deposit profile for an FD event. The red line is the fit function. The fit results and event information are also given.

# Chapter 4

# A new Longitudinal profile reconstruction

In this chapter a new longitudinal profile reconstruction method for the Auger Fluorescence Detector (FD) events, developed in the Auger's gruop of this university, is shown.

In this method, called SG (Spot Group), the shower profile is determined through the comparison of the measured and the expected photomultiplier signals. The expected signal is estimated using a model for the light distribution on the telescope focal surface that allows to account for the camera inhomogeneities due to the presence of the Winston cones.

The light distribution on the camera, the spot, is modeled including both the effects induced by the lateral distribution of the shower particles and those due to the imaging characteristics of the telescope.

A detailed comparison of this method and the one used up to now to analyze the FD events (KG method) is presented.

The method is based on a model for the light distribution at the telescope focal surface, the spot. The spherical aberration of the telescope optics produces a spot shape which depends on the position of the spot on the camera. From the known spot shape, the fraction of signal expected in a pixel close to the spot center can be calculated, and compared to the measured ADC counts.

The typical features of this mehtos are a precise positioning of the image on the camera (thus implying good shower geometry reconstruction) and a realistic spot model. The signal fractions calculated with this spot model allows to:

- Avoid the global angular distance cut based on signal to noise used when the light profile is reconstructed (section 3).

- Define the $\chi^2$ function in terms of the measured ADC counts. Fitting untreated data allows a better control of the bias and the errors in the fit.

- Treat correctly the edges of the camera. When the image is entering or leaving the mirror field of view, only a fraction of the spot falls on the camera surface. This method gives a precise estimate of the expected signal at both ends of the profile. In case the image is crossing the overlapping field of view region between neighbouring telescopes, the signal to noise ratio is increased using data from both cameras.

- Correct for the light losses in the Winston cones of the camera. The presence of the mercedes is modeled and taken into account during the reconstruction.

In the first section of this chapter, an introduction to the spot model, to the optical spot and to the camera inhomogeneities treatment, is given.

In the second section the expected photomultiplier signal calculation is shown and in the following section the shower profile fit using this expected signal is discussed.

In the fourth section a detailed description of shower image including all the lateral shower width used in thi method, is given.

In the last section a comparison on the main shower features between our shower profile reconstruction method (SG) and the standard method (KG) are shown.

## 4.1 Spot Model

Even in the approximation of a point-like source, the spherical aberration of the telescope optics causes some spread in the photons at the focal surface. Photons arriving at the detector from a given direction in the sky are not focused in a point, but form an image on the focal surface of typical dimension of 0.5°.

The finite transversal dimension of the shower must be taken into account. In this case, the photons reaching the detector at the same time originate from different shower development stages [106]. The spot on the camera surface will then depend on the details of the lateral distribution of the shower particles. A typical Molière radius of 100 m corresponds to an angular image size of 0.6° at 10 km and 1.1° at 5 km, to be compared with the 0.5° optical spot size. It is clear that the shower transverse dimension plays an important role in the analysis only for showers close to the detector.

In the following the details of the spot due to the detector optics and the finite shower image will be described.

This spot model is neither else that a function $g_{spot}$ describing the distribution of the photon arrival directions at the FD camera focal surface.

$g_{spot}$ is obtained convolving the physical widths of the photons at diaphragm with detector effects.

$g^{p}_{spot}(\Omega; t, \theta_{GH})$ is different for different kinds of photons ($p$ = fluorescence, direct Cherenkov, scattered Cherenkov and multiple scattering) and of course it depends on the *Gaisser–Hillas* parameters $\theta_{GH}$ (eq. 3.18). Moreover $g_{spot}$ is calculated every time slot to account for the different geometrical and atmospheric conditions.

The angles $\Omega = (\alpha, \phi)$ are the polar coordinates defining a position on the camera focal surface. $\alpha$ is the angular distance from the image center, i.e. the radial coordinate while $\phi$ allows to describe a circle ($0 < \phi < 2\pi$) around to the image center (for $\alpha$ fixed). When $\alpha$ is calculated in the pixel center, $\alpha$ is replaced with the symbol $\zeta$.

The function $g_{spot}$ allows to calculated the photomultiplier FADC traces. The expected signal is compared with the data and a $\chi^2$ minimization allows to obtain the best estimation of the Gaisser-Hillas parameters.

### 4.1.1 The optical spot

The fraction of light produced by a point source and detected by a photomultiplier is calculated with a Monte Carlo simulation of the spot produced on the camera surface. The spot is obtained using a complete simulation of the optics of the telescope, including the corrector ring and the camera shadow. A series of photons, uniformly distributed across the aperture, in the direction defined by the point source, are followed using a ray tracing technique.

The simulated spot is different for different angles of incidence. This is due to the relative positions of the camera shadow and to the corrector ring optics. To speed up the calculation of the signal fractions, the spot corresponding to each photomultiplier has been tabulated and the spot for the photomultiplier with the closest direction to the one defined by the shower geometry is used in the reconstruction.

Figure 4.1 illustrates the Monte Carlo method used to calculate the fraction of the signal detected by each pixel. At time t, the spot center is placed at the point where the signal is expected. This point lies in the intersection line of the SDP with the camera and is fixed by the geometrical reconstruction. The number of light rays falling into each pixel surface, normalized to the total number of light rays, gives the fraction $f_{pmt}(t)$ of the signal expected

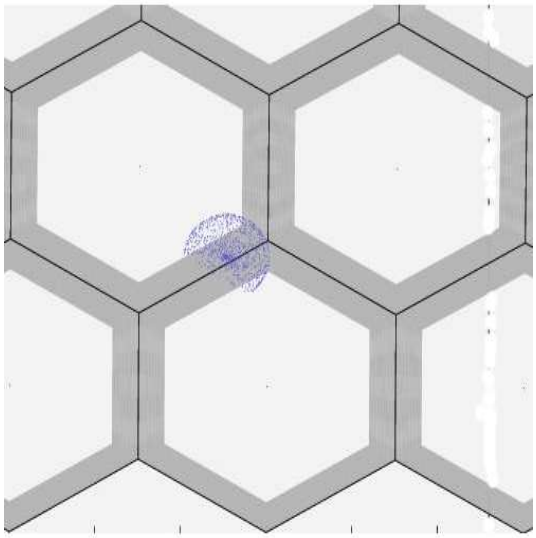

Figure 4.1: Sketch of the method used to calculate the signal fractions in pixels. The positions of the pixel centers and the pixel angular dimensions are known. The shower geometry fixes the position of the spot center and the spot model gives the displacements of the spot points with respect to the center (the blu points). The pixel signal fraction is obtained summing the number of spot points within each pixel and normalizing the sum to the total number of points. The grey region between the parallel lines is covered by the mercedes.

in each photomultiplier *pmt*. In general for a given time $t$ the fractions add up to 1, $\sum_{pmt} f_{ptm} = 1$. When the shower enters or leaves the telescope field of view, $\sum_{pmt} f_{ptm} < 1$ because a number of light rays do not hit the camera.

If the spot model is not consistent with the real image spot it is easy to introduce a bias in the reconstruction procedure. The spot model used here is based on the optical characteristics of the telescope. As we will see, this leads to problems for close high-energy showers where the dimensions of the shower image can not be neglected.

### 4.1.2 Mercedes Correction

The camera inhomogeneities due to the presence of the Winston cones are properly taken into account by the spot method. The light falling onto the mercedes surface is reflected towards the photomultiplier cathode, with some inefficiency mainly due to the mylar reflection.

The Monte Carlo method used to calculate the spot fractions can be extended to take into account the mercedes. At any given time $t$, we can calculate the fraction $\delta_{pmt}$ of spot light rays given by the ratio of light rays

hitting the mercedes surface of a given *pmt* to the total number of light rays hitting the pixel (figure 4.1). $\delta_{pmt}$ will also depend on $X_{max}$, due to the finite transverse dimension of the showers: $\delta_{pmt}(t, X_{max})$. By definition $0 \leq \delta_{pmt} \leq 1$; $\delta_{pmt} = 0$ when all the light falls on the pixel photocathode without reflections on the mercedes and $\delta_{pmt} = 1$ when all the light is reflected on the mercedes before reaching the photocathode.

For a given *pmt*, the fraction of spot light rays that reach the photocatode surface is given by:

$$\epsilon_M^{pmt}(t, X_{max}) = t_M \ \delta_{pmt}(t, X_{max}) + (1 - \delta_{pmt}(t, X_{max})) \ , \tag{4.1}$$

where $t_M$ is the mercedes reflection efficiency. $\epsilon_M^{pmt}$ is equal to 1 only if all the light rays reach the photocatode without mercedes reflection ($\delta_{pmt} = 0$) or in the ideal case of perfect mercedes reflection efficiency ($t_M = 1$). The mercedes reflection efficiency has been measured in laboratory [59] to be $t_M = 0.80$.

In order to apply the mercedes correction to our profile reconstruction we have to take into account that the calibration constants of each pixel are determined with the drum in a condition of uniform illumination of the camera. Namely, the ratio of light rays hitting the mercedes and the photocatode is the same for all camera pixels, and it is simply given by the ratio of the mercedes to photocatode area (see figure 4.1). In this case $\delta_D = 0.632$ for all pixels and $\epsilon_D = 0.874$ for $t_M = 0.8$.

In order to take into account the camera inhomogeneities due to the Wiston cones, we calculate a correction factor:

$$f'_{pmt}(t, X_{max}) = \frac{\epsilon_M^{pmt}(t, X_{max})}{\epsilon_D} = \frac{t_M \ \delta_{pmt}(t, X_{max}) + (1 - \delta_{pmt}(t, X_{max}))}{t_M \ \delta_D + (1 - \delta_D)} \tag{4.2}$$

The correction ranges from $f'_{pmt} \simeq 1.08$ for $\delta_{pmt} = 0$ to $f'_{pmt} \simeq 0.87$ for $\delta_{pmt} = 1$ with $t_M = 0.80$. Thus, depending on the position of the spot, the PMT signal can be from 8% higher to 13% lower than previously expected. The global effect on the profile fit is averaged along the whole track, so it is expected to be small.

## 4.2 Pixel selection and expected pixel signal

Knowing $g_{spot}$ the calculation of the expected pixel signal is straightforward: $g_{spot}$ (normalized to 1) is integrated over the photomultiplier field of view $\Omega_{pmt}$ to obtain the fraction $f''_{pmt}$ of photon flux detected by this pixel:

$$f''^{p}_{pmt}(t; \theta_{GH}) \ = \ \int_{\Omega_{pmt}} d\Omega \ g^p_{spot}(\Omega; t, \theta_{GH}) \tag{4.3}$$

where $d\Omega = d\alpha\alpha\, d\phi$. The integration is done separately in the focal surface covered and not covered by mercedes. This allows to account for the mercedes reflection efficiency (section 3.2 of [107]) and then the correct application of the drum calibration constants * .

In the following text, we call $f$ the final fraction which accounts also for the mercedes:

$$f^p_{pmt}(t;\theta_{GH}) = f' \times f'' = f' \times \int_{\Omega_{pmt}} d\Omega\; g^p_{spot}(\Omega;t,\theta_{GH}) \tag{4.4}$$

The fraction $f_{pmt}$ is calculated numerically. We simulate photons directions following the $g^p_{spot}$ distribution and then we calculate the number of photons detected by the pixel. The probability that a pixel is fired, i.e. $f_{pmt}$, is the ratio between the number of the detected photons to the total number of simulated photons.

The probability $f_{pmt}$ allows the calculation of the expected ADC signal of a pmt:

$$\widehat{n}^{pmt}_{adc}(t;\theta_{GH}) = \sum_p \frac{f^p_{pmt}(t;\theta_{GH})}{C^{370}_{pmt}}\; \widehat{n}^{370}_{\gamma;p}(t;\theta_{GH}) \;+\; n^{pmt}_{ped} \tag{4.5}$$

where $C^{370}_{pmt}$ is the calibration constant of the photomultiplier, $n^{pmt}_{ped}$ is the FADC pedestal and $\widehat{n}^{370}_{\gamma;p}$ is the expected photon flux at the diaphragm.

The expected signal is calculated only for some pixels. First we define a time-start and time-stop for the track taking the minimum time-start and the maximum time-stop of the photomultipliers pulses. In this search only photomultipliers for which the Offline finding pulse algorithm has found a pulse are used. Moreover, to avoid pixels for which the uncertainty on the pulse could be large, the search is done only for T2 pixels having $\zeta < 2°$. At this point we make a loop on time (bins of 100 ns) between time-start and time-stop. Using the time-fit relation, we associate to each time bin a position on the camera focal surface along the shower detector plane. At each time only pixels with $\zeta < \zeta_c$ are selected. $\zeta_c$ is a constant value that could be defined by the user. It's optimal value depends on the fit strategy used to fit the shower observables (see next section). In general $\zeta_c$ is the compromise between the requirement to contain as much as possible the measured shower image and to avoid an exaggerate increase of the background light.

*The drum illuminates the camera in a uniform way while the shower image depends on $g_{spot}$ which is not uniform.

### 4.2.1 Shower width

There are several physical effects determining the shower image $g_{spot}$ detected by FD telescopes. First of all the angular distribution of the fluorescence photons is a direct consequence of the finite shower transversal size. This distribution has been parametrized in [106] with an universal function. This function is used to correct the shower energy in the official Auger profile reconstruction (KG) [91]. The scattered Cherenkov light also influences the shower image and its angular distribution at the FD diaphragm, wider than the fluorescence one, has been modeled in [108]. The calculation of the Cherenkov width proposed in [108] has been implemented in the KG reconstruction [109]. Another contribution to the photon angular distribution is due to the multiple scattering light. This effect has been calculated by different authors [110, 111, 112], tested on laser shots [113] and implemented in the KG profile reconstruction.

## 4.3 Shower profile fit

In this section we describe the longitudinal profile fit technique. In order to make more fluent the discussion we define firstly the fit strategies, showing the mathematical expression of the $\chi^2$ functions. After we will discust the features of the "spot" longitudinal profile fit.

### 4.3.1 Fit strategies

In the "spot" profile reconstruction we define two fit strategies. The determination of the best estimators of the Gaisser-Hillas parameters could be done by making a fit of the FADC traces ($ADC - Fit$) or a fit of the *measured* photon flux at diaphragm (*Ph-Fit*).

In the $ADC - Fit$ the $\chi^2$ function is calculated in the following way:

$$\chi^2_{ADC}(\theta_{GH}) = \sum_t \sum_{pmt} \left( \frac{n^{pmt}_{adc}(t) - \widehat{n}^{pmt}_{adc}(t;\theta_{GH})}{\widehat{\sigma}^{pmt}_{adc}(t;\theta_{GH})} \right)^2 \tag{4.6}$$

where $\widehat{n}^{pmt}_{adc}$ are the expected FADC traces (eq. 4.5), $n^{pmt}_{adc}$ are the measured traces and the sum is restricted to the time window and selected pixels defined in section 4.2. The errors on the signal are calculated using the expected signal [†] and for that reason they are functions of the Gaisser-Hillas parameters.

[†]The notation $\widehat{a}$ is used for the expected quantities. The same observables calculated from the data is represented with $a$

In the $Ph - Fit$ we must calculate the *measured* flux from the ADC traces. The flux obtained from the data is defined in the following way:

$$n^{370}_{\gamma;M}(t) = \sum_{pmt} C^{370}_{pmt}(n^{pmt}_{adc}(t) - n^{pmt}_{ped}) \tag{4.7}$$

$n^{370}_{\gamma;M}$ is the is the photon flux at diaphragm corrected for the spot fractions. As in the $ADC - Fit$, the sum is restricted to the only selected pixels ($\zeta < \zeta_c$) and the flux is calculated in the time window defined in section 4.2. We call $n^{370}_{\gamma;M}(t)$ *measured* flux because it is not exactly the photon flux at diaphragm, but the flux at diaphragm convoluted with detector effects and restricted to field of view defined by $\zeta_c$.

The expectation for $n^{370}_{\gamma;M}$ is calculated defining, at a given time and for a given process, the total fraction

$$f^p_{tot}(t;\theta_{GH}) \;=\; \sum_{pmt} f^p_{pmt}(t;\theta_{GH}) \tag{4.8}$$

which is the fraction of flux at diaphragm $\widehat{n}^{370}_{\gamma;p}$ detected by the telescope. The expected photon flux is then

$$\widehat{n}^{370}_{\gamma;M}(t;\theta_{GH}) \;=\; \sum_{p} \widehat{n}^{370}_{\gamma;p}(t;\theta_{GH}) f^p_{tot}(t;\theta_{GH}) \tag{4.9}$$

and the $\chi^2$ function of the *Ph-Fit* is:

$$\chi^2_{Ph}(\theta_{GH}) = \sum_t \left( \frac{n^{370}_{\gamma;M}(t) - \widehat{n}^{370}_{\gamma;M}(t;\theta_{GH})}{\widehat{\sigma}_{\gamma;M}(t;\theta_{GH})} \right)^2 \tag{4.10}$$

The the errors $\widehat{\sigma}_{\gamma;M}$ of the *measured* photon flux are obtained propagating the errors of the FADC traces.

### 4.3.2 Considerations on shower profile fit

The main advantage of the "spot" reconstruction method in comparison to KG one is the possibility to calculate the expected FADC traces. The calculation is done using a detailed model of the angular distribution of the light at the focal camera surface. In this way both the longitudinal and lateral light profiles are calculated taking into account detector related effects.

We expect tht the light from the shower is mainly concentrated close to the image center, so a wide angular window $\zeta_c$ in the pixel selection would lower significantly the overall signal to noise ratio. This is not a problem for

the $ADC - Fit$ which is nearly independent of the huge background introduced by the pixels at large values of $\zeta$. In fact, due to the small signal to noise ratio, the $\chi^2$ contribution of these pixels is nearly independent of the Gaisser-Hillas parameters and thus they do not affect significantly the minimization. This feature of the $ADC - Fit$ allows to collect almost all detected light ($\zeta_c \sim 4°$) without lowering the performance of fit.

In the case of the $Ph - Fit$ it would be better to make a pixel selection which excludes photomultipliers with very low signals (i.e. $\zeta_c \sim \zeta_{opt}$). In fact in this case the unbinned information of the FADC traces is lost and the pixels with low signal to noise ratio will worsen the fit, increasing the statistical uncertainties on the fitted shower parameters. This does not happen in the $ADC - Fit$, because, as noted before, it is insensitive to the pixels dominated by background, so that the statistical uncertainty on the shower parameters will be independent of the particular choice of $\zeta_c$.

When a significant amount of light is outside of the field of view defined by $\zeta_c$ a correction for the not collected light is automatically included in the fractions defined by eq. (4.12). This can be understood if we remember the definition $of f^p_{pmt}$: they are the fractions of the photon flux at the diaphragm detected by the photomultipliers. Hence if pixels with $\zeta > \zeta_c$ have a probability detecting some signal, the total fraction of equation (4.8) will be less than 1. $1 - f^p_{tot}$ will be the fraction of not collected light.

The corrections for the not collected light in the "spot" reconstruction method properly account for detector effects, like telescope spherical aberration and finite pixel dimension. This does not happen in the KG reconstruction because the corrections are calculated using the theoretical parameterizations of the angular distribution of the light at the telescope diaphragm. In comparison to the Auger official reconstruction the $ADC - Fit$ has also the significative advantage of making possible the simultaneous fit of the lateral and longitudinal profiles.

The philosophy of the "spot" reconstruction is to make a fit of the observables leaving unchanged as much as possible the data. It is clear that the $ADC - Fit$ entirely honors this philosophy. Moreover it is for this reason that in the *Ph-Fit* strategy we make a fit of the measured photon flux which includes detector effects. With an easy modification of the software, an equivalent fit of the photon flux at the diaphragm without detector effects or a fit of the energy deposit like in the KG reconstruction could be introduced. The fit results will not differ from the *Ph-Fit* ones.

### 4.3.3 Results of the "spot" reconstruction

The most natural way to visualize the output of the "spot" reconstruction is to plot the measured and expected FADC traces. Figure 4.2 compares the measured and expected FADC traces for few pixels along the SDP of the event with SD identification number $SdId = 1677996$.

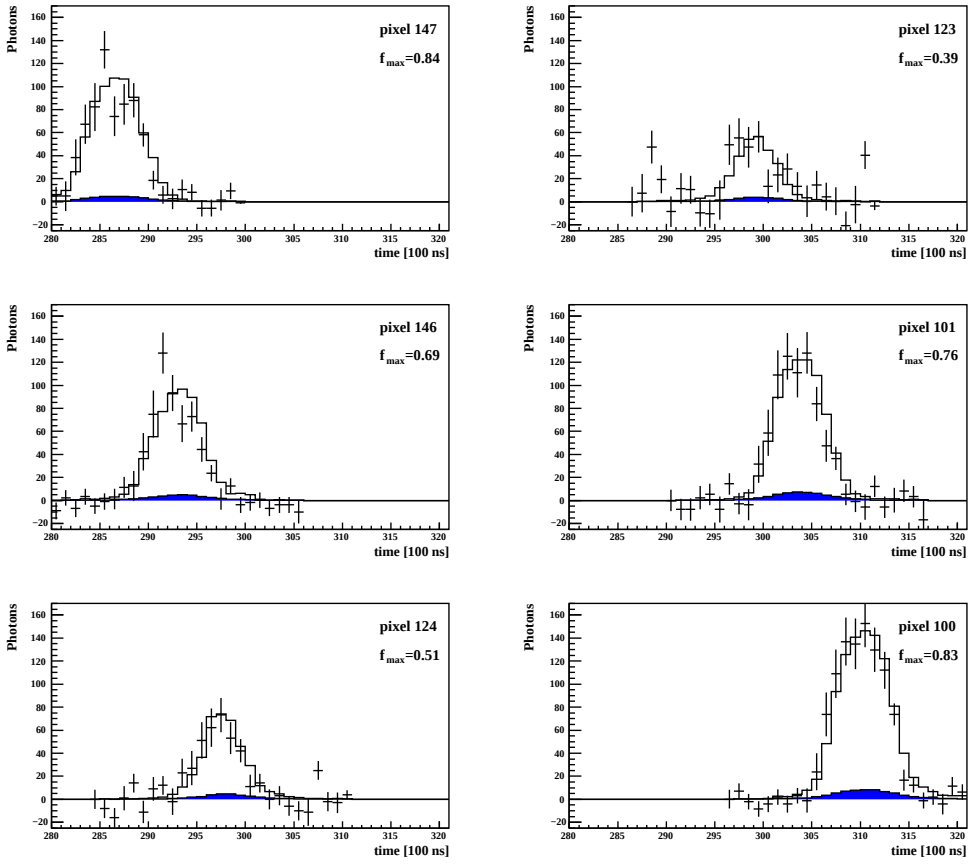


Figure 4.2: Number of detected photons as a function of the time (FADC traces corrected by the drum calibration constants) for few pixels of event $SdId = 1677996$. The dots are the data, the solid black line is the total expected signal and the blue distribution shows the no-fluorescence light (mainly scattered Cherenkov). $f_{max}$ is the expected fraction of total light detected by the pixel at the time corresponding to the maximum signal.

The traces are expressed in terms of photons at diaphragm. For each pulse the expected fraction of total light (i.e. fluorescence+Cherenkov) detected by the pixel at the time corresponding to the maximum signal is shown. As one can see for pixels 123 and 124 the fractions are relatively low, at the level

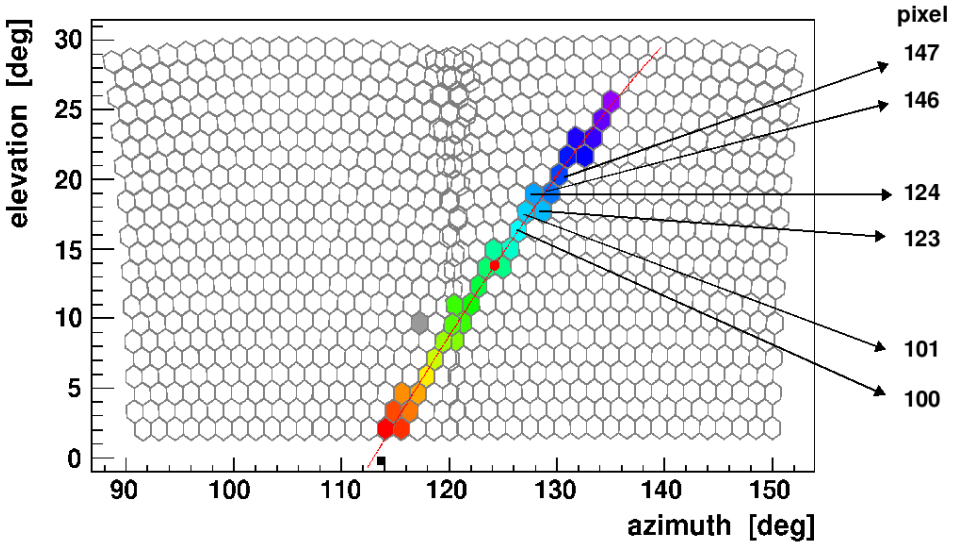


Figure 4.3: The pixels shown in figure 4.2 are indicated on this camera display.

of $40\% - 50\%$. In fact the SDP track is crossing the border of those pixels so our spot model predict that the signal is equally shared among them. For the other pixels the fractions are larger, but never greater than 80% because the shower image is never fully contained in only one pixel. Notice that the good agreement between the data and the expectation is due not only to a realistic spot model, but also to a precise geometry reconstruction. In fact, shifting slightly the SDP track we do not observe an equal signal (or fraction) in pixels 123 and 124. For example, if the SDP track is moved within the pixel 123 field of view, in this pixel the signal will be significantly larger than the signal of the other pixel.

When making the analysis of many showers, the visualization of all photomultipliers signals is unpractical. A summary plot of the results of the reconstruction should show how well the shower longitudinal profile and the shower width are fitted. Figure 4.4 on the left shows the number of photons detected along the full shower track as a function of $\zeta$ and on the right the *measured* photon flux defined by equation (4.7). In this way the shower width is shown integrating over the shower time development, while the shower longitudinal profile integrating over $\zeta$. Notice that both distributions of the expected number of photons show a non-smooth behaviour due to detector effects. For example the pick in the right distribution is made by photons

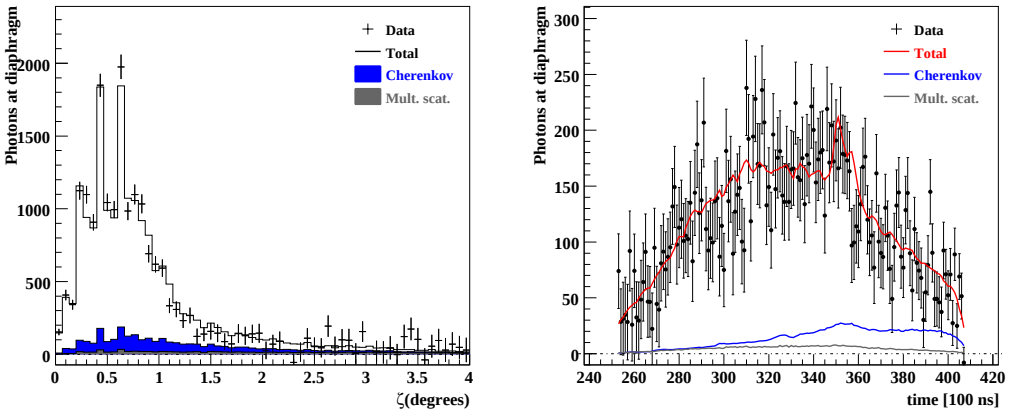


Figure 4.4: Number of detected photons as a function of $\zeta$ (on the left) and as a function of the time (on the right). The data and the expectations for different kind of photons are shown.

detected in the region of overlap of the two FD mirrors field of view. Notice that this light is not selected by the KG reconstruction producing holes in the longitudinal profile plots.

Another important plot is of course that of the energy deposit as a function of the atmospheric depth. The energy deposit of the data is calculated subtracting to the ADC data the contribution from the background light ($bkg$ means Cherenkov and multiple scattering) and correcting for the detector effects (fraction $f^{flu}_{pmt}$ for the fluorescence light):

$$n^{370}_{\gamma;fluo}(t;\theta_{GH}) = \sum_{pmt} \frac{C^{370}_{pmt}}{f^{flu}_{pmt}(t;\theta_{GH})} \times \times \left( n^{pmt}_{adc}(t) - n^{pmt}_{ped} - \sum_{p}^{\{bkg\}} \frac{f^{p}_{pmt}(t;\theta_{GH})}{C^{370}_{pmt}} \, \widehat{n}^{370}_{\gamma;p}(t;\theta_{GH}) \right) \tag{4.11}$$

At this point the calculation of the energy deposit $dE/dX$ from the fluorescence light $n^{370}_{\gamma;fluo}$ estimated from the data is done in the standard way correcting for the atmospheric and geometrical effects and using the fluorescence yield [114]. Notice that the energy deposit of the data depends on the Gaisser-Hillas parameters $\theta_{GH}$, becouse the background light and the fractions depend on these.

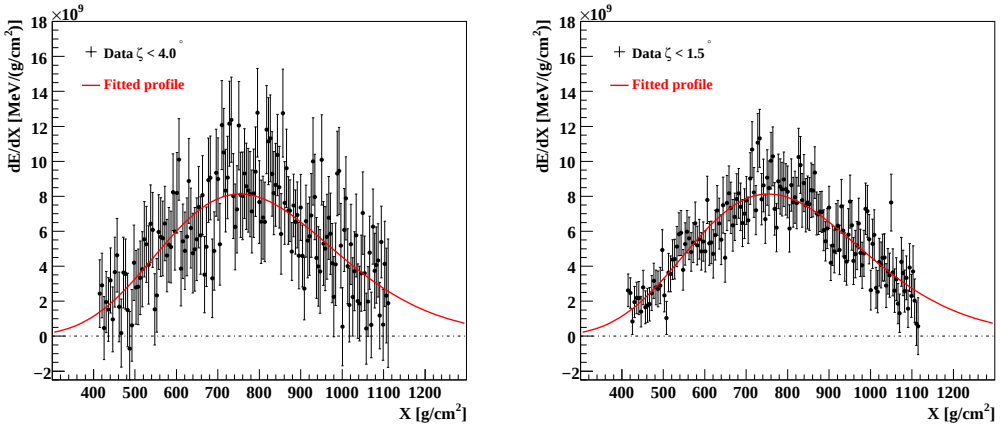


Figure 4.5: On the left: reconstructed energy deposit as a function of the atmospheric depth overimposed to the fitted Gaisser-Hillas profile. The figure on the right is a better visualization of the data because the energy deposit was calculated using only pixels close to the SDP track. The Gaisser-Hillas profile is exactly the same in both figures.

Figure 4.5 on the left show the energy deposit from the data overimposed to the fitted Gaisser-Hillas profile. Notice that, in comparison to the right plot of figure 4.4 we don't have detector effects having divided the fluorescence signal calculated from data by the fraction $f_{pmt}^{flu}$. The large uncertainties on the data points come from pixels not close to the SDP track. A better visualization of the energy deposit could be obtained selecting only pixels with $\zeta < 1.5°$ as shown in the right picture of figure 4.5. In this plot the Gaisser-Hillas profile is exactly the same of the left figure. This improved visualization becomes mandatory for far away showers with low photomultipliers signals. The same consideration is valid for the light flux plot.

The output of the "spot" reconstruction described in this section is available for both $ADC - Fit$ and $Ph - Fit$, because in both strategies we make the calculation of the fractions. However there is substantial difference: in the $ADC - Fit$ the transverse and longitudinal light profile are fitted simultaneously while the only longitudinal profile informations are used in the $Ph - Fit$.

A not realistic spot model or/and a wrong reconstructed shower geometry will affect the $ADC - Fit$ with the risk to introduce bias in the fitted Gaisser-Hillas parameters. The $Ph - Fit$ is nearly free from this risk: the only dependence on the light width is in the *a posteriori* correction that often is reasonably small, even for $\zeta \sim \zeta_{opt}$.

The values of the fitted shower energy and maximum depth of the energy

| | $E\ [EeV]$ | $X_{max}\ [g/cm^2]$ | $\chi^2/n.d.f.$ |
|---|---|---|---|
| $ADC-Fit$ | $4.94\ \pm\ 0.11$ | $764\ \pm\ 6$ | 1.05 |
| $Ph-Fit$ | $4.72\ \pm\ 0.15$ | $764\ \pm\ 19$ | 1.19 |

Table 4.1: Fitted shower parameters and $\chi^2$ at minimum divided by the number of degree of freedom for event $SdId = 1677996$.

deposit obtained in both fit strategies are shown in table 4.1. The values are in agreement among them proving a good understanding of the light width and a precise geometry reconstruction.

## 4.4 The shower image

The key quantity of the "spot" reconstruction method is the "spot function" $g^p_{spot}$ of equation (4.12) which describes the angular distribution of the light at the focal camera surface $g^p_{spot}$ is the convolution of several functions describing the angular distribution of the light at the diaphragm and the detector effects (spherical aberration, etc...). In the text we use the symbol $\otimes$ to indicate the operation of convolution

$$h\ \otimes\ f\ =\ \int dx'\ h(x-x')\ f(x')\ .$$

In the reconstruction method described in this paper the "spot function" is calculated in the following way:

$$g^p_{spot}\ =\ s\ \otimes\ u\ \otimes\ w^p \tag{4.12}$$

where $s$ is the function describing the optical spot, i.e. the circle of least confusion of the FD optics. $w^p$ is the angular distribution of the light at the FD diaphragm and it is in general different for different kind of radiations (index $p$: fluorescence, direct Cherenkov, scattered Cherenkov and light of multiple scattering). $u$ is an empirical function which must be introduced in order to reproduce the measured shower image. $u$ makes broader the product $s\ \otimes\ w^p$ and it parametrizes effects not described by the theoretical functions $s$ and $w^p$.

In the following sections the three functions of the convolution will be described in detail. In order to smooth the statistical fluctuations of the data and to average over the track positions on the camera (the $\zeta$ distribution depends by this) we studied the shower image width looking to all light produced by 300 well reconstructed golden hybrid showers.

### 4.4.1 The optical spot $s$

The FD Schmidt optics plus the corrector ring allows to keep the angular size of the optical spot $s$ at about 0.25 degrees (radius). Due to the relative positions of the camera shadow and to the corrector ring optics the optical spot depends on the incident direction of the light. The function $s$ has been tabulated for each photomultiplier and the spot for the photomultiplier with the closest direction to the one defined by the shower geometry is used in the reconstruction.

The optical spot has been calculated according to [47]. Recently a more realistic simulation of the FD optics based on Geant4 has been implemented in the Offline framework [115]. We do not have introduced this new calculation within the reconstruction chain, but following some studies done in the past, we expect that this more realistic optical spot will produce only very small changes in the shower observables.

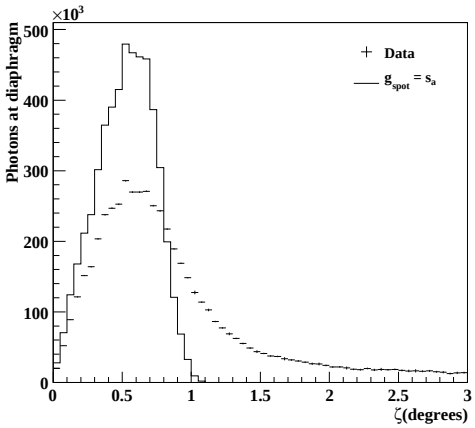


Figure 4.6: Number of detected photons as a function of $\zeta$ for 300 showers. The data are compared with the expected signal calculated assuming that the shower image is determined by the only optical spot.

Figure 4.7 shows the angular distribution of the photons produced in the 300 showers. The data and the total expectation calculated with $g^p_{spot} = s$, i.e. assuming that the source is point-like and assuming that $u$ is a $\delta$ function, are overimposed. As one can see, the only optical spot cannot describe the data. The width produced by $s$ extending up to 1° and it is significantly larger than 0.25°, the radius of the optical spot. This is a detector effect: the size of half pixel is 0.75° and if the image center is close to pixel border, some photons are detected by the adjacent photomultiplier for which $\zeta \sim 0.75°$.

A measurement of the spot light distribution for a point-like source has been reported in [109]. A significant tail of the optical spot (about 6% of the light has $\alpha > 1^\circ$) has been observed. The cumulative distribution of this halo has been parameterized with the function

$$H_{halo} \;=\; p\left[1-\exp\left(-\frac{\alpha}{\theta_1}\right)\right] \;+\; (1-p)\left[1-\exp\left(-\left(\frac{\alpha}{\theta_2}\right)^{\gamma}\right)\right] \qquad (4.13)$$

Ideally the measurement reported in [109] should allow a parameterization of a sort of an effective optical spot, including the nominal spot light produced by the spherical aberration plus residual effects due to the dust or, more in general, due to a non perfect optics (mirrors misalignment etc...). However, looking to the figure 2 of [109], the first experimental point is for $\alpha \simeq 0.7^\circ$. All the details for smaller values of $\alpha$ produced by the optics are lost. For that reason, in our reconstruction method, the use of the function $H_{halo}$ is restricted to the parameterization of the halo light only.

In order to include in the $g^p_{spot}$ calculation both the spherical aberration and the halo we define a new function $s$ in the following way:

$$s \;=\; (1-c)\; s_a \;+\; c\; s_h \qquad (4.14)$$

where $s_a$ accounts for the spherical aberration, $s_h$ is the angular differential distribution of the light in the halo and $c$ is a constant. Notice that $s_a$ and $s_h$ must be normalized to 1 to ensure the correct normalization of $s$. From the cumulative distribution $H_{halo}$ one can derive the angular distribution of the light in the halo:

$$h_{halo} \;=\; \frac{1}{2\pi\alpha}\;\frac{dH_{halo}}{d\alpha} \qquad (4.15)$$

where the $2\pi$ factor accounts for the normalization over the $\phi$ coordinate.

We do not replace $s_h$ with $h_{halo}$ because looking at figure 2 of [109], this would imply an unrealistic extrapolation of the measurements significantly below the lowest experimental point $\alpha_0 \simeq 0.7^\circ$. Instead, we decided to use $h_{halo}$ to describe only the light in the halo above $\alpha_0$ and to assume a constant behaviour below $\alpha_0$. Our final parameterization of the halo angular distribution is then:

$$s_h(\alpha) \;=\; \frac{\theta(\alpha_0-\alpha)\; h_{halo}(\alpha_0) \;+\; \theta(\alpha-\alpha_0)\; h_{halo}(\alpha)}{\pi\alpha_0^2 h_{halo}(\alpha_0) \;+\; 1 - H_{halo}(\alpha_0)} \qquad (4.16)$$

where $\theta$ is the step function[‡] and the constant in the denominator ensures the normalization to 1 of $s_h$.

[‡] $\theta(x) = 1$ for $x > 0$ and $= 0$ otherwise.

The value of the constant $c$ in equation (4.14) defines the relative normalization of the two functions $s_a$ and $s_h$. $c$ could be expressed in terms of the fraction $X$ of light for $\alpha > \alpha_0$. Noting that for these values of $\alpha$, $s_a = 0$ one has

$$X \;=\; \int_0^{2\pi} d\phi \int_{\alpha_0}^{\infty} d\alpha\alpha \; s \;=\; c \int_0^{2\pi} d\phi \int_{\alpha_0}^{\infty} d\alpha\alpha \; s_h \qquad (4.17)$$

and expressing the integral in terms of the cumulative function $H_{halo}$ we obtain the relation between $c$ and $X$

$$c \;=\; \frac{X}{1 - H_{halo}(\alpha_0)} \; \left(\pi\alpha_0^2 h_{halo}(\alpha_0) \;+\; 1 - H_{halo}(\alpha_0)\right) \qquad (4.18)$$

For example, in case we want to reproduce the same angular distribution of the light in the halo as [109] for $\alpha > \alpha_0$, we should fix $X = 1 - H_{halo}(\alpha_0) \simeq 0.106$ for which $c \simeq 14\%$.

Figure **??**, right panel, shows the angular distribution of the photons produced by the 300 showers. The data distribution is superimposed to the expected one calculated with $g^p_{spot} = s$. Now the width produced by $s$ has a long tail for $\alpha > 1^\circ$ due to the halo effect.

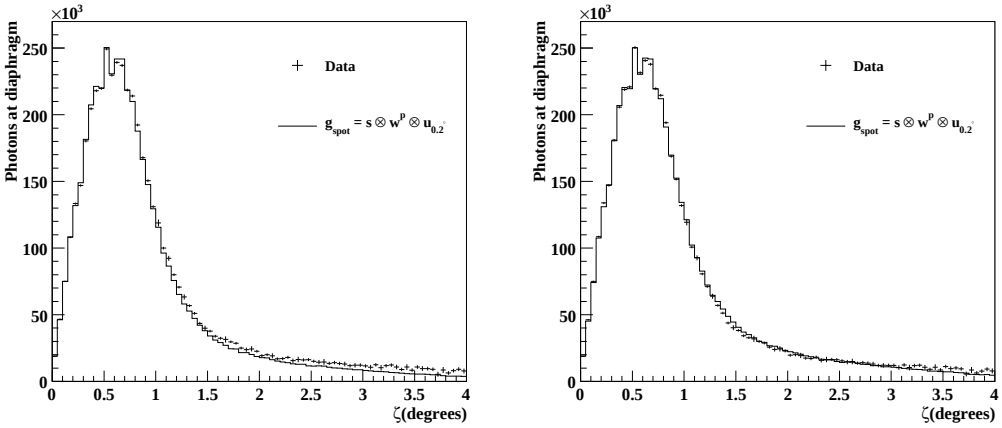


Figure 4.7: On the left: expected number of photons as a function of $\zeta$ calculated with $g^p_{spot} = s \otimes w^p \otimes u_{0.2^\circ}$ summing the light coming from the data sample of 300 showers, $s$ is fixed with $X = 1$ - $H(\alpha_0) \simeq 0.106$ ($c = 14\%$). On the right: the same distribution but $s$ fixed with $X = 0.15$ ($c = 19\%$).

In order to see how well the model for the halo describes the data, we should calculate the expected lateral width convolving all known effects: the spot function $s$, the physical widths $w^p$ and the empirical function $u$. Details

on the $w^p$ and $u$ calculations will be the object of the next two sections. For the moment, let's assume to be able to calculate $g^p_{spot} = s \otimes w^p \otimes u$ and let's compare the expected angular distribution with the measured one in our sample of 300 events. In the left panel of figure 4.7 the spot function has been calculated assuming the same halo parameterization suggested in [109], i.e. with $X = 0.106$ ($c = 14\%$). We notice that the distribution is well described around the peak while the tail above $2^\circ$ is underestimated. This suggests that the amount of light in the halo should be larger. A larger halo could easily obtained increasing X. Figure 4.7 on the right shows how a better description of the data can be obtained with $X = 0.15$ ($c = 19\%$).

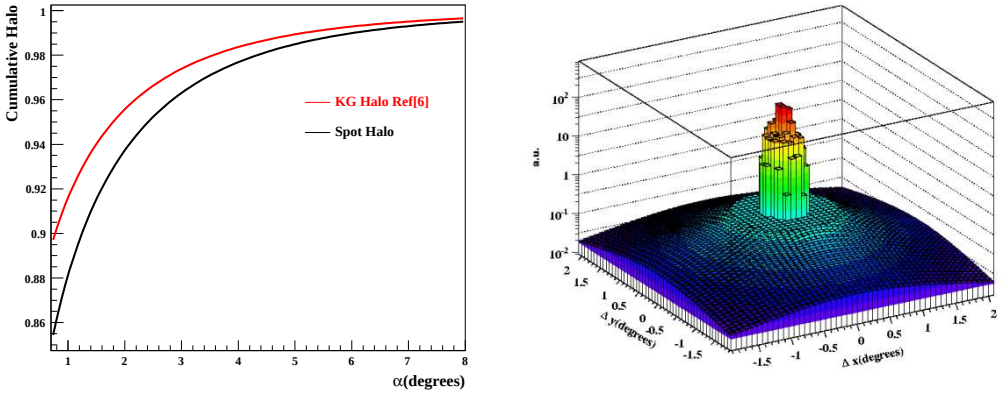


Figure 4.8: On the left: cumulative of the halo distribution for $\alpha > 0.7^\circ$. The red line is the parameterization presented in [109], while the black curve is the parameterization we find to give a better description of the data. On the right: two dimensional angular distribution of optical spot including the halo light.

The latter has the following analytical expression:

$$S_h(\alpha) \;=\; 1 \;-\; X\,\frac{1 - H(\alpha)}{1 - H(\alpha_0)} \tag{4.19}$$

where $X = 0.15$. Notice that with our parameterization, the amount of light above $1.4^\circ$ ($\simeq \zeta_{opt}$) is increased by $3\% - 4\%$. On the same figure on the right the two dimensional distribution $s$ (eq.(4.14)) of the optical spot plus the halo used in our reconstruction analysis code is shown.

### 4.4.2 The "physical width" $w^p$

The function $w^p$ is called "physical width" because it is not a consequence of detector effects, but it reflects the width of the shower. $w^p$ is different

for different kind of radiations (index $p$) and it is calculated according to theoretical predictions. $w^p(\Omega; t, \theta_{GH})$ is in general a function of the solid angle $\Omega = (\theta, \phi)$, of the time $t$ and of the Gaisser-Hillas parameters $\theta_{GH}$. It turns out that the widths of all the processes have azimuthal symmetry, i.e. $w^p$ does not depend on $\phi$, while the dependence on $\theta_{GH}$ is different for each kind of radiation.

The integration of $w^p$ is done numerically. When the cumulative function $F^p$ of the distribution in $\alpha$ has an analytical expression, the integration is done by means of the "Inverse transform method" [116]. From the relation $\alpha(F^p)$, i.e. $\alpha$ as a function of $F^p$, random values of $\alpha$ following the width distribution are obtained generating uniformly random values of $F^p$ between $[0, 1]$. Due to the azimuthal symmetry, the angle $\phi$ is uniformly generated between $[0, 2\pi]$.

Notice that the width function $w^p$ is related to $F^p$ via the following equation

$$w^p \;=\; \frac{1}{2\pi\alpha}\;\frac{dF^p}{d\alpha} \tag{4.20}$$

where the $2\pi$ factor accounts for the normalization over the $\phi$ coordinate.

The width of the fluorescence radiation has been parametrized using simulated showers by an universal (i.e. not dependent on the primary mass) analytical function [**?**]. In this paper the cumulative distribution of $r^\star$, the shower plane distance ($r$) in units of Moliere radius ($r_M$), is

$$F^{flu}(r^\star; s) \;=\; 1 \;-\; (1 \;+\; a(s)\; r^\star)^{-b(s)} \tag{4.21}$$

where $s$ is the shower age. The angle $\alpha$ is calculated knowing the FD-shower axis distance $d$ (calculated in each time slot along the SDP plane)

$$r^\star \;=\; \frac{d\;\tan\alpha}{r_M} \tag{4.22}$$

The relation $\alpha(F^{flu})$ is obtained from equations (4.21) and (4.22)

$$\alpha \;=\; \frac{r_M}{d}\;\arctan\left\{\frac{1}{a}\left[\left(1 - F^{flu}\right)^{-1/b} \;-\; 1\right]\right\} \tag{4.23}$$

The width of the direct Cherenkov radiation is not necessarily equal to the one of the fluorescence light. In fact, unlike for the fluorescence radiation, only electrons above an energy threshold which depends on the atmospheric altitude emit Cherenkov photons. Due to the lack of a theoretical parameterization, we approximate the direct Cherenkov width with the one for the fluorescence

$$w^{ch-dir} \;\simeq\; w^{flu} \tag{4.24}$$

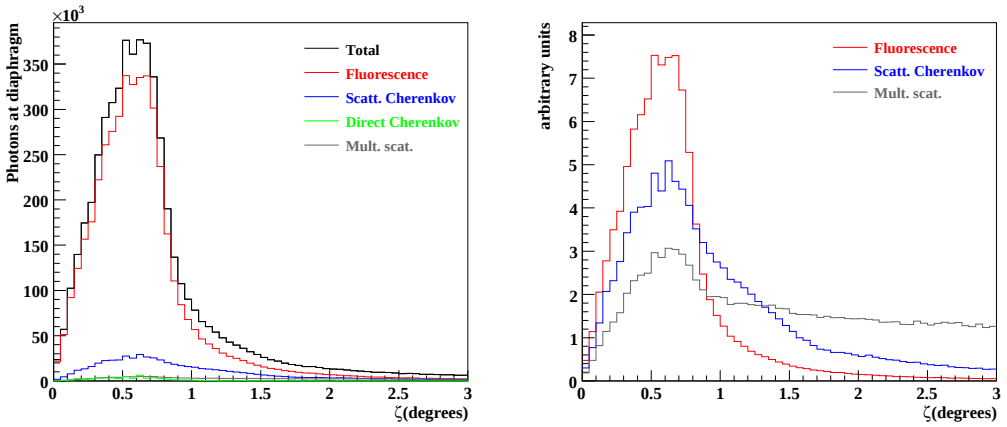


Figure 4.9: On the left: expected number of photons as a function of $\zeta$ calculated with $g^p_{spot} = w^p$. The distributions are for different kind of radiations and have been obtained summing the light coming from the data sample of 300 showers. On the right: the distributions of the left plot for fluorescence, scattered Cherenkov and multiple scattering light are plotted with the same arbitrary normalization to show the different shapes of $w^p$. The width of the direct Cherenkov radiation is assumed to be the same of the fluorescence one.

The width of the scattered Cherenkov radiation is determined by the angular distribution of the Cherenkov photons produced along the shower development. This distribution has been parametrized using simulated showers [103] and it is a function of the shower age and of the atmospheric altitude. From this parametrization it is straightforward to calculate the scattered Cherenkov width [108]. We have implemented the same calculation of $w^{ch-scat}$ as for the standard reconstruction [109]. At each time slot a numerical expression for the Cherenkov width is saved in a histogram and used to generate $\alpha$.

The contribution of the multiple scattered light (MS) has been calculated following [110]. The ratio between the light of multiple scattering and the total light (including the MS) within a circle of radius $\alpha$ is parameterized like:

$$k \;=\; 0.774 \;\left(OD\;\alpha_{scatt}\;d^{1/2}\;\alpha^{1.1}\right)^{0.68} \tag{4.25}$$

where $d$ is the FD-shower axis distance, $OD$ is the total optical depth along $d$ and $\alpha_{scatt}$ is the scattering coefficient. $OD$ and $\alpha_{scatt}$ are wavelength dependent and then $k$ is calculated separately for fluorescence and Cherenkov radiation.

Let be $\tilde{\alpha}$ an arbitrary angle large enough to include the field of view of

all pixels selected for the profile reconstruction. We define the cumulative distribution

$$F_{MS}(\alpha) \;=\; \frac{k(\alpha)}{1-k(\alpha)}\;\frac{1-k(\tilde{\alpha})}{k(\tilde{\alpha})} \tag{4.26}$$

which can be inverted leading to

$$\alpha \;=\; \left[\left(1+\frac{1}{F_{MS}}\;\frac{1-\tilde{k}}{\tilde{k}}\right)\;0.774\;\left(OD\;\alpha_{scatt}\;d^{1/2}\right)^{0.68}\right]^{-\frac{1}{0.68\quad 1.1}} \tag{4.27}$$

With this formalism random values of $\alpha$ in the window $[0,\tilde{\alpha}]$ are obtained generating uniform random values of $F_{MS}$ between $[0,1]$. Notice that from the fraction of multiple scattering, the expected pixel signal (eq.(4.5)) is proportional to number of multiple scattering photons within $\tilde{\alpha}$. It is easy to show that the results are independent of $\tilde{\alpha}$.

Figure 4.9 on the left shows the expected number of photons as function of $\zeta$ calculated with $g^p_{spot} = w^p$, i.e. assuming for both $s$ and $u$ a $\delta$ function. In this way we show the physical widths $w^p$ taking into account only the finite pixel dimension. To underline the different shapes of the distributions, they are shown with the same normalization in the plot on the right. As expected the fluorescence width is narrower than the scattered-Cherenkov one and the multiple scattered light has an approximately flat distribution.

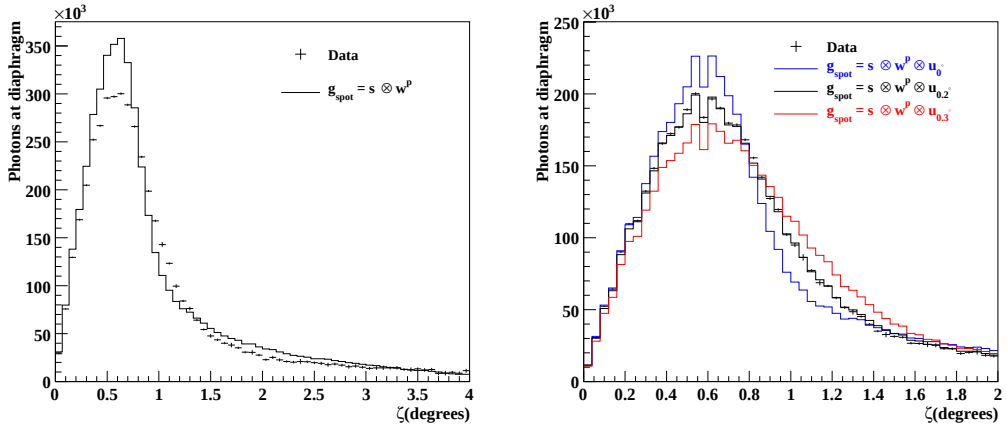


Figure 4.10: Number of photons as a function of $\zeta$ for a sample of 300 showers. The expected distribution in the left picture shows that with $u_{halo}$ alone we are not able to reproduce the data. The figure on the right shows that the peak of the data is well reproduced when a gaussian distribution $u_\sigma$ with $\sigma = 0.2°$ is introduced in the "spot function" calculation.

### 4.4.3 The empirical function $u$

An empirical function $u$ must be introduced in order to achieve a satisfactory agreement with the data. Figure 4.10 on the left shows that the expected $\zeta$ distribution calculated with $g^p_{spot} = s \otimes w^p$ is narrower than the one observed in the data. In particular we observe an expected peak too narrow and for that reason we introduce a gaussian distribution centered in 0 to be convoluted with $s \otimes w^p$

$$u_\sigma = \frac{1}{2\pi} \frac{1}{\sqrt{2\pi}\sigma} \exp\left(-\frac{\alpha^2}{2\sigma^2}\right) \tag{4.28}$$

The $\sigma$ of the gaussian distribution has been determined by making a fit of the data. The minimum was found for $\sigma = 0.2°$. The right plot of figure 4.10 show that the fitted distribution agrees well with the data. On the same plot the expected distribution for two different values of $\sigma$ are also shown.

A possible interpretation of the observed $\sigma$ is the finite resolution on shower geometry. Let's take one event and let's calculate the $\zeta$ distribution after having moved randomly the track position on the camera around the true position. If we repeat this exercise many times and we sum all distributions, we obtain a distribution wider than the one calculated with the true geometry. This would happen also in our case because we sum the light produced in hundred of events. May be it is only coincidence, but 0.2° is very close to the nominal uncertainty on the reconstructed SDP track.

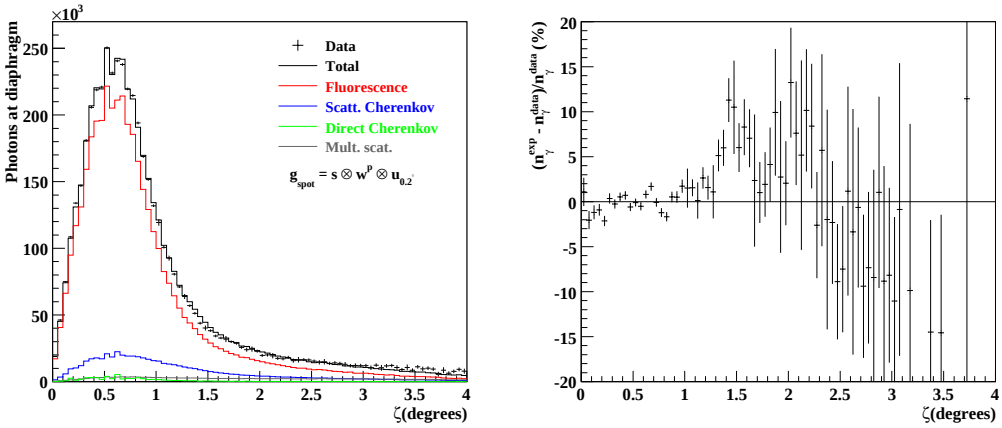


Figure 4.11: Number of photons as a function of $\zeta$ for a sample of 300 showers. On the left: the expected distribution calculated with the halo function and the gaussian distribution are compared with the data. The general agreement is good with the exception of the tail above 3°.

Figure 4.11 compares the data with the expected width calculated with $g_{spot} = s \otimes w^p \otimes u_{0.2^\circ}$. The contributions of each single process are also shown. The residuals between the data and the expected width are plotted on the right figure. There is a good general agreement with the exception of the small tail above 3.0°, larger in the data.

## 4.5 Comparison with standard reconstruction

In this section a comparison on the main shower features is shown. A data sample of about 1000 Golden Hybrid events is used. Those events are selected on the ADST data sample until Dicember 2007 appling the quality cut shown in the next chapter. In figure 4.12 on the left is shown the energy difference

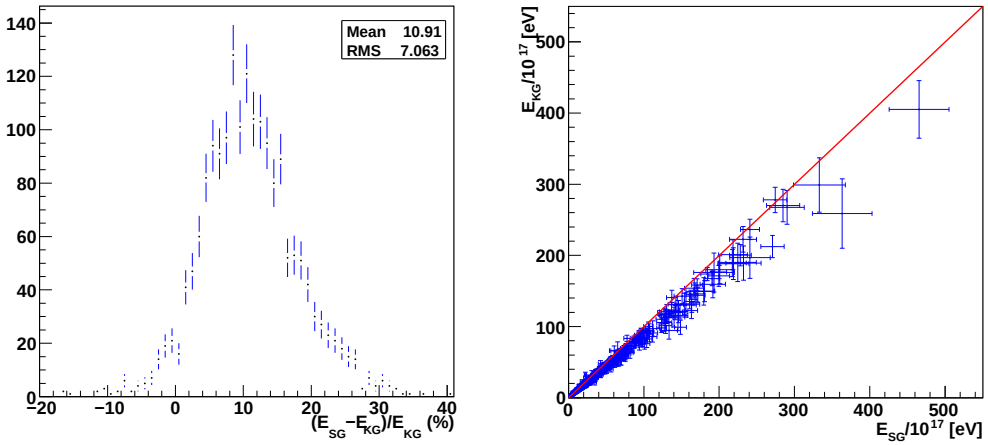


Figure 4.12: On the left: Energy difference between the alternative profile reconstruction method (SG) and the standard shower profile reconstruction (KG). On the right: Energy with uncertainties obtained using both profile reconstruction method, the red line is a visive guide to show the difference respect the KG reconstructed energy.

between the standard shower profile reconstruction (KG) and the alternative profile reconstruction method (SG). The SG method reconstruct the energy about 11% bigger than KG method. In the right panel on figure 4.12 the energy obtained with both method for the data sample with uncertainty is shown.

Another important shower obsevable is the atmospheric depth where the number of shower particle is maximum, $X_{max}$. This observable is imporant to study the mass composition of the cosmic rays. In the left panel on figure

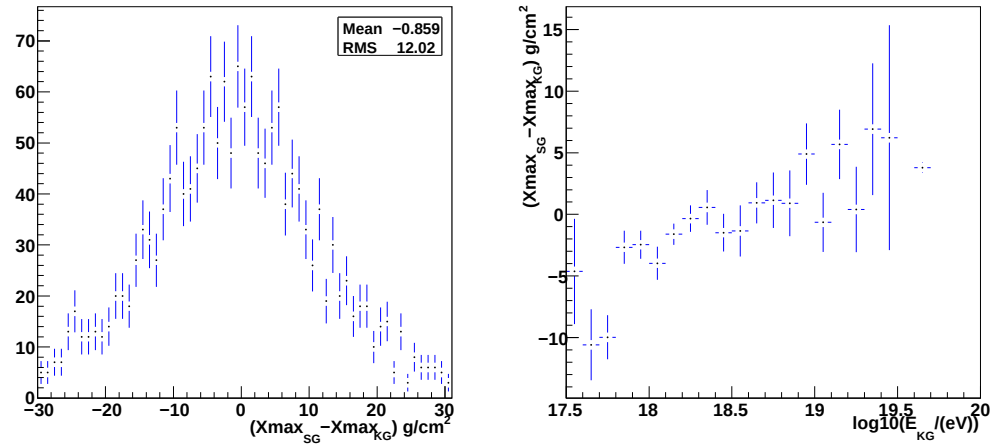


Figure 4.13: On the left: $X_{max}$ difference between the standard shower profile reconstruction (KG) and the alternative profile reconstruction method (SG). On the right: The $X_{max}$ difference on function of energy reconstructed with standard method.

4.13 the $X_{max}$ difference between the standard shower profile reconstruction (KG) and the alternative profile reconstruction method (SG). A differece at level $-10\ g/cm^2$ is obtained for the lower shower energy and $+10\ g/cm^2$ for higher energy (figure 4.13 right panel) .

An important test for the alternative reconstruction method is to compare the fraction of Cherenkov light estimated. In figure 4.14 the good agreement between the reconstruction methods is shown.

### 4.5.1 Conclusion

Using the SG profile reconstruction method to estimate the shower energy for the fluorescence detector events, a 11% of energy bigger than KG profile reconstruction method is obtained. This is due to the different light collection between the methods, and to the different strategy fit procedure.

This value is the systematic uncertainty estimated on the standard longitudinal profile reconstruction procedure. This energy shift affect directly the surface detector calibration curve how is shown at the end of next chapter.

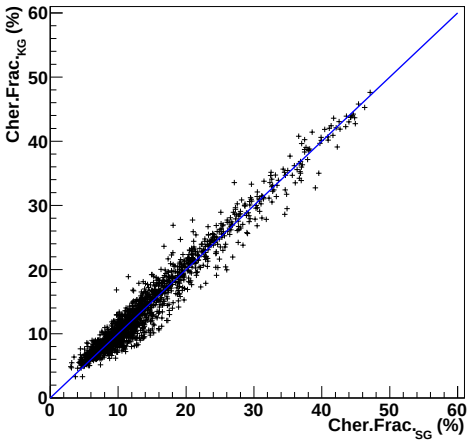


Figure 4.14: Fraction of Cherenkov light calculated with the standard shower profile reconstruction (KG) and the alternative profile reconstruction method (SG).

# Chapter 5

# Energy Calibration

To measure the energy spectrum of UHECR the Pierre Auger Observatory takes full advantage of their two independent detection techniques. The SD, with a duty cycle of 100%, is used to accumulate high statistics. The FD, with a limited duty cycle of around 10%, provides a nearly calorimetric, model-independent energy measurement. Both FD and SD techniques are combined to achieve a spectrum that does not rely on detailed numerical simulations which are dependent on the hadronic interaction model or chemical composition assumed.

The procedure used to assign an energy to each SD event is described. The SD parameter used to characterize the energy of a cosmic ray shower is S(1000) which has been previously described as the signal in VEM units at a distance of 1000 m from the shower core. This parameter will be calibrated by comparison with the energy of the shower measured with the FD.

For a fixed primary energy the S(1000) value will depend on the stage of development of the shower and thus, on the zenith angle. For a shower of a given energy the function that describes the dependence of S(1000) with atmospheric depth, or zenith angle, is called the attenuation curve. The knowledge of this curve will allow us to reduce S(1000) signals to the equivalent S(1000) at a reference zenith angle of 38°, the so-called $S_{38}$ parameter, simplifying the calibration procedure. The attenuation curve can be obtained directly from the data using the so-called Constant Intensity Cut (CIC) method.

Once the attenuation curve is known, a calibration curve relating primary energy and $S_{38}$ is needed. Again the calibration curve is obtained purely empirically using high quality hybrid events for which a direct measurement of the shower energy is performed. The systematic uncertainties involved in the procedure will be discussed.

## 5.1 Attenuation Curve

The S(1000) parameter characterizes the energy of a cosmic ray shower detected by the SD array. As already mentioned, for a given energy S(1000) depends on the stage of shower development and therefore on the zenith angle. The signal recorded by the array decreases with increasing zenith angle due to the attenuation of the shower particles. The function that describes S(1000) as a function of zenith angle for a given primary energy is called the attenuation curve.

The knowledge of this curve is essential to calibrate SD events. It provides a mean to convert the S(1000) signal generated by a shower arriving at a given zenith angle to an equivalent S(1000) that would have produced the shower if it had arrived at a reference zenith angle. In this way, the calibration efforts can be centered in this reference angle that the Pierre Auger Collaboration has been fixed at 38°, the median of the zenith angle distribution of SD events. The attenuation curve can be obtained empirically using SD events in the way described in [117].

The constant intensity cut (CIC) provides a mean to extract the attenuation curve from the data. It relies on two assumptions, that the flux of cosmic rays is isotropic and that the acceptance of the detector is known as a function of zenith angle.

These two assumptions imply that the zenith angle ($\theta$) distribution of cosmic ray showers of energy higher than any threshold is proportional to $\cos\theta \sin\theta$ or, equivalently, that the distribution of $\sin^2\theta$ is uniform. The attenuation curve corresponds to the curve that makes the distribution of $\sin^2\theta$ uniform.

Consider then the intensity $I$ defined as:

$$I(S(1000), \theta) = \frac{dN(> S(1000))}{d\sin^2\theta} \tag{5.1}$$

$I$ is the number of events with signal above a given $S(1000)$ per unit $\sin^2\theta$. Note that $I$ is, by definition and for a fixed value of $\theta$, a decreasing function of $S(1000)$. At a given zenith angle, a given intensity corresponds to a certain lower signal cut in $S(1000)$. The key observation of the CIC method is that equal intensities at two different zenith angles, correspond to the *same* lower energy cut.

Figure 5.1 shows $I$ as a function of $S(1000)$, for different bins in $\sin^2\theta$ (corresponding to different lines). A horizontal line in this plot, a line of constant intensity, corresponds to a line of constant energy.

The attenuation curves at different energies can easily be obtained from this plot: for a given value of the intensity (corresponding to some yet un-

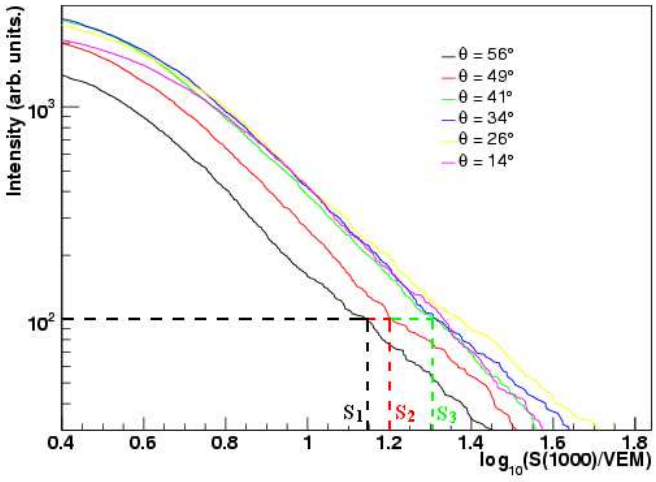


Figure 5.1: Integrated number of events ($I$) as a function of the threshold $S(1000)$. For clarity, only 6 bins were used in this plot.

known but constant value of energy), find the corresponding value of $S(1000)$ for each one of the different $\theta$ bins, obtaining the pairs $\{\theta, S(1000)\}$. These pairs are points that belong to the attenuation curve at the given energy.

The intensity used for deducing the attenuation curve was chosen to be 128, well above the ankle and corresponding to an energy of around 10 $EeV$.

The attenuation curve obtained is:

$$S(1000m) = S_{38}(1 + a\ (\cos^2\theta - \cos^2 38^\circ) + b\ (\cos^2\theta - \cos^2 38^\circ)^2) \quad (5.2)$$

where the parameter $a$ and $b$ are;

$$a = 0.919 \pm 0.055(stat.); \quad (5.3)$$
$$b = -1.13 \pm 0.26(stat.); \quad (5.4)$$
$$(5.5)$$

In figure 5.2 this atteuation curve is shown.

## 5.2 Event Selection from hybrid data

The data sample used to calibrate the energy contains SD events of same quality as in the energy spectrum to avoid possible biases. The only selection applied are T5 condition and requirement of a zenith angle smaller than 60°.

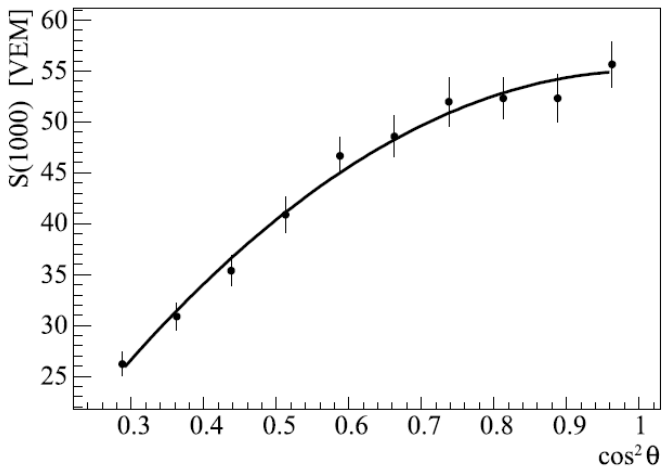


Figure 5.2: Derived attenuation curve, $CIC(\theta)$, fitted with the quadratic function.

### Geometrical cuts

- In order to suppress monocular events with random surface detector triggers, only events with the station used for reconstruction lying within 750 m from the shower axis are accepted.
- As it has been previously mentioned, only events with a reconstructed zenith angle less than 60° are used.

### Shower profile quality cuts

- To ensure a reliable reconstruction, it is required that the reconstructed value of $X_{max}$ (atmospheric depth at the shower maximum development) lies within the observed track range (Fig. 5.3 a).
- as the algorithm used for the profile reconstruction propagates both, light flux and geometrical uncertainties, the estimated uncertainty of shower energy, is a good variable to reject poorly reconstructed showers. We require the uncertainty in $X_{max}$ must be smaller than 40 $g/cm^2$ (Fig. 5.3 b) and the relative uncertainty on the energy less than 20%. (Fig. 5.3 c).
- The presence of a cloud or fog can distort the profile shape significantly. To avoid these events a successful Gaisser-Hillas fit with a reduced $\chi^2$ less than 2.5 for the longitudinal profile is required. (Fig. 5.3 d).

- Profiles with an insignificant shower maxima mainly due to low energy showers are rejected by requiring that the $\chi^2$ of a linear fit to the longitudinal profile exceeds the Gaisser-Hillas $\chi^2$ fit by at least four units (Fig. 5.3 f).

- The maximum allowed amount of Cherenkov light in the signal is 50%. Events with a higher contribution are not considered. (Fig. 5.3 e).

- For events registered by more than one telescope a fraction of the light at the boundaries can be lost. Showers with a hole in the profile greater than 20% of their total length are rejected. If the shower profile reconstruction method described in chapter 4 is used, it's possible to remove this cut.

**Technical cuts**

- Due to the absence of the absolute calibration for Loma Amarilla at the time of this analysis, only events recorded in Los Leones, Los Morados and Coihueco are considered.

- Events are also required to have a contemporaneous measurement of the aerosol content as a function of height available.

Around 2600 events survive to these cuts when they are applied to all events collected from January 1st 2004 to August 31st 2007.

## 5.3 Study of systematic uncertainties on the $S_{38}$ energy calibration

The $E_{SD}$ is affected by several systematic uncertainties involved in the shower reconstruction such as those related with the FD response, the atmosphere or the reconstruction procedure. In the following, the sources of these systematic uncertainties, affecting directly the energy calibration procedure, are discussed [118];

One of these sources, related with the FD performance, is the absolute optical calibration of the telescopes including its wavelength dependence. The uncertainty assigned to the FD absolute calibration performed with the "drum" technique is estimated to be 9.5%.

The ratio between fluorescence intensity and the energy deposited in the atmosphere by shower particles, i.e. the fluorescence yield, has presently an

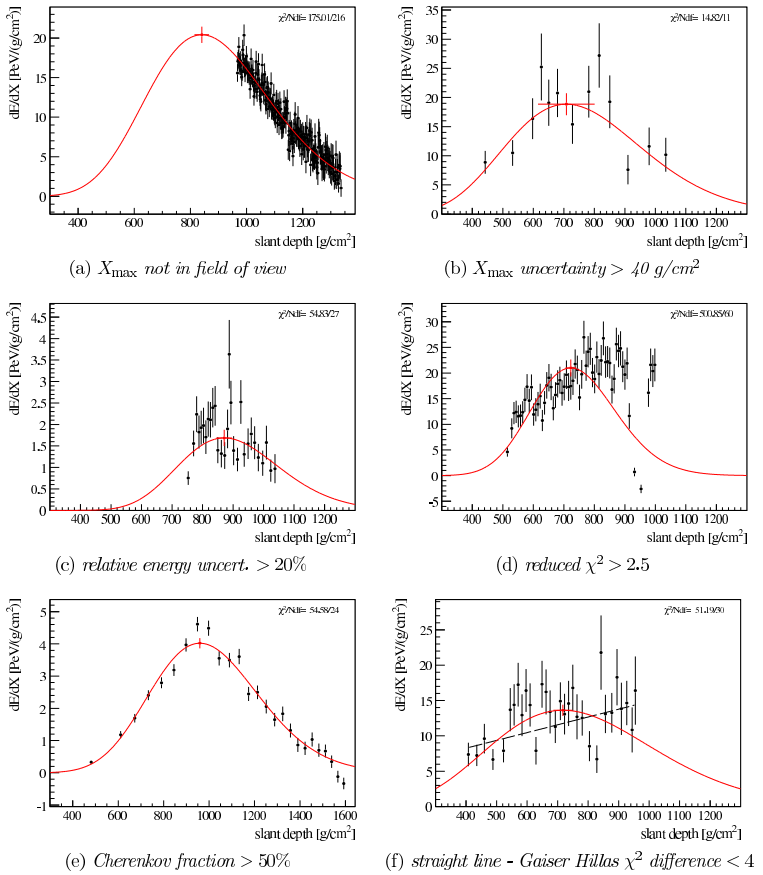


(a) $X_{\max}$ *not in field of view* (b) $X_{\max}$ *uncertainty* $> 40$ *g/cm*$^2$

(c) *relative energy uncert.* $> 20\%$ (d) *reduced* $\chi^2 > 2.5$

(e) *Cherenkov fraction* $> 50\%$ (f) *straight line - Gaiser Hillas* $\chi^2$ *difference* $< 4$

Figure 5.3: Some of the profiles from the events rejected by quality cuts.

uncertainty of 14% [100]. Furthermore, the pressure dependence of the fluorescence yield has been recently measured by the AIRFLY experiment [101], and the corresponding systematic uncertainty is 1%. The fluorescence yield is also dependent on the amount of water vapor. The humidity as a function of altitude has been measured in Malargue using balloon measurements and the fluorescence yield with an without water vapor was compared. The contribution to the systematic uncertainty due to the humidity has been estimated to be 5%. There is also a temperature dependence with an assigned uncertainty of 5%.

Fluorescence light is attenuated by scattering processes with molecules and aerosols. The molecular contribution is studied using monthly models translating into a nearly negligible systematic uncertainty. However aerosol scattering requires a continuous monitoring. The systematic uncertainties in atmospheric attenuation contribute 4% to the total uncertainty for the energy reconstruction.

Along chapter 4 the importance of the light collection in the camera has been emphasized. Care must be taken to collect the fluorescence light coming from the full lateral width of the shower but avoiding the inclusion of night background or multiple scattered light that dominate away from the shower axis. The algorithm used to reconstruct the longitudinal profile of a shower uses the "standard" method based on the maximization of the signal to noise ratio. A set of hybrid events used have been re-analyzed with the algorithm dubbed as the spot method. Energy differences between both procedures at the level of 10% have been observed so an uncertainty of 10% has been assigned to the FD reconstruction method.

There is a final correction in the energy reconstruction due to the energy lost in neutrinos and high energy muons, the so-called "invisible" energy (figure 3.12). This correction is parameterized via shower simulations so that it is dependent on the hadronic interaction model or the composition assumed. A systematic uncertainty of 4% has been estimated for the missing energy correction [105].

These systematic uncertainties are combined in quadrature to give a final value of 22%. A lot of efforts are being dedicated to reduce significantly these uncertainties in order to increase the accuracy of the energy measurements. Table 5.1 summarizes the systematic uncertainties in determining energy by the hybrid method.

### 5.3.1 Event selection criteria and the ellipse cut

The correlation between $S_{38}$ and the energy $E_{FD}$, measured by the fluorescence detector, is studied plotting each hybrid data point on a graph of

| Source | Systematic uncertainty |
|---|---|
| Fluorescence yield | 14% |
| P,T and humidity effects on yield | 7% |
| Calibration | 9.5% |
| Atmosphere | 4% |
| Reconstruction | 10% |
| Invisible energy | 4% |
| TOTAL | 22% |

Table 5.1: Systematic uncertainties in determining energy by the hybrid method. Efforts are underway to reduce the main uncertainties in the fluorescence yield, the absolute calibration, and in the reconstruction method.

$S_{38}$ *vs.* $E_{FD}$. To obtain a surface detector energy calibration curve we need consider the trigger efficiency of the surface detector that is lower than 100% for $S_{38}^{cut} \simeq 15\ VEM$, and cuts the events below this limit.

On the correlation plot $S_{38}$ *vs.* $E_{FD}$, any given pair of $(x, y) = (S_{38}^{cut}, E_{FD}^{cut})$, in the hypothesis of gaussian distributed measurements, we expect the data points to be distributed according to the standard error ellipse with center in $(S_{38}^{cut}, E_{FD}^{cut})$ (see Fig. 5.4). Thus, when we reject events below any line cutting the ellipse, we introduce necessarily a bias. In fact, when averaging over the points of the ellipse above the cut, $(< S_{38} >, < E_{FD} >) \neq (S_{38}^{cut}, E_{FD}^{cut})$. The optimal cut line of slope $B' = -1/B(\sigma_y^2/\sigma_x^2))$ introduced in [117] has the property that the corresponding $(< S_{38} >, < E_{FD} >)$ lies on the calibration line of slope $B$.

This is illustrated in Fig. 5.5.a: the error ellipse becomes a circle in the new coordinates $x' = x\sigma_y/\sigma_x$ and $y' = y$, and the optimal line cut, orthogonal to the calibration line in this coordinate system, guarantees the selected points to be symmetric around the calibration line.

Thus, even if the $(< S_{38} >, < E_{FD} >)$ point is biased, a fit to the data with the optimal line cut will not bias the measurement of slope and intercept of the calibration line.

Another possibility is to use a selection criterium for which $(< S_{38} >, < E_{FD} >) = (S_{38}^{cut}, E_{FD}^{cut})$. This is obtained by selecting events which are in the 90% C.L. ellipse centered in $(S_{38}^{cut}, E_{FD}^{cut})$ (see Fig.5.5.a).

Compared to the optimal line cut, the ellipse selection criterium is in principle less sensitive to the true values of $\sigma_x$ and $\sigma_y$, and does not depend on the slope $B$. Since events are continuosly distributed along the calibration line, we also keep events with energies larger than $E_{FD}^{cut}$.

Our data are distributed according to a steep-falling spectrum. Thus, any selection criterium centered in $(S_{38}^{cut}, E_{FD}^{cut})$ will also accept the spill-over of events of lower energy. If $\sigma_x$ and $\sigma_y$ are energy independent, $(< S_{38} >, < E_{FD} >)$ will still lie on the calibration line both for the optimal line and the ellipse cut, and the measurement of slope and intercept of the calibration line is not biased. This is illustrated in Fig. 5.5.b: the error circle of a point of lower energy will intersect the optimal line cut or the ellipse cut with a distribution of selected points symmetric around the calibration line.

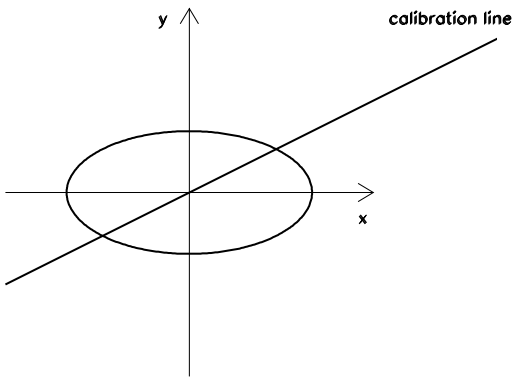


Figure 5.4: The standard error ellipse for a point of the calibration line. Any cut which select only a portion of the ellipse area will bias the position of the reconstructed point.

### 5.3.2 Study of selection criteria with toy Monte Carlo simulations

Toy Monte Carlo simulations, first investigated in [119], are a useful tool to understand biases and systematic uncertainties in the calibration procedure. We used a toy Monte Carlo simulation which includes the energy dependence of the $S_{38}$ uncertainty as implemented in [117]. We also included the larger uncertainty corresponding to events with saturated tanks, according to the fraction of saturated events in the hybrid data sample. The FD energy resolution $\Delta E_{FD}/E_{FD}$ was taken to be $0.08 \pm 0.03$. Events were simulated according to the $E_{FD}$ distribution measured in the hybrid data sample, and the calibration curve was taken as $E = 10^A S_{38}^B$, with $A = 17.080$ and $B = 1.10$.

In order to study the effect of the different event selection criteria, we simulated a sample of events of statistics similar to the data. We applied

the selection criterium under study to the MC sample, and performed a fit of the calibration parameters. All the studies presented in this section were performed with the *linear* fit model (see section 5.3.3), $\log_{10} E_{FD} = A + B \log_{10} S_{38}$.

To reduce the statistical uncertainty, we repeated the procedure 200 times, and obtained the averaged values of the fitted parameters $A$ and $B$. The fitted calibration parameters as a function of $S_{38}^{cut}$ for different selection cuts are shown in Figs. 5.6 and 5.7. For the optimal line cut, Monte Carlo simulations are used to determine the optimal value of the slope of the cut line: $B' = -\frac{1}{B} + \Delta$, and we took $\Delta = -0.65$ [117] .

The ellipse cut was defined by taking $\sigma_{E_{FD}}^{cut} = 0.08 E_{FD}^{cut}$ and $\sigma_{S_{38}}^{cut}$ equal to the expected uncertainty on $S_{38}^{cut}$. The horizontal cut selects the events with $E_{FD} > E_{FD}^{cut}$. From Figs. 5.6 and 5.7, both the ellipse criterium and the optimal line cut appear to provide an unbiased measurement of the calibration curve over a wide range of $S_{38}^{cut}$ . The orthogonal cut introduces a bias, which amounts to $+0.025$ in the parameter $A$, consistent with what found by [119] [117]. There is a clear dependence of the parameter $B$ on the value of $S_{38}^{cut}$ for the orthogonal, the horizontal and the optimal line cuts.

In order to study the sensitivity of the selection criteria to the measurement uncertainties, we performed a simulation with $\Delta E_{FD}/E_{FD} = 0.12 \pm 0.03$. In fitting the calibration curve, we kept $\Delta = -0.65$ for the optimal line cut, and assumed $\Delta E_{FD}/E_{FD} = 0.08$ for the ellipse selection criterium. In this way we can study the effect on the calibration curve of underestimating the $E_{FD}$ uncertainty in the data. The corresponding fitted calibration parameters as a function of $S_{38}^{cut}$ for the ellipse and the optimal line cuts are shown in Figs. 5.8 and 5.9. Sizeable biases on $A$ and $B$ appear with the optimal line cut, while results with the ellipse cut are practically unchanged. This is expected, since a smaller ellipse will in any case provide $(< S_{38} >, < E_{FD} >) \approx (S_{38}^{cut}, E_{FD}^{cut})$ (see section 5.3.1).

We also checked the sensitivity of the ellipse cut to the assumptions on the energy spectrum. For this purpose, we generated events according to a spectral index of 2.5 and 2.7 ($J \propto E^{-\gamma}$), and compared them to the nominal hybrid spectrum. Since we kept fixed the number of generated events in all simulations, the number of events above $S_{38}^{cut}$ depends on the spectral index. In Figs. 5.10 and 5.11, the fitted calibration parameters are compared for different energy spectrums in the simulation. The parameter $B$ is practically independent of the spectrum chosen. The parameter $A$ is flat up to $S_{38}^{cut} \approx 30$ VEM, and then shows a bias increasing with $S_{38}^{cut}$ and the steepness of the energy spectrum. This bias comes from the limited statistics above a given $S_{38}^{cut}$. In fact, even for the steeper spectrum of spectral index 2.70, the bias disappears when a large statistics simulation is performed.

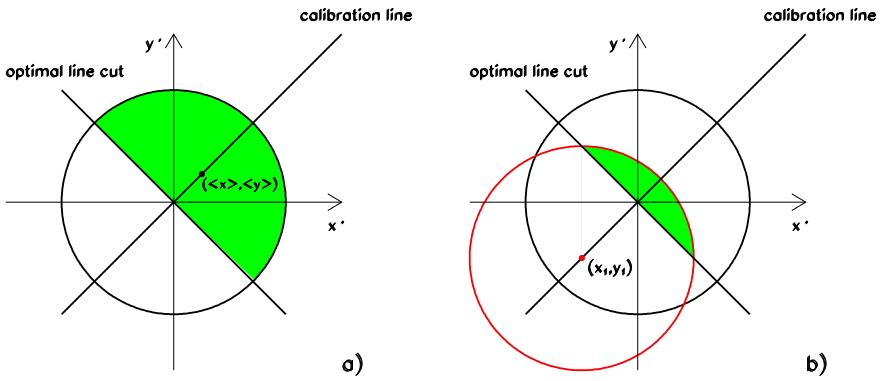


Figure 5.5: a) The optimal line cut, orthogonal to the calibration line in this coordinate system, guarantees the selected points to be symmetric around the calibration line. The $(< x >, < y >)$ lies on the calibration line. For the ellipse cut, $(< x >, < y >)$ would be at the center of the circle. b) The error circle of a point of lower energy $(x_1, y_1)$ intersects the optimal line cut or the ellipse cut with a distribution of selected points symmetric around the calibration line.

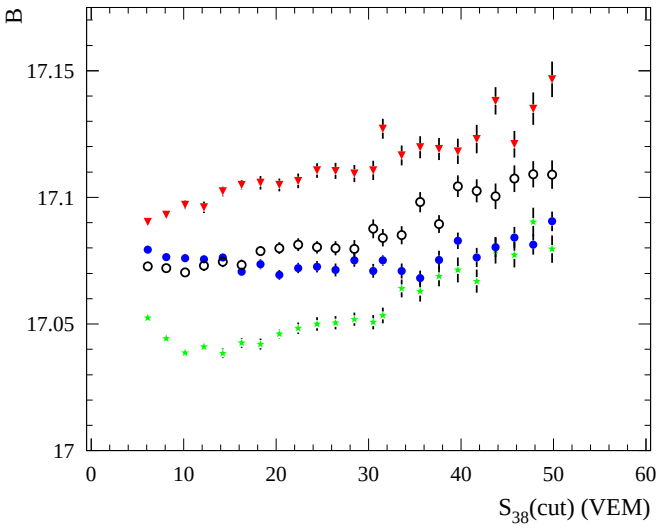


Figure 5.6: MC: Fitted calibration parameter $A$ as a function of $S_{38}^{cut}$ for different selection cuts. Full dots (blue): ellipse cut. Open dots: optimal line cut. Stars (green): horizontal cut. Triangles (red) orthogonal cut.

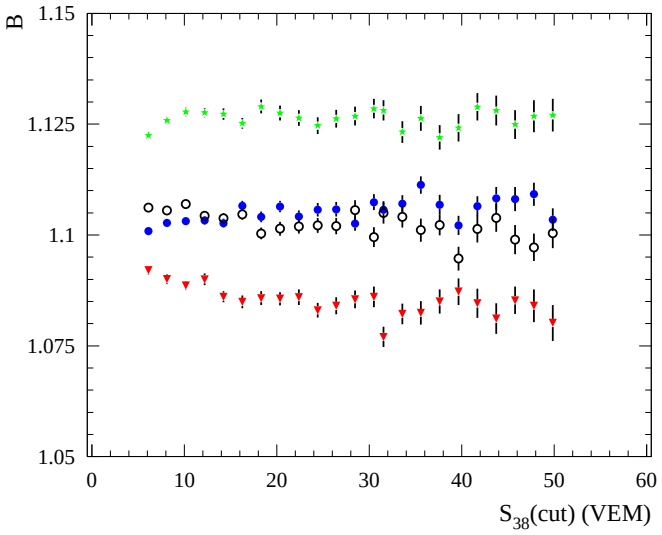


Figure 5.7: MC: Fitted calibration parameter $B$ as a function of $S_{38}^{cut}$ for different selection cuts. Full dots (blue): ellipse cut. Open dots: optimal line cut. Stars (green): horizontal cut. Triangles (red) orthogonal cut.

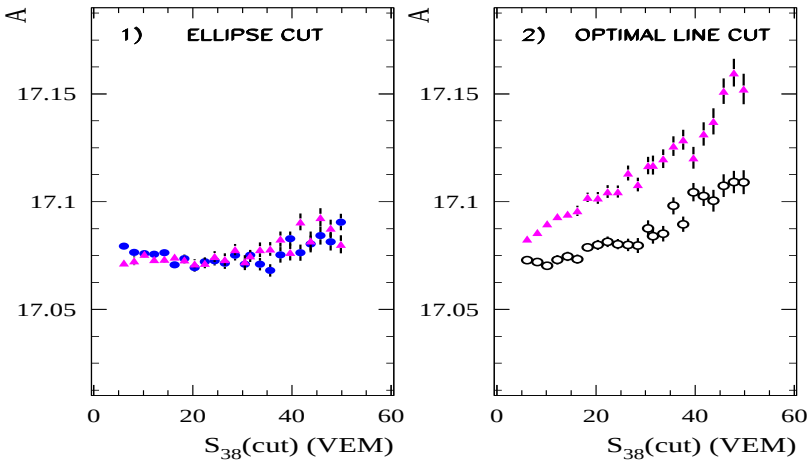


Figure 5.8: MC: Dependence of the fitted calibration parameter $A$ on the $E_{FD}$ uncertainty: 1) the ellipse cut (full dots blue $\Delta E_{FD}/E_{FD} = 0.08$, triangles magenta $\Delta E_{FD}/E_{FD} = 0.12$ ), 2) the optimal line cut (open dots $\Delta E_{FD}/E_{FD} = 0.08$, triangles magenta $\Delta E_{FD}/E_{FD} = 0.12$).

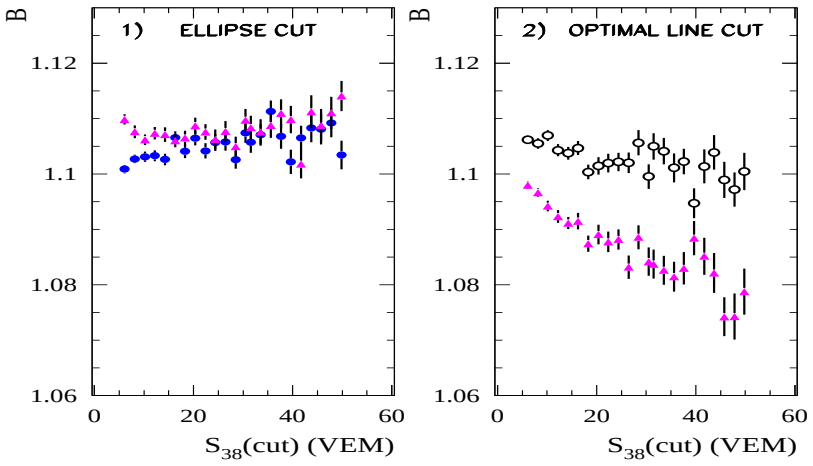


Figure 5.9: MC: Dependence of the fitted calibration parameter $B$ on the $E_{FD}$ uncertainty: 1) the ellipse cut (full dots blue $\Delta E_{FD}/E_{FD} = 0.08$, triangles magenta $\Delta E_{FD}/E_{FD} = 0.12$ ), 2) the optimal line cut (open dots $\Delta E_{FD}/E_{FD} = 0.08$, triangles magenta $\Delta E_{FD}/E_{FD} = 0.12$).

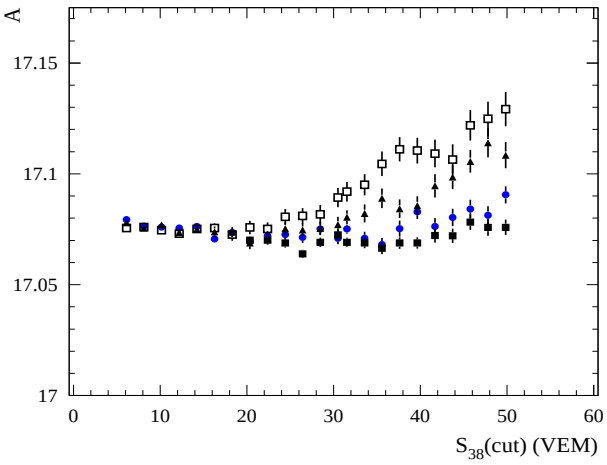


Figure 5.10: MC: Dependence of the fitted calibration parameter $A$ on the energy spectrum: full dots (blue) hybrid spectrum, triangles spectral index 2.5, open squares spectral index 2.7, closed squares spectral index 2.7 large statistics. The ellipse cut was used to select the events.

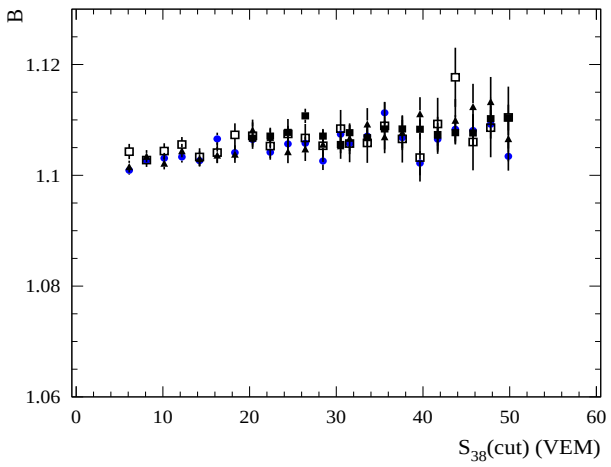


Figure 5.11: MC: Dependence of the fitted calibration parameter $B$ on the energy spectrum: full dots (blue) hybrid spectrum, triangles spectral index 2.5, open squares spectral index 2.7, closed squares spectral index 2.7 large statistics. The ellipse cut was used to select the events.

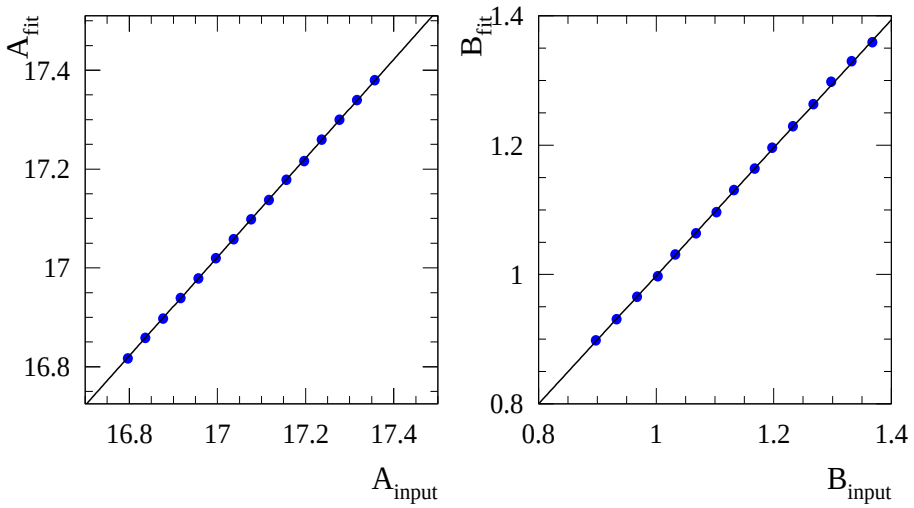


Figure 5.12: MC: Fitted calibration parameters $A$ and $B$ vs the input values in the simulation. While changing one input parameter, the other was kept to its nominal value. The fitted slopes are within 1% of unity.

We also checked that the results do not depend on the particular input value of $A$ and $B$ in the simulation. The correlation between reconstructed values of the calibration parameters and their input values is shown in Fig. 5.12. The correlation is very good.

The Monte Carlo studies presented in this subsection can be of guidance when analyzing the data. Both the ellipse cut and the optimal line cut provide an unbiased calibration curve up to $S_{38}^{cut} \approx 30$ VEM, with no dependence on the hybrid energy spectrum. A detailed knowledge of the uncertainties is needed for the optimal line cut: changing the FD energy resolution from 0.08 to 0.12 (both compatible with the resolution measured in the data), introduces a bias on $A$ of about 0.02. On the other hand, the ellipse cut is robust with respect to assumptions on the measurement uncertainties.

Another important information comes from Figs. 5.6 and 5.7. The orthogonal cut provides an unbiased calibration when the relative uncertainties on $E_{FD}$ and $S_{38}$ are equal. The horizontal cut provides an unbiased calibration in the limit of infinite precision on the FD energy. While we may not know with sufficient precision our measurement uncertainties, the FD energy resolution is certaintly smaller than the $S_{38}$ resolution. From Figs. 5.6 and 5.7, we deduce that the true values of the calibration parameters are always between the ones obtained by the orthogonal and horizontal cut fits. This results does not depend on the specific assumptions made on the uncertainties, and can be very useful when estimating the systematic uncertainty to be associated to the calibration procedure in the data.

### 5.3.3 Fitting procedure

The fitting procedure may introduce biases in the determination of the calibration curve. We have investigated several approaches to the power law fit.

In the *linear* fit, we take $X = \log_{10} S_{38}$ and $Y = \log_{10} E_{FD}$ and minimize the $\chi^2$ (cf. [120]):

$$\chi^2 = \sum_i \frac{(Y_i - A - BX_i)^2}{\sigma_i^2}, \tag{5.6}$$

$$\sigma_i^2 = \sigma_{Yi}^2 + B^2 \sigma_{Xi}^2, \tag{5.7}$$

$$\sigma_{Xi} = \frac{\sigma_{S_{38i}}}{S_{38i}} \log_{10} e \tag{5.8}$$

$$\sigma_{Yi} = \frac{\sigma_{E_{FD}}}{E_{FD}} \log_{10} e \tag{5.9}$$

A power law fit was studied, taking $x = S_{38}$ and $y = E_{FD}$ with $\chi^2$ defined

as:

$$\chi^2 = \sum_i \frac{(y_i - 10^A x_i^B)^2}{\sigma_i^2}, \quad (5.10)$$

$$\sigma_i^2 = \sigma_{yi}^2 + (B10^A x^{B-1})^2 \sigma_{xi}^2, \quad (5.11)$$

$$\sigma_{xi} = \sigma_{S_{38i}} \quad (5.12)$$

$$\sigma_{yi} = \sigma_{E_{FD}} \quad (5.13)$$

We will refer to this fit as the *vertical power law* fit, since it minimizes the vertical distance of each point from the calibration curve.

We also implemented an *orthogonal power law* fit, which was performed with the following procedure. Given a set of parameters $A$ and $B$, that is a trial power law curve, for each point $(x_i, y_i)$ we find the minimum "distance" $R^2_{mini}$ to the power law curve by minimizing:

$$R_i^2 = \frac{(x - x_i)^2}{\sigma_{xi}^2} + \frac{(10^A x^B - y_i)^2}{\sigma_{yi}^2}. \quad (5.14)$$

Then, we minimize the $\chi^2$ defined as:

$$\chi^2 = \sum_i R^2_{mini}. \quad (5.15)$$

This procedure is standard in nonlinear fits, and it is based on the fact that the probability that a true point $A_i = (x, y)$ of the theoretical curve is measured as $B_i = (x_i, y_i)$ is:

$$P(A_i \to B_i) \propto e^{\frac{(x-x_i)^2}{\sigma_{xi}^2}} e^{\frac{(y-y_i)^2}{\sigma_{yi}^2}}. \quad (5.16)$$

We tested the different fitting procedures with the toy Monte Carlo simulation described in section 5.3.2. Results for the *vertical power law* and the *linear* fits are compared in Fig. 5.13. The *orthogonal power law* fit, not shown in the figure, gives results comparable with the *vertical power law* fit. Above $S_{38}^{cut} \approx 15$ VEM, the power law and the linear fits give compatible results, with differences $\Delta A \leq 0.02$ and $\Delta B < 0.01$. This study gives us a feeling of the stability of the result with respect to the fitting procedure.

### 5.3.4 $S_{38}$ energy calibration with data

The data sample corresponding to the ICRC 2007 was analyzed with the insight provided by the studies performed in the previous sections. The fitted

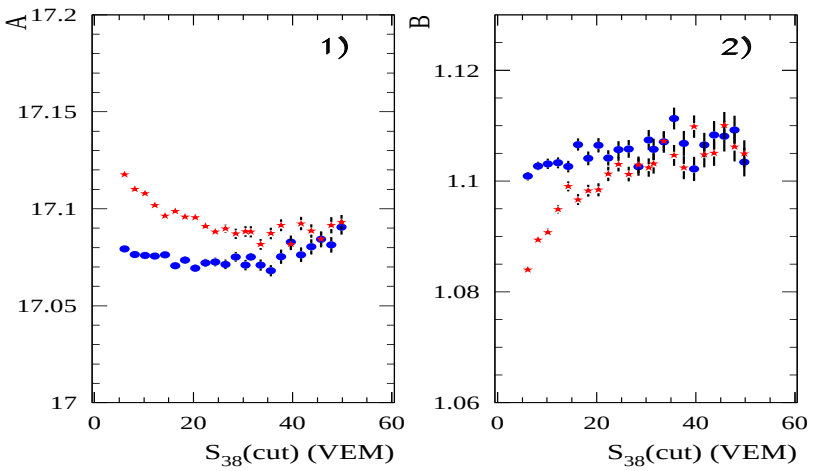


Figure 5.13: MC: Calibration parameter $A$ and $B$ as a function of $S_{38}^{cut}$: full dots (blue) linear fit, stars (red) vertical power law fit.

calibration parameters as a function of $S_{38}^{cut}$ for different selection criteria are shown in Fig. 5.14. Fits were performed with the *vertical power law* model. For the optimal line cut, we took $\Delta = -0.65$ [117].

The ellipse and the optimal line cut provide essentially the same results over a wide range of $S_{38}^{cut}$. The results with the ellipse cut are very stable in the range of $S_{38}^{cut}$ from 10 to 35 VEM, which makes the systematic uncertainty from the particular choice of $S_{38}^{cut}$ negligible. The calibration curve parameters for $S_{38}^{cut} = 15$ VEM with the ellipse selection criterium are:

$$A = 17.167 \pm 0.017_{stat} \quad (5.17)$$

$$B = 1.085 \pm 0.013_{stat}, \quad (5.18)$$

and we will use these values as a reference in the following.

Notice that the ellipse cut selects many more events than the optimal line cut in the region of $S_{38}^{cut}$. This is seen in Fig. 5.15, where the correlation of $S_{38}$ and $E_{FD}$ for $S_{38}^{cut} = 15$ VEM is shown. The ellipse cut selects 652 events, to be compared to 363 selected by the optimal line cut. The agreement on the calibration curves derived from the two selected samples, despite the large difference of events in the region of $S_{38}^{cut}$, is a good indication that both selection criteria are not biased. Also, the calibration parameters from the ellipse and the optimal line cut fits are between the ones obtained by the orthogonal and horizontal cut fits, within a range of $\Delta A \approx \pm 0.04$ and $\Delta B \approx \pm 0.03$ at $S_{38}^{cut} = 15$ VEM. We expect, following the considerations of

section 5.3.2, that the true values of $A$ and $B$ are within these ranges, which thus represent a maximum limit for the systematic uncertainties on $A$ and $B$ coming from biases in the selection cut.

The ellipse cut accepts events with smaller measured $S_{38}$ than the optimal line cut, and one may be worried of a bias due to upward fluctuations of $S_{38}$ close to the detection threshold. This is not apparent in the data, since the ellipse and the optimal line fits are consistent down to $S_{38}^{cut} = 5$ VEM in Fig. 5.14. Also, the data appear to follow the same power law well below $S_{38}^{cut} = 15$ VEM. This can be seen in the correlation between $S_{38}$ and $E_{FD}$ for the full sample of 2616 hybrid events, shown in Fig. 5.16. The correlation of the weighted average of the data points is shown in Fig. 5.17, together with the reference fit calibration curve given by Eqns. 5.17-5.18. It is clear that data follow closely the calibration curve down to $S_{38} \approx 6$ VEM, corresponding to an energy of $\approx 1$ EeV.

The calibration parameters obtained by using the different fitting models of section 5.3.3 are shown in Fig. 5.18. The ellipse cut was used to select events. The two power law fits provide practically identical results. Above $S_{38}^{cut} = 15$ VEM, the difference between the *linear* fit and the *power law* fits is $\Delta A < 0.03$ and $\Delta B < 0.01$.

In Fig. 5.19, the stability of the fitted calibration parameters is shown in a large range of $S_{38}^{cut}$. Events were selected by the ellipse cut, and the *power law* fit was used. The calibration parameters are found to be consistent within one standard deviation of the values at $S_{38}^{cut} = 15$ VEM.

We also checked the stability of the results with respect to the ellipse cut by changing the confidence level from 68% to 95%. The maximum corrections observed were $\Delta A = 0.030$ and $\Delta B = 0.015$.

The various tests presented in this section make us confident that the selection cut and the fitting procedures for the calibration curve are under control. From the current understanding of the calibration procedure, systematic uncertainties $\sigma_{A_{syst}} = 0.03$ and $\sigma_{B_{syst}} = 0.02$ look reasonable. These estimates are within the band defined by the horizontal and vertical cuts, and also take into account the differences in the fitting models.

We will adopt in the following the ellipse cut and the *power law* fit as the reference procedure for the $S_{38}$ calibration curve, and proceed in the estimate of the systematic uncertainties.

### Systematic uncertainties from the hybrid event selection

We studied the stability of the calibration parameter $A$ and $B$ with respect to the selection criteria of the hybrid event sample. For this purpose, each selection cut was removed one-by-one, while keeping the others cuts. In Table

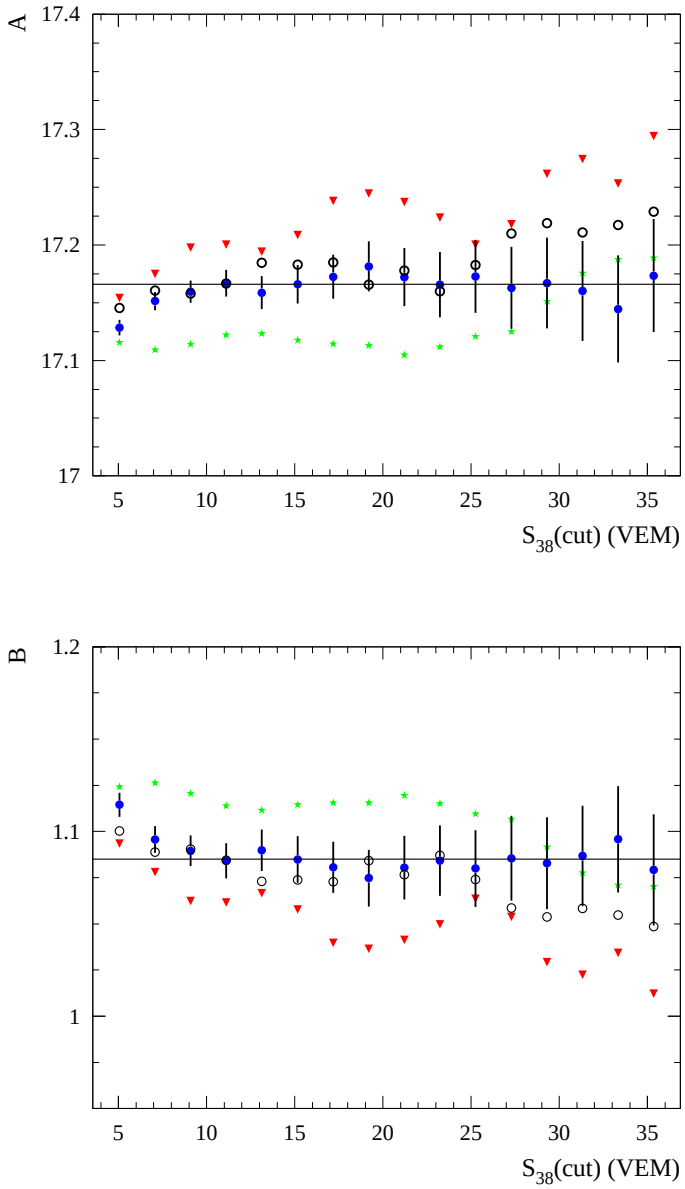


Figure 5.14: DATA: fitted calibration parameters $A$ and $B$ as a function of $S_{38}^{cut}$ for different selection cuts. Full dots (blue): ellipse cut. Open dots: optimal line cut. Stars (green): horizontal cut. Triangles (red): orthogonal cut. Only the uncertainties for the ellipse cut fit are shown for clarity. The horizontal lines correspond to the reference values at $S_{38}^{cut} = 15$ VEM.

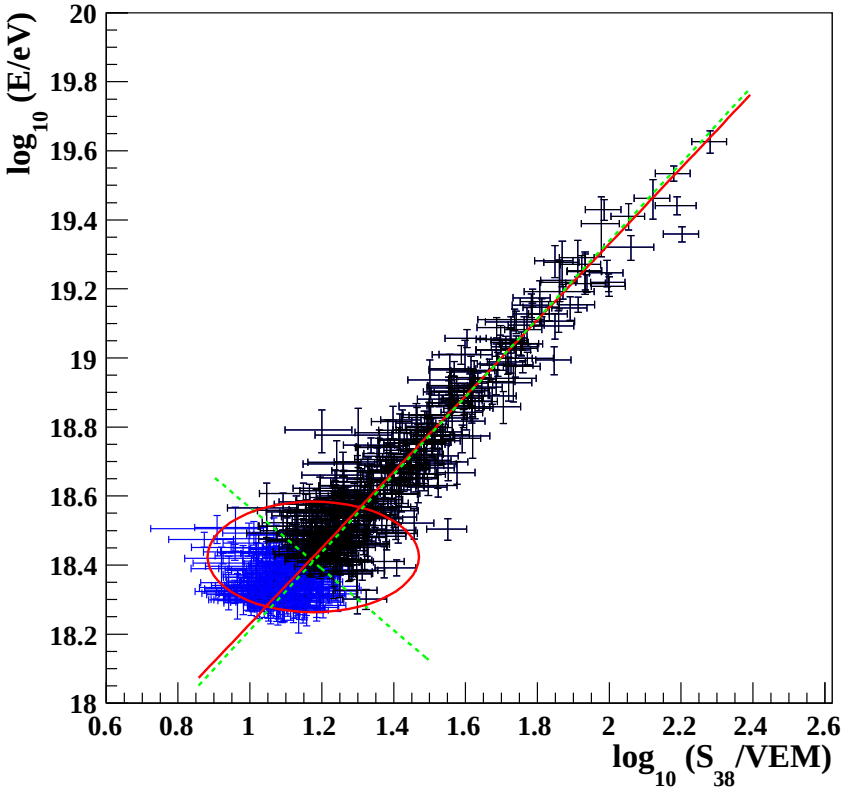


Figure 5.15: DATA: Correlation between $S_{38}$ and $E_{FD}$. Events selected by the optimal line cut at $S_{38}^{cut} = 15$ VEM are represented in black. Additional events selected by the ellipse cut are in blue. The corresponding fitted calibration curves are also shown.

5.2, results are summarized. The number of events in the data sample after removing the selection cut is also reported. The stability of the results is very good, at the level of $\Delta A \leq 0.01$ and $\Delta B \leq 0.005$. Notice, in particular, that the application of the antibias cut, which considerably reduces the statistics of the hybrid sample, does not change significantly the calibration parameters.

We also checked the stability when tightening the selection cuts. In Table 5.2, corresponding results are reported. Also in this case, the observed corrections on the calibration parameters are small.

From this study, it is not obvious that the hybrid selection introduces no systematic uncertainty in the calibration curve. In any case, we conservatively assign a systematic uncertainty $\sigma_{A_{syst}} = 0.010$ and $\sigma_{B_{syst}} = 0.005$.

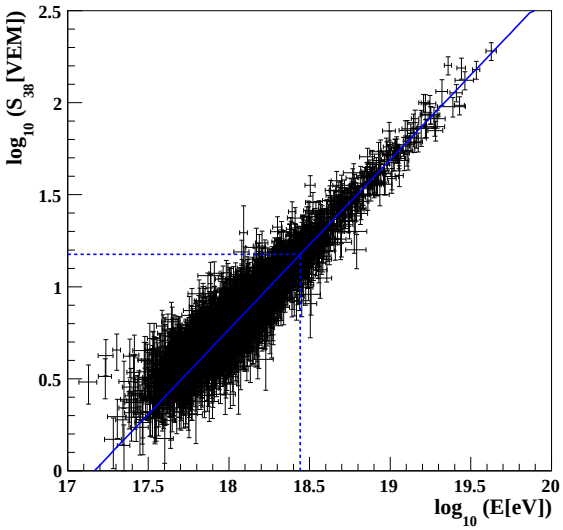


Figure 5.16: DATA: Correlation between $E_{FD}$ and $S_{38}$ for the full sample of hybrid data. The solid line represents the reference calibration curve of Eqns. 5.17-5.18. The dashed lines correspond to $S_{38}^{cut} = 15$ VEM.

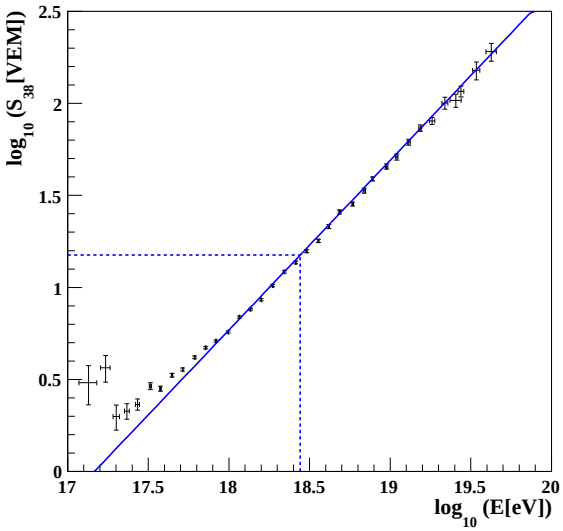


Figure 5.17: DATA: Correlation of the weighted averages of $E_{FD}$ and $S_{38}$ for the full sample of hybrid data. Each data point is obtained from the weighted average of $E_{FD}$ and $S_{38}$ in $\Delta \log_{10} E_{FD}$ bins of fixed size. The solid line represents the reference calibration curve of Eqns. 5.17-5.18. The dashed lines correspond to $S_{38}^{cut} = 15$ VEM.

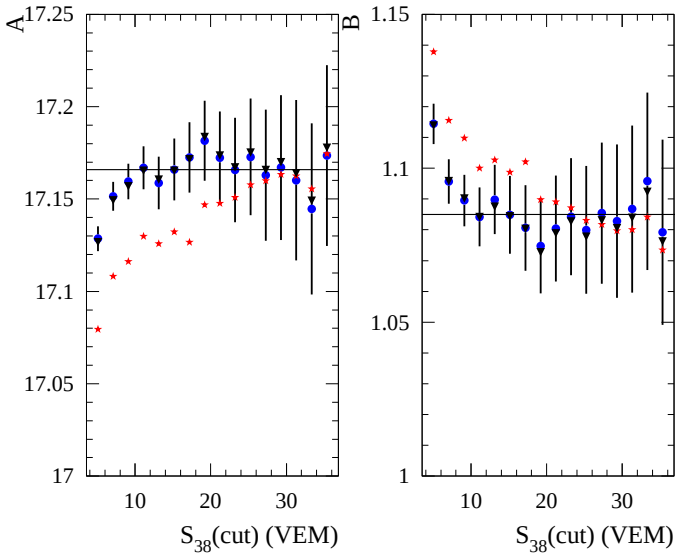


Figure 5.18: DATA: fitted calibration parameters $A$ and $B$ as a function of $S_{38}^{cut}$ for different fitting models. Full dots (blue): *vertical power law* fit. Triangles (black): *orthogonal power law* fit. Stars (red): *linear* fit. Only the uncertainties for the *vertical power law* fit are shown for clarity. The horizontal lines correspond to the values at $S_{38}^{cut} = 15$ VEM.

### Systematic uncertainties from energy dependent sources

A correction in the FD energy scale which is independent of energy is taken into account by the 22% systematic uncertainty assigned to the FD energy. On the other hand, some of the steps involved in the FD energy reconstruction have energy dependencies which may introduce systematic biases in the $S_{38}$ calibration. The following sources have been investigated.

The ratio of fluorescence to Cherenkov light in the reconstructed hybrid showers is energy dependent, since low energy showers tend to have larger Cherenkov contribution. Changing the absolute fluorescence yield will change the energy in a slightly different way at low and high energy, due to the different Cherenkov contribution. We studied this effect by changing the absolute fluorescence yield by its uncertainty ($\pm$13%).

The missing energy correction is energy dependent. To estimate the uncertainty from this source, we corrected the shower electromagnetic energy of a constant 11% independent of energy, which is the average correction for missing energy in the energy range of the hybrid sample, and repeated the $S_{38}$ calibration.

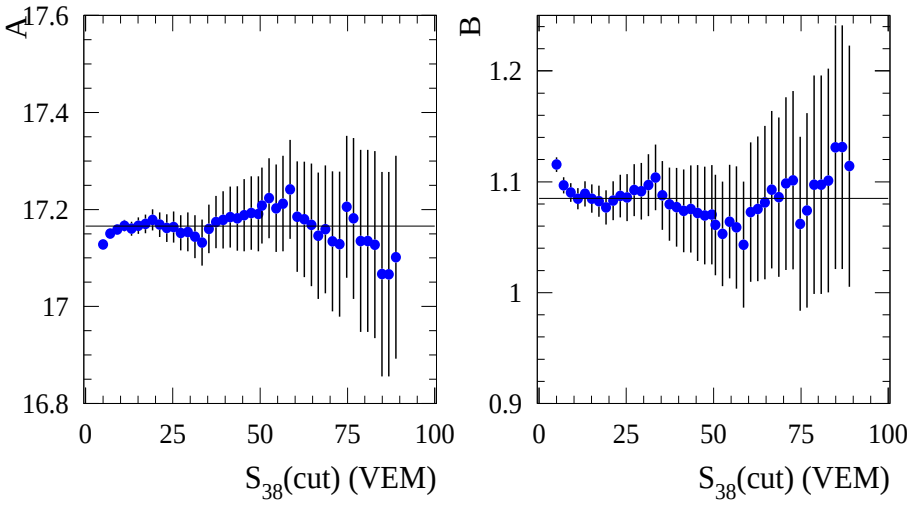


Figure 5.19: DATA: fitted calibration parameters $A$ and $B$ for a large range of $S_{38}^{cut}$. Events were selected with the ellipse cut and the *vertical power law* fit was used. The horizontal lines correspond to the values at $S_{38}^{cut} = 15$ VEM.

In the $S_{38}$ calibration procedure, the FD energy uncertainty due to the VAOD uncertainty was taken as uncorrelated event by event. We studied the effect of the conservative assumption that 50% of the uncertainty is correlated. This introduce a small energy dependence, since large energy events have larger atmospheric corrections.

One of the largest systematic uncertainties we quote on the absolute energy scale is due to the reconstruction procedure, and amounts to 10%. This was estimated by comparing the KG [91] reconstruction with the Spot [107] reconstruction, and accounts for the difference in the collected light on the camera. This difference is found to be also energy dependent. Calibration fits with FD energies from KG reconstruction and from the Spot reconstruction were performed.

In Table 5.4, results are summarized. Corrections on the $B$ parameter are $\leq 0.025$, the largest uncertainty coming from the reconstruction. Notice that corrections in the $A$ parameter for the absolute fluorescence yield, for the missing energy and for the reconstruction model, correspond to global corrections on the energy scale. The 22% systematic uncertainty assigned to the FD energy scale already takes into account these sources, so we should avoid double counting. On the other hand, the $A$ and $B$ parameters are correlated in sign, which should be properly taken into account to avoid overestimation of the systematic uncertainties. In principle, the contributions

| Selection cut | N. of events | $\Delta A$ | $\Delta B$ |
|---|---|---|---|
| $\theta < 60^{\circ}$ | 694 | +0.001 | -0.002 |
| $d_{tank} < 750$ m | 691 | -0.001 | 0 |
| $X_{max}Error < 40 g/cm^2$ | 665 | +0.001 | -0.001 |
| $Fraz.\ Cherenkov < 50\%$ | 657 | -0.001 | +0.001 |
| $\chi^2_{GH}/Ndf < 2.5$ | 672 | +0.005 | -0.005 |
| $\chi^2_{line} - \chi^2_{GH} > 4$ | 710 | +0.008 | -0.004 |
| $Profile\ gap < 20\%$ | 654 | -0.006 | +0.005 |
| *Mie Database Cut* | 1004 | +0.001 | +0.004 |
| *Anti-bias cut* | 378 | -0.001 | +0.003 |
| $X_{max}$ *in FOV* | 668 | +0.003 | -0.003 |
| $\Delta E/E(FD) < 20\%$ | 668 | 0 | 0 |

Table 5.2: Corrections of the fitted calibration parameters with respect to reference value in eq:5.18, obtained by removing each cut, where $\Delta A = A_{corr.} - A_{reference}$ and $\Delta B = B_{corr.} - B_{reference}$. For the antibias cut, the cut is applied. The number of events in the data sample after removing the selection cut is also reported.

from these sources should be taken out from the 22% systematic uncertainty assigned to the FD energy scale, and propagated independently.

### 5.3.5 $S_{38}$ energy calibration with AIRFLY reprocessed data

The fluorescence yield model used in the FD reconstruction for the ICRC 2007, as well as for results presented in section 5.3.4, was taken from [100]. The recent AIRFLY measurement of the pressure dependence of the fluorescence spectrum [121] is now implemented in the FD reconstruction. The hybrid data sample was thus reprocessed with the following set of fluorescence yield parameters: the absolute fluorescence yield of the 337 nm line was taken to be 5.05 photons/MeV at 1013 hPa and 293 K (derived from [100]), and the pressure dependence of all lines was taken from the AIRFLY measurements [121]. The FD energies reconstructed with this new model were found to be only 1.2% higher than the ICRC 2007, and thus we do not expect any significant change with respect to results obtained in section 5.3.4.

The calibration curve parameters for $S_{38}^{cut} = 15$ VEM, the ellipse selection criterium and the *power law* fit were found to be:

$$A = 17.168 \pm 0.017_{stat} \pm 0.032_{syst} \quad (5.19)$$

$$B = 1.088 \pm 0.013_{stat} \pm 0.037_{syst}, \quad (5.20)$$

| Selection cut | N. of events | $\Delta A$ | $\Delta B$ |
|---|---|---|---|
| $\Delta E/E(FD) < 15\%$ | 625 | 0 | -0.001 |
| $Fraz.\ Cherenkov < 20\%$ | 557 | -0.014 | +0.005 |
| $\chi^2_{GH}/Ndf < 1.5$ | 588 | +0.004 | -0.002 |
| $\chi^2_{line} - \chi^2_{GH} > 6$ | 627 | -0.002 | +0.001 |
| $Profile\ gap < 10\%$ | 459 | -0.008 | +0.005 |
| $\theta < 40^\circ$ | 367 | +0.001 | -0.004 |

Table 5.3: Corrections of the fitted calibration parameters $A$ and $B$ obtained by tightening selection cuts. The number of events in the data sample after applying the selection cut is also reported.

| Source | $\Delta A$ | $\Delta B$ |
|---|---|---|
| $Absolute\ yield + 13\%$ | -0.051 (*) | -0.002 |
| $Absolute\ yield - 13\%$ | +0.041 (*) | +0.003 |
| $Missing\ Energy$ | -0.017 (*) | +0.014 |
| $VAOD\ + 50\%$ | -0.001 | +0.010 |
| $VAOD\ - 50\%$ | -0.009 | -0.002 |
| Reconstruction | +0.055 (*) | -0.025 |

Table 5.4: Study of energy dependent corrections on calibration curve parameter. Thw systematic uncertainties already included in the 22% FD absolute energy scale uncertainty are indicated with a (*).

practically the same of Eqns. 5.17-5.18. The quoted systematic uncertainties have been obtained from section 5.3.4, and are summarized in Table 5.5. To calculate the total systematic uncertainties, the individual contributions are summed in quadrature. The statistical uncertainties of $A$ and $B$ are anticorrelated. From Tables 5.2-5.3-5.4, systematic uncertainties of $A$ and $B$ are also in large part anticorrelated.

### 5.3.6 Systematic uncertainty on the spectral index

If we assume that the energy spectrum is described by a power law $E^{-\gamma}$, it can be shown that a correction of the calibration slope $\Delta B = B - B_{true}$ changes the spectral index by:

$$\frac{\Delta\gamma}{\gamma} = \frac{1-\gamma}{\gamma}\frac{\Delta B}{B}. \tag{5.21}$$

For a spectral index $\gamma \approx 2.6$, one obtains $\Delta\gamma/\gamma \approx -0.6\Delta B/B$. Using Eqn.(5.21), The systematic uncertainty on the spectral index due to the $S_{38}$

| Source | $\sigma_{A_{syst}}$ | $\sigma_{B_{syst}}$ |
|---|---|---|
| Ellipse cut and fit | ± 0.030 | ± 0.020 |
| Hybrid selection | ± 0.010 | ± 0.005 |
| Absolute yield | - | ± 0.003 |
| Missing energy | - | ±0.014 |
| VAOD | ± 0.009 | ± 0.010 |
| Reconstruction | - | ±0.025 |
| TOTAL SYST. | ±0.033 | ±0.037 |

Table 5.5: Summary of systematic uncertainties on the calibration curve parameters.

energy calibration procedure can be estimated from the statistical uncertainty of the $B$ parameter and its systematic uncertainties reported in Table 5.5 . Results are summarized in Table 5.6, for $\gamma = 2.62$.

| Source | $\Delta\gamma$ |
|---|---|
| $B$ stat. uncertainty | ±0.019 |
| Ellipse cut and fit | ±0.030 |
| Hybrid selection | ±0.007 |
| Absolute yield | ±0.004 |
| Missing energy | ±0.021 |
| VAOD | ±0.015 |
| Reconstruction | ±0.037 |
| TOTAL | ±0.058 |

Table 5.6: Estimated systematic uncertainties on the spectral index $\gamma$.

### 5.3.7 Summary

We have performed a detailed study of the $S_{38}$ energy calibration procedure and its systematic uncertainties. In particular, we investigated a criterium which provides an unbiased sampling of the events distribution around $S_{38}^{cut}$, by selecting events staying within the 90% CL error ellipse with center in $(S_{38}^{cut}, E_{FD}^{cut})$.

Systematic uncertainties from the selection cut, the fitting procedure, the hybrid events selection and energy dependent effects have been estimated. The parameters of the calibration curve $E = 10^A S_{38}^B = R S_{38}^B$ for the hybrid

data sample reprocessed with recent AIRFLY measurement are:

$$\begin{aligned} A &= 17.168 \pm 0.017_{stat} \pm 0.033_{syst} \\ R &= (1.47 \pm 0.06_{stat} \pm 0.12_{syst}) \cdot 10^{17} \text{ eV} \\ B &= 1.088 \pm 0.013_{stat} \pm 0.037_{syst} \end{aligned}$$

The uncertainties on the $A$ and $B$ parameters should be treated as anti-correlated when propagated in the spectrum. We estimate that the current uncertainty on the $B$ parameter will result in a systematic uncertainty of about $\pm 0.06$ on the spectral index.

# Chapter 6

# Measurement of the Energy Spectrum

In this chapter the various steps needed to obtain the cosmic ray flux are described. Statistical and systematic uncertainties are discussed.

The next step to obtain the UHECR flux using the Pierre Auger Observatory SD data is the exposure calculation. In this chapter the exposure calculation is briefly discussed and the flux obtained using the SD data with the systematic uncertainties is shown.

The validity of the reconstruction tools are presently limited to a maximum zenith angle of 60°. As will be shown in this first section, for these zenith angles the array becomes fully efficient for events with an energy above 3 $EeV$. Considering only events for which the detector will be triggered independently of their direction or primary energy, the calculation of the effective area turns out to be purely geometrical. To obtain the total exposure this area is integrated over the time that the detector has been operational and over the covered solid angle.

In the last section, some astrophysical implication are discussed.

## 6.1 Trigger efficiency, aperture and exposure

A first step for the measurement of the energy spectrum is the selection of SD events since good quality showers must be separated from accidental triggers or background events. The T4 and T5 triggers ensure that the selected events are well contained in the SD array and that non-physics events are rejected, therefore providing a good quality reconstruction.

For further purposes such as the calculation of the total exposed area, it is necessary to find the energy above which the trigger efficiency, defined as

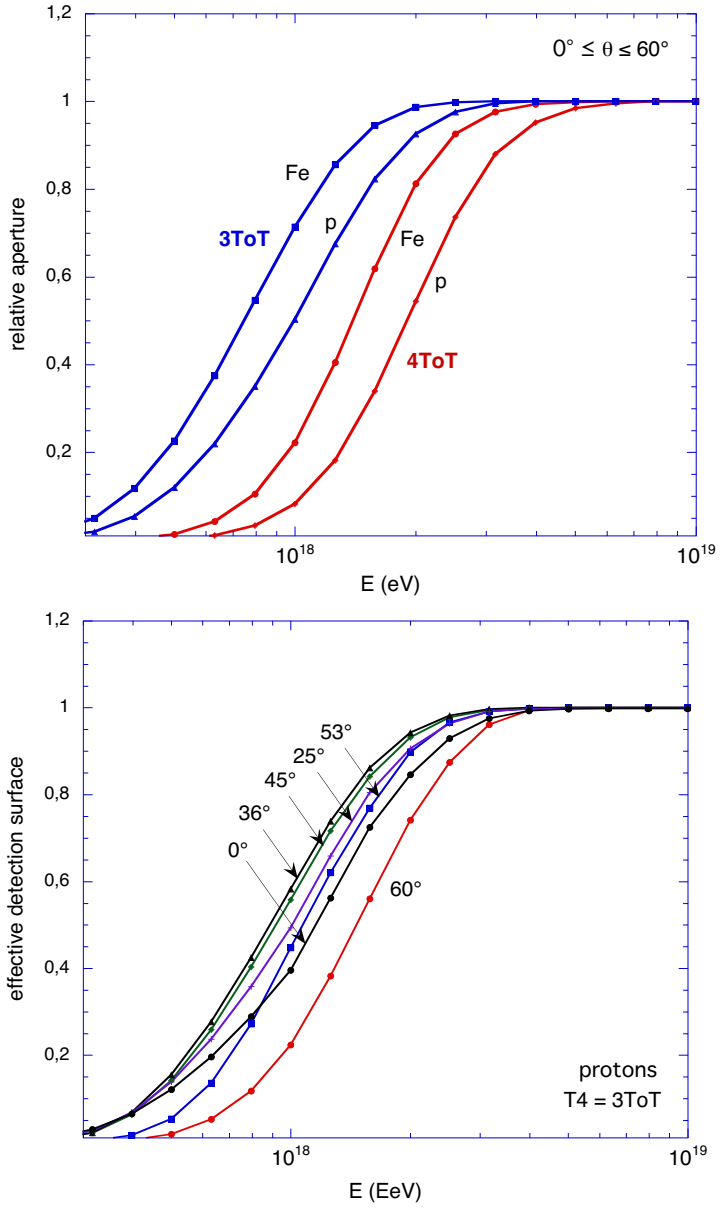


Figure 6.1: Up:Aperture saturation curves for proton or Fe-induced showers, with either 3ToT or 4ToT selection criterion. Down: Effective detection surface as a function of energy for proton showers at different zenith angles.

the probability that the SD event induced by a cosmic ray shower passes the highest level triggers, becomes unit, i.e., the energy above which the array will be triggered independently of the arrival direction, the impact position and the primary mass composition.

This trigger efficiency has been studied in the Pierre Auger Observatory using both Monte Carlo simulations [122] and hybrid data [123].

The Lateral Trigger Probability (LTP) function [122] gives the probability of triggering for a single station as a function of the distance to the shower axis for a given primary mass, energy and arrival direction. Thus, the probability that a given shower produces a T4 trigger (at least three ToT stations in the first ring of neighbours) can be obtained from a combination of this individual tank trigger probabilities. The global shower detection efficiency is then obtained by averaging over all the allowed shower core positions, i.e. satisfying the T5 condition: the closest tank to the core which is expected to record the largest signal must be surrounded by 6 working stations 6.

The effective detection surface of the elementary hexagonal cell, defined as the integral of its area weighted by the global trigger probability, is shown, normalized, for proton simulations in figure 6.1 (left) as a function of primary energy and for different zenith angles. The aperture is then obtained by integrating this effective area over solid angle and is shown in figure 6.1 (right) for two different choices of the T4 condition. For the T4 requirement used in the Pierre Auger Observatory (3ToT stations) the array is fully efficient, i.e. the aperture is independent of energy or primary mass, above $3EeV$ for events with zenith angle below $60^\circ$ .

At full trigger efficiency the aperture of the SD becomes purely geometrical since it is independent of shower energy, arrival direction or mass composition. For a given time, the instantaneous aperture of any array configuration is obtained as a multiple of the elementary aperture $a_{cell}$ defined for the single element. Above $3EeV$ the effective detection area per tank is independent of energy:

$$S_{eff}(\theta) = S_{cell} \cos\theta \simeq 1.95\ km^2 \cos\theta. \tag{6.1}$$

The corresponding aperture will be obtained integrating this area over the solid angle:

$$a_{cell} = S_{cell} \int_0^{\pi/3} \cos\theta\ \sin\theta\ d\theta \int_0^{2\pi} d\phi = 4.59\ km^2\ sr \tag{6.2}$$

The total exposure, defined as the time integration of the total aperture, is therefore easily obtained counting the total number of elementary stations active each second. As for the aperture, the exposure of the SD is also

independent of the energy above 3 $EeV$. Since the array configuration is continuously changing due to the deployment of SD tanks and eventual station failures, the exposure in a fix configuration with $N_{cell}$ elementary cells and a duration$\Delta t$ is incremented in $\Delta\eta$ given by:

$$\Delta\eta = N_{cell}\ a_{cell}\ \Delta t \tag{6.3}$$

The total exposure is calculated summing over all periods with different configurations and arises, previously corrected by dead times in the data taking which could lead to an overestimate of the exposure, to 7000 $km^2\ sr\ yr$ for the period considered to build the energy spectrum, i.e. from January 1st 2004 to August 31st 2007. The uncertainty on the exposure has been estimated to be 3%.

## 6.2 Calibration curve

The analysis described in the chapter 5 it's repeated for the data sample actualized until to August 31st 2007, and the calibration curve parameter used for the [7] are shown.

Statistical uncertainties in $S_{38}$ and $E_{FD}$ were assigned to each event: averaged over the sample these were 16% and 8%, respectively. The correlation of $S_{38}$ with $E_{FD}$ is shown in Fig. 6.2, together with the fit of the data by a power-law, $E = a\cdot\ {S_{38}}^b$.

The results of the fit are:

$$a = (1.49 \pm 0.06(stat) \pm 0.12(syst))\times\ 10^{17}\ \text{eV},$$

$$b = 1.08 \pm 0.01(stat) \pm 0.04(syst),$$

with a reduced $\chi^2$ of 1.1. $S_{38}$ grows approximately linearly with energy.

The energy resolution, estimated from the fractional difference between $E_{FD}$ and the derived SD energy is shown in Fig. 6.3. The RMS of the distribution is 19%, in good agreement with the quadratic sum of the $S_{38}$ and $E_{FD}$ statistical uncertainties of 18%.

The statistical uncertainty on $E_{SD}$ as a function of the energy is shown in the left panel in figure 6.4. The systematic uncertainties is shown in the right panel in figure 6.4.

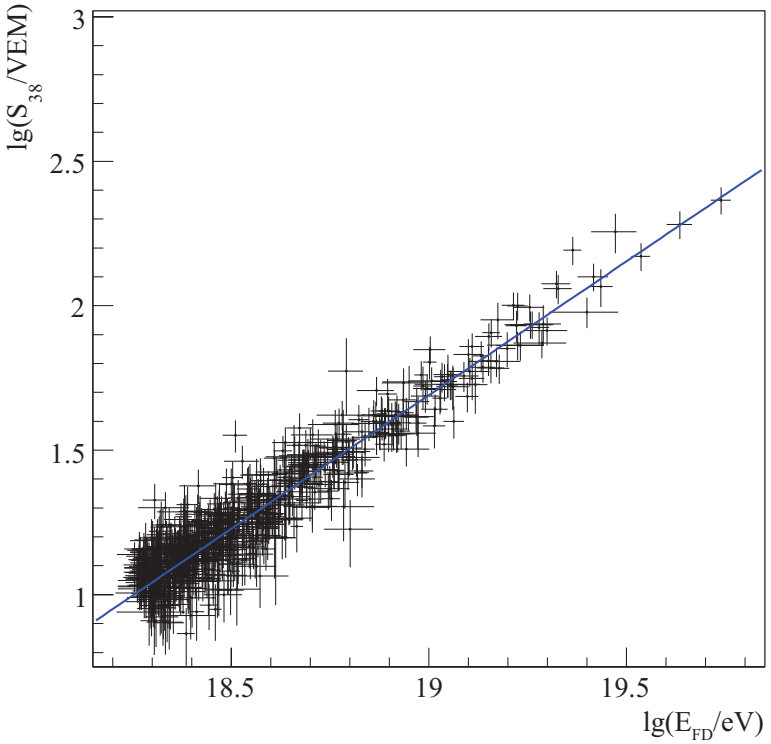


Figure 6.2: Correlation between $\lg(S_{38})$ and $\lg(E_{FD})$ for the 661 hybrid events used in the fit. The full line is the best fit to the data.

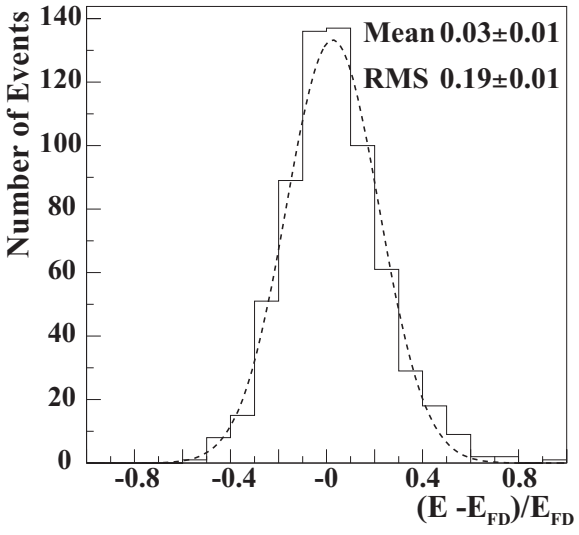


Figure 6.3: The fractional differences between the two energy estimators.

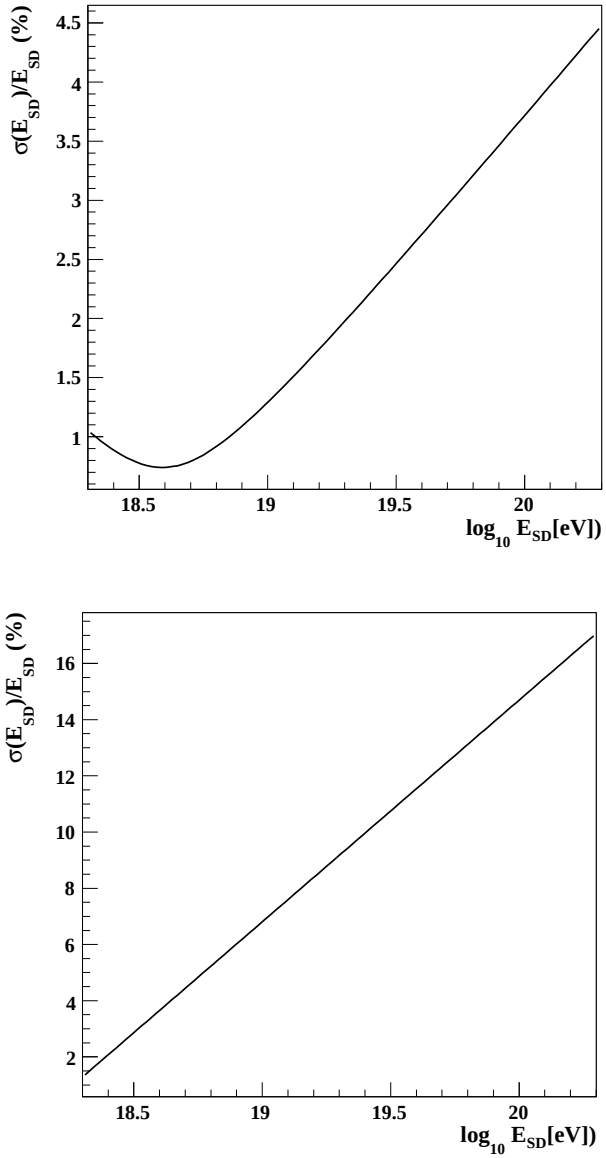


Figure 6.4: Up: The statistical uncertainties on calibration curve propagated to $E_{SD}$ energy. Down: The systematic uncertainties on calibration curve propagated to $E_{SD}$ energy.

## 6.3 Calibration Curve using the Spot Reconstruction

The analysis described in the chapter 5 it's repeated for the data sample actualized until to August 31st 2007.

The procedure shown it's used for the data obtained using this hybrid data sample, where the FD events are reconstructed with the spot profile reconstruction method developped in this work (chapter 4) and the SD events are reconstructed using the standard procedure (chapater 3).

The differents shown in section 4.5 is propagated in the calibration curve. The calibration curve parameters obtained using this profile reconstruction method are:

$$\begin{aligned} a &= (1.96 \pm 0.08_{stat}) \cdot 10^{17} \text{ eV} \\ b &= 1.056 \pm 0.013_{stat} \end{aligned}$$

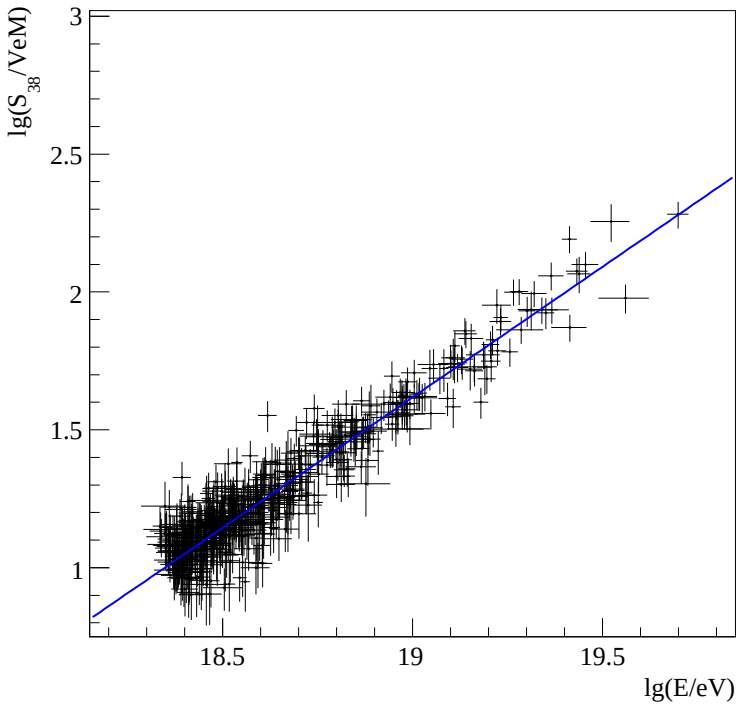


Figure 6.5: Correlation between $S_{38}$ and $E_{FD}$. The energy $E_{FD}$ is obtained using the alternative reconstruction method (SG) described in chapter 4 The corresponding fitted calibration curve is also shown.

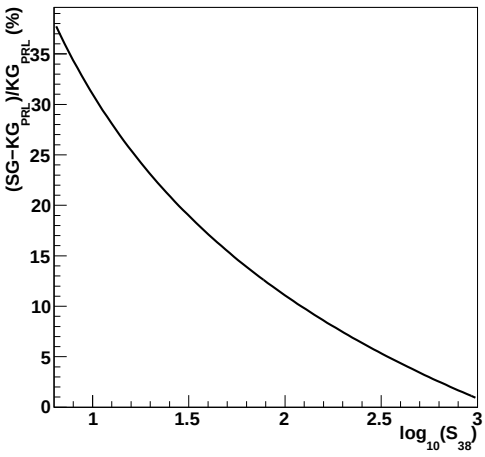


Figure 6.6: The relative difference bewtween the calibration curve obtained using the spot reconstruction method and the standard profile reconstruction method on function of $S_{38}$.

In Figure 6.5 the energy reconstructed for the events, obtained by the spot longitudinal profile reconstruction methods, are shown with the fitted calibration curve. The difference respect the standard profile reconstruction methods is shown in Figure 6.6.

## 6.4 Cosmic ray flux from the surface detector data

The differential flux $J(E)$ has been calculated for nearly 20000 events recorded by the SD in the considered time period, from January 1st 2004 to August 31st 2007. $J(E)$ is defined as:

$$J(E)\Delta E \;=\; \frac{N(E)}{\eta} \tag{6.4}$$

where $\eta$ is the total exposure, $N(E)$ is the total number of collected SD events with a reconstructed energy contained in a bin centered in $E$ and width $\Delta E$. The measured flux $J(E)$ versus reconstructed energy, is shown in figure 6.7. Error bars correspond only to statistical uncertainties and 84% CL calculated according to [124]. A 22% systematic uncertainty in the absolute energy scale comes from the FD energy estimate. In addition, the energy scale is also affected by an energy-dependent systematic uncertainty due to the calibration procedure. The spectrum is fitted by a smooth tran-

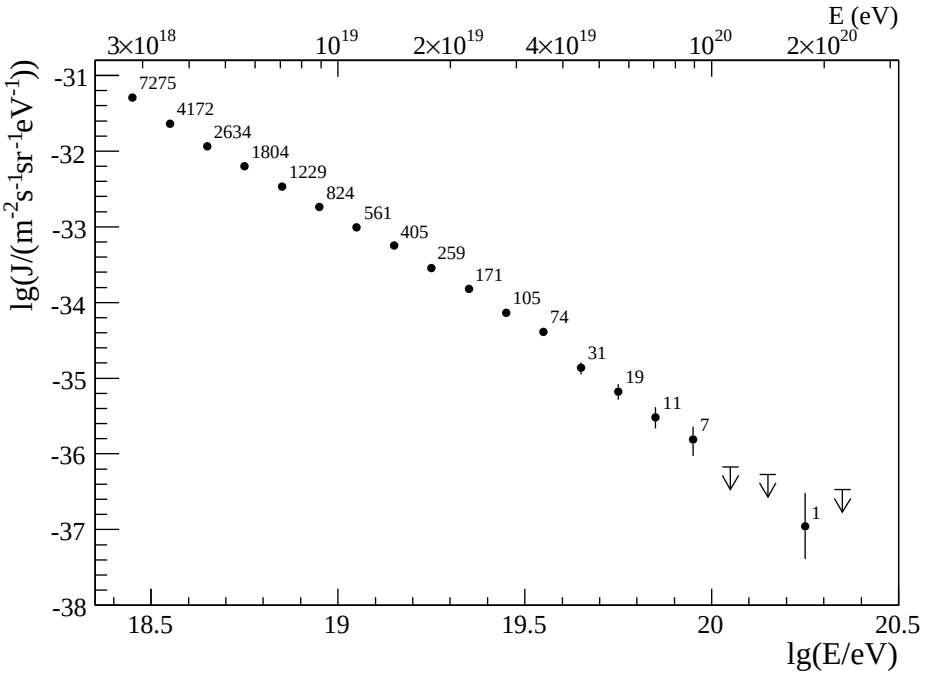


Figure 6.7: The differential flux $J$ as a function of energy, with statistical uncertainties.

sition function with the suppression energy of $4 \times 10^{19}$ $eV$ defined as that at which the flux falls below an extrapolated power law by 50%. To examine the spectral shape at the highest energies, we fit a power-law function between $4 \times 10^{18}$ $eV$ and $4 \times 10^{19}$ $eV$, $J \propto E^{-\gamma}$, using a binned likelihood method [125]. A power-law is a good parameterization: the spectral index obtained is $2.69 \pm 0.02(\text{stat}) \pm 0.06(\text{syst})$ (reduced $\chi^2 = 1.2$), the systematic uncertainty coming from the calibration curve. The numbers expected if this power-law were to hold above $4 \times 10^{19}$ $eV$ or $10^{20}$ $eV$, would be $167 \pm 3$ and $35 \pm 1$ while 69 events and 1 event are observed. The spectral index above $4{\times}10^{19}$ $eV$ is $4.2{\pm}0.4(\text{stat}){\pm}0.06(\text{syst})$. A method which is independent of the slope of the energy spectrum is used to reject a single power-law hypothesis above $4{\times}10^{18}$ $eV$ with a significance of more than 6 standard deviations [125], a conclusion independent of the systematic uncertainties currently associated with the energy scale. In Fig. 6.8 the fractional differences with respect to an assumed flux $\propto E^{-2.69}$ are shown. HiRes I data [126] show a spectral index 2.81 where our index is 2.69 while the position of suppression agrees within the quoted systematic uncertainties.

In Fig. 6.8 the Auger event calibrated using the calibration shower figure 6.2 and the Hires I scaled with $E^3$ are shown. The Auger flux obtained using

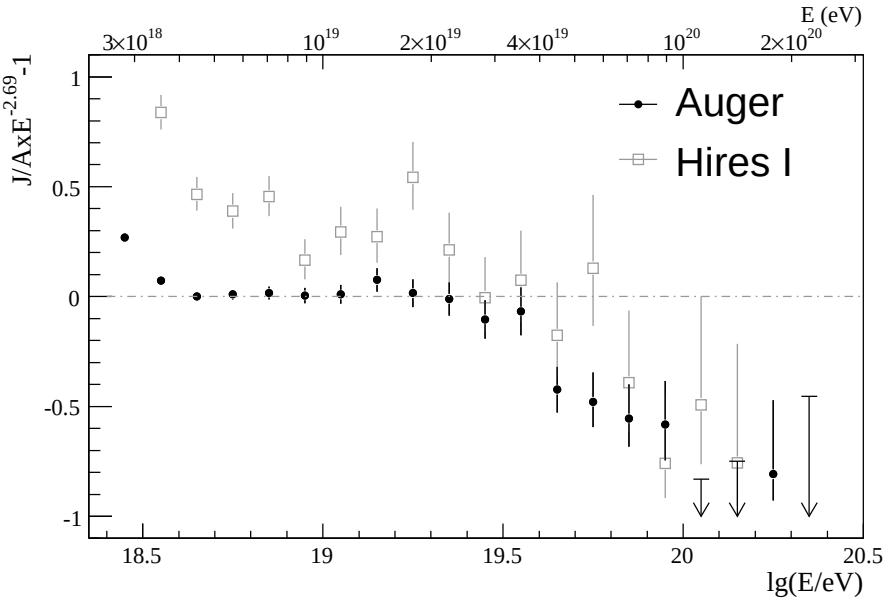


Figure 6.8: The fractional differences between Auger and HiRes I data [126] compared with a spectrum with an index of 2.69.

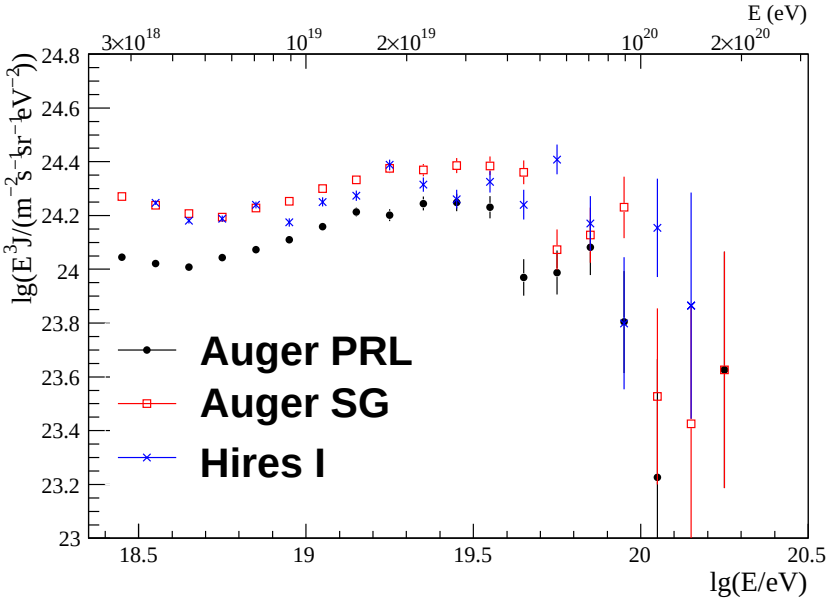


Figure 6.9: The Auger flux obtained by the calibration derived by figure 6.2, the HiRes I flux, and the Auger events calibrated using the Spot method for the longitudinal profile reconstruction are shown.(PRELIMINARY RESULT NOT APPROVED BY THE AUGER COLLABORATION).

the calibration curve by the Spot reconstruction method is shown. For this plot preliminary SD data from January 2004 to June 2008 are used with exposure of 10300 $km^2$ $sr$ $yr$.

## 6.5 Cosmic ray flux: astrophysical implications

The existing data on the cosmic ray spectrum over a wide energy range is presented in fig. 6.10. The inconsistency between different measurements at the highest energies is within the systematic uncertainties on the energy scale of the experiments.

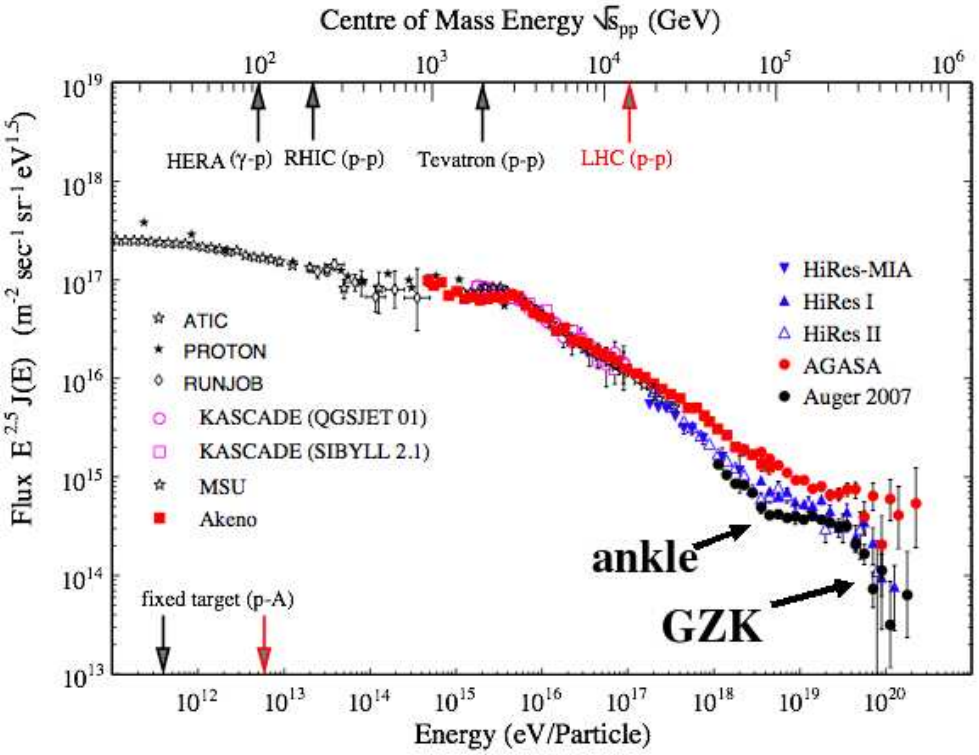


Figure 6.10: Cosmic rays spectrum detected by several experiments, multiplied by $E^{2.5}$.

The cosmic ray spectrum follows a power law $dN/dE \propto E^{-\gamma}$ over many orders of magnitude. At the highest energies one has three remarkable features. The *knee*, a steepening of the flux by $\Delta\gamma \approx 0.5$ at the energy of few

$PeV$, followed by a flat region called the *ankle* at several $EeV$ and the flux suppression in the GZK region. The first two features are suspected to be an indication of the end of the galactic cosmic ray spectrum and the transition to an extra-galactic component. This interpration is supported by the fact that at the *ankle* energies the particles can't be magnetically bound to the Galaxy.

In the following we present three different theoretical models to describe the cosmic ray spectrum at the highest energies (see [127, 128, 129, 130] for recent reviews on this topic). In these models the extra-galactic sources of the cosmic ray are described essentialy by four parameters [131]:

- the source emissivity (needed to adjust the overall normalization),
- the spectral index $\gamma_0$ of the energy spectrum at the source,
- the maximum energy $Z \cdot E_{\mathrm{c}}$ at which the source accelerates the particles,
- the cosmological source evolution parameter $m$, describing the source density $n$ as a function of redshift $z$, $\mathrm{dn/dz} \propto (1+z)^m$.

In order to simplify the discussion, we consider only the case of uniform source distribution ($m = 0$).

In the so-called *dip model* [132], all extragalactic cosmic rays are assumed to be protons that interact with the microwave background radiation (Fig. 6.11). The ankle is essentialy determined by the interactions followed by an $e^+e^-$ production. The steepening at $\sim 10^{20}$eV is interpreted as a GZK cutoff. The experimental data are well described only if an hard injection spectrum at the source is assumed. However this is problematic in terms of the overall energy luminosity of extra-galactic sources if extrapolated to low energies. Therefore an 'artificial' softening of the spectrum below a certain energy is usually introduced. Notice that the dip-model does not work for heavy nuclei because the threshold for $\mathrm{e^+e^-}$-production is proportional to the energy per nucleon and thus only relevant for protons at the energies of the ankle.

In *mixed composition models* [133, 134] the extra-galactic cosmic ray composition is assumed to be equal to the one measured at low energies in our galaxy. Due to the Lorentz-factor dependence of the energy loss, the individual spectra of nuclei with mass $A$ are subsequently suppressed at energies above $\gtrsim A \cdot 10^{18}\ eV$. As in case of the dip-model, this ansatz gives a good description of the existing data (Fig. 6.12b), but with a much softer extra-galactic source spectrum. The transition from galactic to extra-galactic

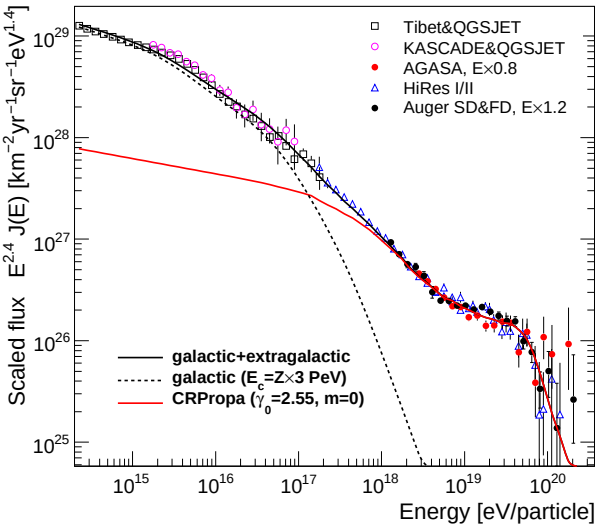


Figure 6.11: Models of the transition from galactic to extra-galactic cosmic rays vs. measurements of the all particle flux: Extragalactic protons [131].

cosmic rays is at about a factor 10 higher energies close to 1 $EeV$ and correspondingly, this model needs galactic sources with a higher maximum acceleration energy than the dip-model.

The last model is called (*ankle model*). The ankle-feature are reproduced by the intersection of a flat extra-galactic component with a steep galactic one.

In this case, as shown in Fig. 6.13, the galactic cosmic ray spectrum extends to energies well above several EeV.

The traditional way to reproduce the ankle-feature is to model it as the intersection of a flat extra-galactic component with a steep galactic component (*ankle model*). In that case, as can be seen in Fig. 6.13, the galactic cosmic ray spectrum extends to energies well above several EeV.

More than forty years after Greisen, Zatsepin and Kuzmin (GZK) predicted a suppression of the cosmic ray flux due to interactions with the cosmic microwave background (CMB) radiation and its existence has now finally been established with high significance by HiRes and the Pierre Auger Observatory [126, 7] (Fig. 6.14).

As can be seen in Fig. 6.14, the current statistical precision of the flux measurements at ultra-high energies is not sufficient to distinguish between the predictions for the spectral shape for cosmic rays with a pure proton

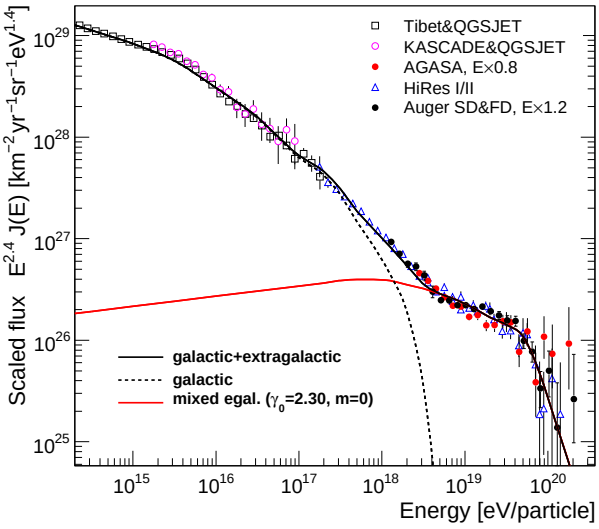


Figure 6.12: Models of the transition from galactic to extra-galactic cosmic rays vs. measurements of the all particle flux: Mixed Composition [131, 133].

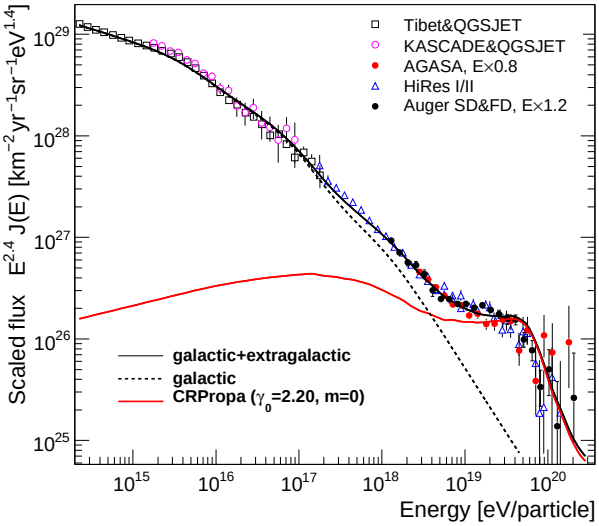


Figure 6.13: Models of the transition from galactic to extra-galactic cosmic rays vs. measurements of the all particle flux: Transition at the ankle [131].

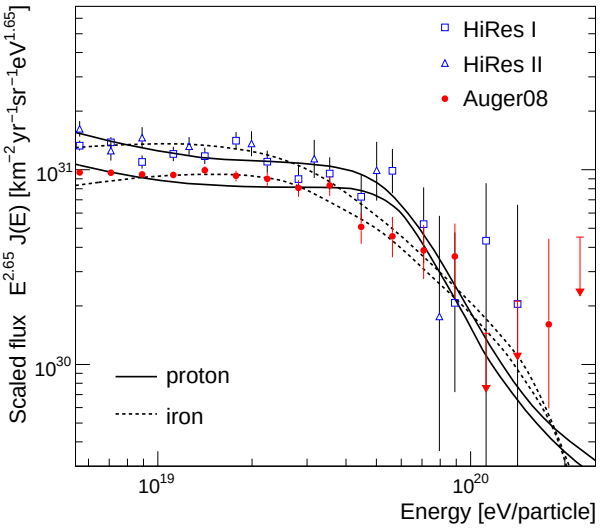


Figure 6.14: Measured flux at ultra-high energies compared to predictions for propagated proton and iron primaries ([131] lines adapted from [135] and [136]).

[135] and iron [136] composition at the source. A possible way to resolve this degeneracy would be the measurement of mass composition with high significance at this energy range.

# Conclusions

The aim of this work is the study of the energy spectrum of the ultra-high energy cosmic rays with the data collected by the Surface Detector (SD) of the Auger Observatory.

A method to convert the SD energy estimator ($S_{38}$) into shower energy using the Fluorescence Detector (FD) data has been developed.

The Auger energy calibration is based on the FD calorimetric measurement of the shower energy. This procedure allows to avoid the large uncertainties in the hadronic models of the simulation programs which have been used in the past to interpret the shower size at ground,

The sub-sample of Auger hybrid events, i.e. simultaneously detected by SD and FD, has been used to study the correlation between the SD observable $S_{38}$ and the FD energy ($E_{FD}$).

A power-law ($E = a \cdot {S_{38}}^b$) has been fitted to the hybrid data assigning to each event the statistical uncertainty in $E_{FD}$ and $S_{38^\circ}$. The values of the fitted parameters are:

$$a = [1.49 \pm 0.06(stat) \pm 0.12(syst)] \times 10^{17} \text{ eV},$$

$$b = 1.08 \pm 0.01(stat) \pm 0.04(syst),$$

with a reduced $\chi^2$ of 1.1. The fitted calibration curve is then used to estimate the energy for all events observed only by the SD.

The statistical uncertainty of the calibration curve propagated on the energy scale is 7% at $10^{19}$eV and 15% at $10^{20}$eV. A detailed study of the systematic uncertainty on the absolute energy scale from the FD measurements has been also performed.

In addition there is a scale error of 22% which is dominated by the uncertainties in the fluorescence yield, the FD absolute calibration and the longitudinal profile reconstruction.

I have developed a new method to reconstruct the longitudinal profile of the shower.

The key point of this new method is the possibility to calculate the expected photomultiplier signal from a model of the light distribution at

the telescope focal surface. This model is the result of a convolution of the shower image at diaphragm produced by the lateral distribution of the shower particles, with the detector response (spherical aberration, camera inhomogeneities and finite pixel dimension). Using this new method an energy estimator about 10% higher with respect to the official FD event reconstruction has been obtained and this difference has been quoted as systematic uncertainty on the FD energy scale used in the spectrum measurement.

The work done for this thesis as been used to derive the the SD energy spectrum measured by the Auger Observatory in [7]. The spectrum obtained, shows a suppression above $4 \times 10^{19}$eV as predicted by the GZK effect. The steepening has been quantified by making a power law ($J \propto E^{-\gamma}$) fit to the data below $4 \times 10^{19}$ eV: extrapolating the fitted power law we would expect $167 \pm 3$ events above $4 \times 10^{19}$ eV and $35 \pm 1$ above $10^{20}$ eV while 69 and 1 events have been observed, respectively.

The measured spectral index $\gamma$ of the energy spectrum below $4 \times 10^{19}$ eV is $2.69 \pm 0.02(stat) \pm 0.06(syst)$ and above this energy threshold is $4.2 \pm 0.4(stat) \pm 0.06(syst)$.

The Auger energy spectrum agrees within the systematic uncertainties with the spectrum measured by the Hires experiment. If the calibration curve obtained with the new longitudinal profile method developed in this work is used, the agreement between the two experiments becomes much better.

The energy at which the flux is suppressed matches the energy threshold of the correlation found by the Auger collaboration between the cosmic rays directions and the nearby AGNs (distance less then 100 Mpc). [137], supporting the hypothesis that at the highest energies, cosmic rays are originated from extra-galactic sources close enough that the flux is not significantly reduced by the GZK effect.

# Bibliography


[1] V. F. Hess, "Über Beobachtungen der durchdringenden Strahlung bei sieben Freiballonfahrten," *Phys. Zeitschr.* **13** (1912) 1084; V. F. Hess, "Über den Ursprung der durchdringenden Strahlung," *Phys. Zeitschr.* **14** (1913) 610.

[2] P. Auger, P. Ehrenfest, R. Maze, J. Daudin, Robley and A. Freon, "Extensive cosmic-ray showers," *Rev. Mod. Phys.* **11** (1939) 288–291; P. Auger, R. Maze, P. Ehrenfest and A. Freon *J. de Phys. et Rad.* **10** (1939); P. Auger, R. Maze and T. Grivet-Mayer, "Extensive cosmic showers in the atmosphere containing ultra–penetrating particles," *Compt. Rend. Acad. Sci. (Ser. II)* **206** (1938) 1721–1722; P. Auger and R. Maze, "Extensive cosmic showers in the atmosphere," *Compt. Rend. Acad. Sci. (Ser. II)* **207** (1938) 228–229.

[3] C. D. Anderson, "The positive electron," *Phys. Rev.* **43** (1933) 491–494; C. D. Anderson, "The apparent existence of easily deflectable positives," *Science* **76** (1932) 238.

[4] S. H. Neddermeyer and C. D. Anderson, "Note on the nature of cosmic ray particles," *Phys. Rev.* **51** (1937) 884–886; J. C. Street and E. C. Stevenson, "New evidence for the existence of a particle of mass intermediate between the proton and electron," *Phys. Rev.* **52** (1937) 1003–1004.

[5] **High Resolution Fly's Eye** Collaboration, R. U. Abbasi *et al.*, "First Observation of the Greisen-Zatsepin-Kuzmin Suppression," *Physical Review Letters* **100** (2008), no. 10, 101101–+.

[6] M. Takeda *et al.*, "Energy determination in the Akeno Giant Air Shower Array experiment," *Astropart. Phys.* **19** (2003) 447–462, astro-ph/0209422.

[7] **Pierre Auger** Collaboration, J. A. et al., "Evidence for suppression of the flux of cosmic rays above $10^{19}$ eV from the Pierre Auger Observatory," *accepted to Physical Review Letters* (2008) arXiv:0806.4302..

[8] **Pierre Auger** Collaboration, J. A. et al., "Correlation of the Highest-Energy Cosmic Rays with Nearby Extragalactic Objects," *Science* **318** (2007), no. 5852, 938–943, DOI: 10.1126/science.1151124.

[9] **Pierre Auger** Collaboration, J. A. et al., "Correlation of the highest-energy cosmic rays with the positions of nearby active galactic nuclei," *Astropart. Phys.* **29** (2007) 188–204, DOI:10.1016/j.astropartphys.2008.01.002. arXiv:0712.2843/astro-ph.

[10] E. Fermi, "On the Origin of the Cosmic Radiation," *Phys. Rev.* **75** (1949) 1169–1174.

[11] M. S. Longair, *High Energy Astrophysics*. Cambridge University Press, Cambridge, 2nd ed., 1993.

[12] A. M. Hillas, "The origin of ultrahigh-energy cosmic rays," *Ann. Rev. Astron. Astrophys.* **22** (1984) 425–444.

[13] M. Nagano and A. A. Watson, "Observations and implications of the ultrahigh-energy cosmic rays," *Rev. Mod. Phys.* **72** (2000) 689–732.

[14] F. A. Aharonian and J. W. Cronin, "Influence of the universal microwave background radiation on the extragalactic cosmic ray spectrum," *Phys. Rev.* **D50** (1994) 1892.

[15] S. Yoshida and M. Teshima, "Energy spectrum of ultrahigh-energy cosmic rays with extragalactic origin," *Prog. Theor. Phys.* **89** (1993) 833.

[16] G. T. Zatsepin and V. A. Kuzmin, "Upper limit of the spectrum of cosmic rays," *JETP Lett.* **4** (1966) 78–80; K. Greisen, "End to the cosmic ray spectrum?," *Phys. Rev. Lett.* **16** (1966) 748–750.

[17] T. Yamamoto *et al.*, "Propagation of ultra-high energy nucleus in the intergalactic photon field," in *Proc. 28th Int. Cosmic Ray Conf.*, Tsukuba, 2003, Kajita *et. al.* [138], vol. 2, pp. 723–726.

[18] A. Berezinsky, V. Gazizov and S. Grigorieva, "On astrophysical solution to ultra high energy cosmic rays," *Phys. Rev. D* **74** (2006) 043005, `hep-ph/0204357`.

[19] V. Ginzburg and S. Syrovatskii, *The origin of cosmic rays*. Pergamon Press, Oxford, russian edition (1963) ed., 1964.

[20] P. Biermann and P. Strittmatter, "Synchrotron emission from shockwaves in active galactic nuclei," *Astrophys. J.* **322** (1987) 643.

[21] J. P. Rachen and P. L. Biermann, "Extragalactic ultrahigh-energy cosmic rays. 1. Contribution from hot spots in FR-II radio galaxies," *Astron. Astrophys.* **272** (1993) 161–175, `astro-ph/9301010`.

[22] R. J. Protheroe and A. P. Szabo, "High energy cosmic rays from active galactic nuclei," *Phys. Rev. Lett.* **69** (Nov, 1992) 2885–2888.

[23] G. Benford and R. Protheroe, "Fossil AGN jets as ultra high energy particle accelerators," *Astrophys. J.* (2007) `arXiv:0706.4419 [astro-ph]`.

[24] P. Bhattacharjee and G. Sigl, "Monopole annihilation and highest energy cosmic rays," *Phys. Rev.* **D51** (1995) 4079–4091, `astro-ph/9412053`.

[25] S. Sarkar, "New physics from ultrahigh energy cosmic rays," *Acta Phys. Polon.* **B35** (2004) 351–364.

[26] M. Risse and P. Homola, "Search for ultra-high energy photons using air showers," *Mod. Phys. Lett.* **A22** (2007) 749–766, `astro-ph/0702632`.

[27] **Pierre Auger** Collaboration, J. Abraham *et al.*, "An upper limit to the photon fraction in cosmic rays above $10^{19}$ eV from the Pierre Auger observatory," *Astropart. Phys.* **27** (2007) 155–168, `astro-ph/0606619`.

[28] **Pierre Auger** Collaboration, J. Abraham *et al.*, "Upper limit on the cosmic-ray photon flux above $10^{19}$ eV using the surface detector of the Pierre Auger Observatory," *Astropart. Phys.* **29** (2008) 243–256, `0712.1147`.

[29] D. V. Semikoz and P. A. Collaboration, "Constraints on top-down models for the origin of UHECRs from the Pierre Auger Observatory data," 0706.2960.

[30] **The Pierre Auger** Collaboration, J. Abraham *et al.*, "Upper limit on the diffuse flux of UHE tau neutrinos from the Pierre Auger Observatory," *Phys. Rev. Lett.* **100** (2008) 211101, 0712.1909.

[31] J. Linsley, "Structure of large air showers at depth 834 G/sq cm. III - Applications," in *Proc. 15th Int. Cosmic Ray Conf.*, Plovdiv, 1977, Christov *et. al.* [139], vol. 12, pp. 89–96.

[32] **HiRes-MIA** Collaboration, T. Abu-Zayyad *et al.*, "Measurement of the cosmic ray energy spectrum and composition from $10^{17}$ eV to $10^{18.3}$ eV using a hybrid fluorescence technique," *Astrophys. J.* **557** (2001) 686–699, astro-ph/0010652.

[33] **The High Resolution Fly's Eye** Collaboration, R. U. Abbasi *et al.*, "A study of the composition of ultra high energy cosmic rays using the High Resolution Fly's Eye," *Astrophys. J.* **622** (2005) 910–926.

[34] **Fly's Eye** Collaboration, D. J. Bird *et al.*, "Evidence for correlated changes in the spectrum and composition of cosmic rays at extremely high energies," *Phys. Rev. Lett.* **71** (Nov, 1993) 3401–3404.

[35] V. P. Artamonov *et al.*, "Present state and outlook of the Yakutsk EAS array," *Bull. Russ. Acad. Sci. Phys.* **58** (1994) 2026–2031.

[36] M. U. for the Pierre Auger Collaboration, "Study of the Cosmic Ray Composition above 0.4 EeV using the Longitudinal Profiles of Showers observed at the Pierre Auger Observatory," *Proc. 30th Int. Cosmic Ray Conf.* (2007).

[37] J. W. Cronin, "The highest-energy cosmic rays," *Nucl. Phys. Proc. Suppl.* **138** (2005) 465–491, astro-ph/0402487.

[38] S. Yoshida and H. Dai, "The Extremely high-energy cosmic rays," *J. Phys.* **G24** (1998) 905, astro-ph/9802294.

[39] T. K. Gaisser, *Cosmic Rays and Particle Physics.* Cambridge University Press, Cambridge, 1990.

[40] **Auger** Collaboration, "The Pierre Auger Observatory Desing Report," 1997. FERMILAB-PUB-96-024.

[41] G. Molière, "Theorie der Streuung schneller geladener Teilchen. II. Mehrfachstreuung-und Vielfachstreuung," *Z. Naturforsch* **3a** (1948) 78.

[42] L. Cazon, R. A. Vazquez and E. Zas, "Depth development of extensive air showers from muon time distributions," *Astropart. Phys.* **23** (2005) 393–409, astro-ph/0412338.

[43] **Auger** Collaboration, J. Abraham *et al.*, "Properties and performance of the prototype instrument for the Pierre Auger Observatory," *Nucl. Instrum. Meth.* **A523** (2004) 50–95.

[44] S. Dagoret-Campagne, "The Central Trigger, user guide and reference manual," Auger Tech. Note GAP–2004–020.

[45] A. K. Tripathi, "A systematic study of large PMTs for the Pierre Auger Observatory," *Nucl. Instrum. Meth.* **A504** (2003) 1–3.

[46] A. Cordero *et al.*, "Proposal for the optical system of the fluorescence detectors of the Auger Project," Auger Tech. Note GAP–1996–039.

[47] G. Matthiae and P. Privitera, "The Schmidt telescope with corrector plate," Auger Tech. Note GAP–098–039.

[48] G. Borreani *et al.*, "The Fluorescence Detector prototype for the Auger project: Mechanical structure, optical system, and filter," *IEEE Trans. Nucl. Sci.* **48** (2001) 406–410.

[49] **Auger** Collaboration, G. Matthiae, "Optics and mechanics of the Auger Fluorescence Detector," in *Proc. 27th Int. Cosmic Ray Conf.*, Hamburg, 2001, Kampter *et. al.* [140], p. 733.

[50] R. Sato, J. Bellido, H. Reis and C. Escobar, "Corrector plate with an annulus shape," Auger Tech. Note GAP–1999–014; H. Reis, C. Escobar, R. Sato and J. Bellido, "A study of the corrector plates for the Auger fluorescence detector," Auger Tech. Note GAP–1999–013.

[51] M. Ambrosio *et al.*, "The camera of the Pierre Auger Observatory Fluorescence Detector," *Nucl. Instrum. Meth.* **A478** (2002) 125–129; C. Aramo *et al.*, "The camera of the AUGER Fluorescence Detector," Auger Tech. Note GAP–099–027.

[52] G. Matthiae and P. Privitera, "Study of the Philips hexagonal PMT XP3062 for the FD camera," Auger Tech. Note GAP–098–001.

[53] S. Argiro, D. Camin, M. Destro and C. Guerard, "Pasive and Active PMT Biasing Networks," Auger Tech. Note GAP–1998–063.

[54] M. Ambrosio, P. Facal, E. Kemp, G. Matthiae and P. Privitera, "The photomultipliers of the Auger Fluorescence Detector," *Nucl. Instrum. Meth.* **A504** (2003) 234–236; P. Facal, E. Kemp, G. Matthiae and P. Privitera, "The test system for the photomultipliers of the Fluorescence Detector," Auger Tech. Note GAP–2001–042.

[55] S. Argiro *et al.*, "The analog signal processing system for the Auger fluorescence detector prototype," *IEEE Trans. Nucl. Sci.* **48** (2001) 444–449.

[56] P. Privitera, E. Tusi and R. Cardarelli, "The baseline desing of the backplane distribution system of the FD camera," Auger Tech. Note GAP–099–029.

[57] D. Nicotra *et al.*, "The HV/LV power supply system for the Fluorescence Detector of the Pierre Auger Observatory," Auger Tech. Note GAP–2003–094.

[58] W. T. Thompson and R. Winston, *The optics of nonimaging concentrators: light and solar energy.* Academic Press, Nueva York, 1978.

[59] P. Facal and P. Privitera, "Measurement of the FD camera light collection efficiency and uniformity," Auger Tech. Note GAP–2000–010; P. Facal, "La cámara del detector de fluorescencia del experimento Auger." Memoria de Licenciatura. Universidad De Santiago de Compostela. Octubre 1999.

[60] **Auger** Collaboration, "The Pierre Auger Project Technical Desing Review," March, 2004.

[61] **Auger** Collaboration, M. Kleifges, "The Fluorescence Detector electronics of the Pierre Auger Observatory," *Nucl. Instrum. Meth.* **A518** (2004) 180–182.

[62] S. Argirò *et al.*, "The analog signal processor of the Auger Fluorescence Detector prototype," *Nucl. Instrum. Meth.* **A461** (2001) 440–448.

[63] **Auger** Collaboration, H. Gemmeke *et al.*, "The Auger Fluorescence Detector electronics," in *Proc. 27th Int. Cosmic Ray Conf.*, Hamburg, 2001, Kampter *et. al.* [140], p. 737.

[64] M. Kleifges, A. Menshikov, D. Chernyakhovsky and H. Gemmeke, "Statistical current monitor for the cosmic ray experiment Pierre Auger," *IEEE Trans. Nucl. Sci.* **50** (2003) 1204–1207; H. Gemmeke, M. Kleifges and A. Menshikov, "Statistical calibration and background measurements of the Auger Fluorescence Detector," in *Proc. 28th Int. Cosmic Ray Conf.*, Tsukuba, 2003, Kajita *et. al.* [138], vol. 2, pp. 891–894.

[65] J. Bellido, "Alignment and Synchronization of Bay4 at Los Leones and Bay3 at Coihueco using the CLF," Auger Tech. Note GAP–2004–059.

[66] N. Barenthien *et al.*, "The slow control system of the Auger Fluorescence Detectors," in *Proc. 28th Int. Cosmic Ray Conf.*, Tsukuba, 2003, Kajita *et. al.* [138], vol. 2, pp. 895–898.

[67] J. T. Brack, R. Meyhandan, G. J. Hofman and J. Matthews, "Absolute photometric calibration of large aperture optical systems," *Astropart. Phys.* **20** (2004) 653–659.

[68] **Auger** Collaboration, M. D. Roberts, "Calibration of the Pierre Auger Fluorescence Detector," in *Proc. 28th Int. Cosmic Ray Conf.*, Tsukuba, 2003, Kajita *et. al.* [138], vol. 1, pp. 453–456, `astro-ph/0308410`; J. Brack, R. Meyhandan and G. Hofman, "Prototype Auger absolute calibration system: Fluorescence Detector calibration at Los Leones," Auger Tech. Note GAP–2002–033.

[69] M. D. Roberts, P. Sommers and B. Fick, "Absolute calibration of the Auger Fluorescence Detectors using atmospheric laser beams," Auger Tech. Note GAP–2003–010.

[70] J. A. J. Matthews, "Optical Calibration of the Auger Fluorescence Telescopes," Auger Tech. Note GAP–2002–029; J. Rodriguez Martino and P. Privitera, "Relative calibration of the FD camera pixels," Auger Tech. Note GAP–2004–022.

[71] **Auger** Collaboration, M. A. Mostafa, "Atmospheric monitoring for the Pierre Auger Fluorescence Detector," in *Proc. 28th Int. Cosmic Ray Conf.*, Tsukuba, 2003, Kajita *et. al.* [138], vol. 1, pp. 465–468, `astro-ph/0308442`; **Pierre Auger** Collaboration, J. A. J. Matthews and R. Clay, "Atmospheric monitoring for the Auger Fluorescence Detector," in *Proc. 27th Int. Cosmic Ray Conf.*, Hamburg, 2001, Kampter *et. al.* [140], pp. 745–748.

[72] R. Mussa *et al.*, "The LIDAR systems for atmospheric monitoring in Auger," *Nucl. Instrum. Meth.* **A518** (2004) 183–185; A. Filipcic *et al.*, "Pierre Auger atmosphere-monitoring lidar system," in *Proc. 28th Int. Cosmic Ray Conf.*, Tsukuba, 2003, Kajita *et. al.* [138], vol. 1, pp. 461–464, `astro-ph/0305389`.

[73] R. Clay, "Note on the Probability of Cloud Free Observations at Los Leones," Auger Tech. Note GAP–2004–035.

[74] B. Keilhauer, B. Wilczynska and H. Wilczynski, "Molecular atmosphere profiles for Malargüe," Auger Tech. Note GAP–2005–021; B. Keilhauer, H. O. Klages and M. Risse, "Results of the first balloon measurements above the Pampa Amarilla," Auger Tech. Note GAP–2003–009.

[75] B. Fick *et al.*, "The first Central Laser Facility," Auger Tech. Note GAP–2004–003.

[76] S. Argiro *et al.*, "The offline software framework of the Pierre Auger observatory,".

[77] D. Newton, J. Knapp and A. A. Watson, "The Optimum Distance at which to Determine the Size of a Giant Air Shower,".

[78] E. S. Gruop, "The Official Event Selection as of March 2005," Auger Tech. Note GAP–2005–023.

[79] M. Horvat and D. Veberič, "On Shower-Front Start-Time Variance," Auger Tech. Note GAP–2007–057.

[80] C. B. et al., ed., *29th International Cosmic Ray Conference*, 7, no. 17. Pune, India, 2005.

[81] M. A. et al., ed., *30th International Cosmic Ray Conference*. Merida, Mexico, 2007. `arXiv:0709.2125 [astro-ph]`.

[82] K. Greisen *Progress in Cosmic Ray Physics* **3** (1956).

[83] K. Kamata and J. Nishimura *Prog. Theoret. Phys. Suppl.* **6** (1958) 93.

[84] M. Roth and D. Veberič, "SD Reconstruction," $\overline{\text{Off}}\underline{\text{line}}$ Reference Manual $\overline{\text{Off}}\underline{\text{line}}$ distribution.

[85] **Auger** Collaboration, M. Ave *et al. Nucl. Instrum. Meth.* **A578** (2007) 180.

[86] S. M. F. Arneodo and G. Navarra, "A procedure to derive the anode charges for saturated signals from the dynode and anode undershoots," Auger Tech. Note GAP–2005–025.

[87] M. R. I. C. Maris and T. Schmidt, "A Phenomenological Method to Recover the Signal from Saturated Stations," Auger Tech. Note GAP–2006–012.

[88] A. M. Hillas, "Derivation of the EAS spectrum," *Acta Physica Academiae Scientiarum Hungaricae Suppl. 3* **29** (1970) 355–360.

[89] A. M. Hillas, D. J. Marsden, J. D. Hollows and H. W. Hunter, "Measurement of Primary Energy of Air Showers in the Presence of Fluctuations," in *Proc. 12th Int. Cosmic Ray Conf.*, Hobart, 1971. A. Fenton and K. Fenton, eds., University of Tasmania Press, Hobart, Tasmania, 1971, vol. 3, p. 1001.

[90] M. Ave, R. A. Vazquez and E. Zas, "Modelling horizontal air showers induced by cosmic rays," *Astropart. Phys.* **14** (2000) 91, `astro-ph/0011490`.

[91] M. Unger *et al.*, "Reconstruction of Longitudinal Profiles of Ultra-High Energy Cosmic Ray Showers from Fluorescence andCherenkov Light Measurements," *Nucl. Instrum. Meth.* **A588** (2008) 433.

[92] R. M. Baltrusaitis *et al.*, "The Utah Fly's Eye Detector," *Nucl. Instrum. Meth.* **A240** (1985) 410.

[93] T. K. Gaisser and A. M. Hillas, "Reliability of the method of constant intensity cuts for reconstructing the average development of vertical showers," in *Proc. 15th Int. Cosmic Ray Conf.*, Plovdiv, 1977, Christov *et. al.* [139], vol. 8, pp. 353–357.

[94] S. Petrera and F. Salamida, "Status of the sky photon background flux measurement," Auger Tech. Note GAP-2006-014.

[95] E. Flyckt and C. Marmonier, eds., *PHOTOMULTIPLIER TUBES : Principles & applications*. Photonis, Brive, France, Sept., 2002.

[96] R. M. Baltrusaitis *et al.*, "Evidence of a high-energy cosmic ray spectrum cutoff," *Phys. Rev. Lett.* **54** (1985) 1875.

[97] P. Sokolsky, P. Sommers and B. R. Dawson, "Extremely high-energy cosmic rays," *Phys. Rept.* **217** (1992) 225.

[98] B. R. Dawson, "Flourescence Detector Techniques," Auger Tech. Note GAP–096–017.

[99] F. Kakimoto *et al.*, "A Measurement of the air fluorescence yield," *Nucl. Instrum. Meth.* **A372** (1996) 527–533.

[100] M. Nagano, K. Kobayakawa, N. Sakaki and K. Ando, "New measurement on photon yields from air and the application to the energy estimation of primary cosmic rays," *Astropart. Phys.* **22** (2004) 235–248, `astro-ph/0406474`.

[101] **AIRFLY** Collaboration, M. Ave *et al.*, "Measurement of the pressure dependence of air fluorescence emission induced by electrons," *Astropart. Phys.* **28** (2007) 41, `astro-ph/0703132`.

[102] A. M. Hillas, "Angular and energy distributions of charged particles in electron photon cascades in air," *J. Phys.* **G8** (1982) 1461–1473.

[103] **Pierre Auger** Collaboration, F. Nerling, J. Bluemer, R. Engel and M. Unger, "Impact of a new Cherenkov light parameterisation on the reconstruction of shower profiles from Auger hybrid data,".

[104] H. M. J. Barbosa, F. Catalani, J. A. Chinellato and C. Dobrigkeit, "Indirect determination of the missing energy content in extensive air showers," *Astropart. Phys.* **22** (2004) 159–166.

[105] T. Pierog, R. Engel and D. Heck, "Impact of uncertainties in hadron production on air-shower predictions,".

[106] D. Gora *et al.*, "Universal lateral distribution of energy deposit in air showers and its application to shower reconstruction," *Astropart.Phys.* **24** (2006) 484.

[107] D. Allard *et al.*, "A new method for the longitudinal profile reconstruction of the Auger Fluorescence Detector events," Auger Tech. Note GAP–2006–026.

[108] M. G. B. Daeson and G.Wieczorek, eds., *30th International Cosmic Ray Conference*. Merida, Mexico, 2007.

[109] M. Unger *et al.*, "Lateral shower light distributions in the Cherenkov-Fluorescence-Matrix Profile Reconstruction," Auger Tech. Note GAP–2008–052.

[110] D. Gora *et al.*, "Universal lateral distribution of energy deposit in air showers and its application to shower reconstruction," *J. Phys. G: Nucl. Part. Phys.* **31** (2005) 1291.

[111] J. P. et al., ed., *30th International Cosmic Ray Conference*, no. 335. Merida, Mexico, 2007.

[112] M. Giller and A. Smialkowski, eds., *30th International Cosmic Ray Conference*, no. 628. Merida, Mexico, 2007.

[113] B. Dawson *et al.*, "Test of Multiple Scattering Correction using Laser Shots," Auger Tech. Note GAP–2006–007.

[114] P. F. S. Luis, "High Energy Cosmic Rays at the Auger Observatory Fluorescence Detector," 2005.

[115] R. Ulrich *et al.*, "Manual of fluorescence detector simulation in Offline," Auger Tech. Note GAP-2008-014.

[116] C. A. et al. Physics Letters B667, "Particle Data Group," *Physics Letters* **B667** (2008) 331.

[117] I. C. Maris, "Measurement of the Ultra High Energy Cosmic Ray Flux using Data of the Pierre Auger Observatory," Auger Tech. Note GAP–2008–026.

[118] **Pierre Auger** Collaboration, B. R. Dawson, "Hybrid Performance of the Pierre Auger Observatory," `0706.1105`.

[119] N. G. Busca, "Private comunication," Auger Tech. Note Draft.

[120] L. Lyons, *Statistics for Particle and Nuclear Physicists*. Cambridge University Press, 1986.

[121] M. Ave and f. t. A. Collaboration, "Temperature and Humidity Dependence of Air Fluorescence Yield measured by AIRFLY," `0711.4583`.

[122] **Pierre Auger** Collaboration, D. Allard *et al.*, "The trigger system of the Pierre Auger surface detector: Operation, efficiency and stability,".

[123] N. G. Busca, "The Ultra High Energy Cosmic Ray Flux from the Southern Pierre Auger Observatory data," Ph.D. Thesis Chicago University, Illinois (2006).

[124] G. J. Feldman and R. D. Cousins, "A Unified Approach to the Classical Statistical Analysis of Small Signals," *Physical Review D* **57** (1998) 3873.

[125] J. D. Hague, B. R. Becker, M. S. Gold, J. A. J. Matthews and J. Urbar, "Statistical Methods for Investigating the Cosmic Ray Energy Spectrum," `0710.3600`.

[126] **HiRes** Collaboration, R. Abbasi *et al.*, "Observation of the GZK cutoff by the HiRes experiment," *Phys. Rev. Lett.* **100** (2008) 101101, `astro-ph/0703099`.

[127] A. M. Hillas, "Cosmic rays: Recent progress and some current questions,".

[128] T. Stanev, "The transition from galactic to extragalactic cosmic rays," *Nuclear Physics B Proceedings Supplements* **168** (2007) 252–257.

[129] V. Berezinsky, "Transition from galactic to extragalactic cosmic rays," *Proc. 30th ICRC, Merida* (2007).

[130] D. D. C. and G. Medina-Tanco, "Experimental constraints on the astrophysical interpretation of the cosmic ray Galactic-extragalactic transition region," *Astropart. Phys. arXiv:0807.4510* (2008).

[131] M. Unger, "Cosmic Rays above the Knee," `arXiv/0812.2763`.

[132] V. Berezinsky and S. I. Grigoreva *Bull. Russ. Acad. Sci. Phys.* **51N10** (1987) 111–113; A. Z. Berezinsky, V. Gazizov and S. I. Grigoreva *Phys. Rev. D* **74** (2006) 043005.

[133] D. Allard, E. Parizot and A. V. Olinto, "On the transition from Galactic to extragalactic cosmic- rays: spectral and composition features from two opposite scenarios," *Astropart. Phys.* **27** (2007) 61–75.

[134] D. Hooper, S. Sarkar and A. M. Taylor, "The intergalactic propagation of ultra-high energy cosmic ray nuclei," *Astropart. Phys.* **27** (2007) 199–212.

[135] R. Aloisio, P. Berezinsky, V. Blasi and S. Ostapchenko *Phys. Rev. D* **77** (2008) 025007.

[136] D. Allard, E. Parizot and A. V. Olinto *JCAP* **0810** (2008) 033.

[137] M.-P. Véron-Cetty and P. Véron, "A catalogue of quasars and active nuclei: 12th edition," *Astronomy and Astrophysics* **455** (aug, 2006) 773–777.

[138] T. Kajita *et al.*, eds., *28th International Cosmic Ray Conference*, Frontiers Science Series, no. 41. Universal Academy Press, Inc., Tokyo, Japan, 2003. `http://www-rccn.icrr.u-tokyo.ac.jp/icrc2003/`.

[139] C. Christov *et al.*, eds., *15th International Cosmic Ray Conference*. Institute for Nuclear Research, Bulgarian Academy of Sciences, Sofia, Bulgaria, 1978.

[140] K. H. Kampter *et al.*, eds., *27th International Cosmic Ray Conference*. Copernicus Gesellschaft e.V., Katlenburg-Lindau, Germany, 2001. `http://www.copernicus.org/C4/index.htm`.